

Non-linear viscoelasticity of linear and long-chain-branched polymer melts in shear and extensional flows

Von der Fakultät Verfahrenstechnik
der Universität Stuttgart zur Erlangung
des akademischen Grades eines Doktors der
Ingenieurwissenschaften (Dr.-Ing.)
genehmigte Abhandlung

von

Heike Bastian

aus Calw

Hauptberichter:	Prof. Dr.-Ing. M.H. Wagner
Mitberichter:	Prof. Dr.-Ing. P. Eyerer
Tag der mündlichen Prüfung:	22.06.2001

Institut für Kunststofftechnologie
2001

Acknowledgements

This Ph.D. work was performed during my employment as scientific coworker at the Institute of Plastics Technology (IKT), University of Stuttgart.

Sincere thanks are given to Prof. Dr.-Ing. M.H. Wagner for his continuous and invaluable advice during the course of this research. It was a great pleasure for me to work in an international environment on such an exciting subject under his supervision.

I would also like to thank Prof. Dr.-Ing. H.-G. Fritz, the director of IKT, who accepted and supported my scientific work.

Furthermore, I would like to thank Prof. Dr.-Ing. P. Eyerer for being co-advisor of my Ph.D. thesis.

Thanks also go to Dr. Patrice Rubio for many valuable, interesting discussions during his stay as post-doc in our group and to my students Tanja Häußermann and Anne Lacroix.

I would like to thank everybody who shared with me experimental data and material for performing my own experiments.

Thanks go to Dr. Thomas Schweizer at the Institute of Polymers (ETHZ) for his kind help in experimental work concerning the RME, and to everybody else who shared experiences with the RME, in particular to Dr. Erik Waßner at BASF AG.

Last but not least, I would like to thank all, present or past, colleagues of the institute for the pleasant time I spent at IKT.

Financial support from the European Commission and the German Science Foundation (DFG) is gratefully acknowledged.

Contents

Symbols	6
Abstract	9
Zusammenfassung	11
1 Introduction	14
2 Basics of Rheology	16
2.1 Fundamentals	16
2.1.1 The state-of-stress tensor and constitutive equations	16
2.1.2 The deformation gradient	17
2.1.3 Shear	19
2.1.4 Extension	20
2.2 Linear viscoelasticity	23
2.3 Network models	25
2.3.1 Entropy elasticity	25
2.3.2 Rubberlike-liquid theory	28
2.3.3 Damping function	29
2.4 Tube models	31
2.4.1 Doi-Edwards theory	35
2.4.2 Modifications of the Doi-Edwards theory	36
2.4.3 Molecular stress function (MSF) theory	40
3 Experimental methods	42
3.1 Extensional experiments	42
3.1.1 The elongational rheometer RME	46
3.1.2 Experimental results	48

3.1.3	Evaluation of the true strain-rate	52
3.1.4	Sample preparation	56
3.2	Shear experiments	58
4	Material characterisation and sample preparation	61
4.1	Linear polymer melts	61
4.1.1	HDPE I	61
4.1.2	PS	62
4.2	Long-chain-branched polymer melts	63
4.2.1	LDPE I	63
4.2.2	PP II	63
5	Experimental results and comparison to theory	65
5.1	Linear polymer melts	65
5.1.1	HDPE I	67
5.1.2	PS	72
5.2	Long-chain-branched polymer melts	75
5.2.1	LDPE I	77
5.2.2	PP II	83
5.3	Consequences for further developments of the MSF theory	85
6	Extended MSF theory including dissipative constraint release	87
6.1	The free energy of the MSF model	87
6.2	Kinematics of tube deformation and constraint release	91
6.3	Comparison to extensional and shear data of linear polymer melts	97
6.4	Comparison to extensional and shear data of long-chain-branched polymer melts	102
6.5	Comparison of steady-state values in shear and elongational flows with predictions of the extended MSF model	106

7	Conclusions	109
A	Comparison of uniaxial viscosity data to the MSF theory	111
A.1	Linear polymer melts	111
A.2	Long-chain-branched polymer melts	117
B	Summary of vector and tensor operations	123
	References	124

Symbols

a	[m]	Tube diameter
a_0	[m]	Tube diameter at equilibrium
a_1, a_2		Non-linear material parameters in the extended MSF model
a_T		Shift factor for time and frequency
A	[m ²]	Cross-section
b	[m]	Kuhn segment length
b_T		Shift factor in vertical direction
c	[1/m ³]	Segment concentration
$\underline{\underline{C}}_t(t')$		Relative Cauchy tensor
$\underline{\underline{C}}_t^{-1}(t')$		Relative Finger tensor
$\underline{\underline{D}}(r)$		Disentanglement function
$\underline{\underline{D}}$	[s ⁻¹]	Rate-of-deformation tensor
E_a	[J/mol]	Activation energy for flow
E_b	[J/mol]	Activation energy for vertical shift
$\underline{\underline{E}}$		Unit tensor
f		Molecular stress function
F_N	[N]	Normal force
$\underline{\underline{F}}_t$		Relative deformation gradient
$\underline{\underline{F}}_t^{-1}$		Inverse deformation gradient
g		Normalisation factor
$g[\underline{q}, \underline{\bar{q}}, \underline{\bar{p}}]$	[s ⁻¹]	Constraint release function
g_i	[Pa]	Modulus of i^{th} Maxwell element
$\dot{G}(t - t')$	[Pa]	Linear-viscoelastic shear relaxation modulus
G_N^0	[Pa]	Plateau modulus
$G(t)$	[Pa]	Non-linear shear relaxation modulus
$G'(\omega)$	[Pa]	Storage modulus
$G''(\omega)$	[Pa]	Loss modulus
$h(I_1, I_2)$		Damping function
H	[m]	Gap of the plate-and-plate geometry
I_1, I_2, I_3		Invariants of a tensor
k	[J/K]	Boltzmann constant
$K, \underline{\underline{K}}$	[N]	Force, force vector
l, L	[m]	Contour length of the tube
m		Mode of extensional flow
$\dot{m}(t - t')$	[Pas ⁻¹]	Linear-viscoelastic memory function
M	[Nm]	Torque
M_n	[g/mol]	Number-averaged molecular weight
M_W	[g/mol]	Weight-averaged molecular weight

n		Number of Kuhn segments
\underline{n}		Surface vector
N		Number of chains per unit volume
N_e		Number of monomers between entanglements
N_1, N_2	[Pa]	First and second normal stress difference in shear
p	[bar]	Pressure
\underline{p}		Unit vector tangential to a tube segment at any time t
$\underline{\bar{p}}$		Affine time derivative of \underline{p}
P_0		Degree of polymerisation
$P_r(r) dr$		Probability to find a chain between $ \underline{r} $ and $ \underline{r} + d\underline{r} $
$P_t(t)$		Survival probability of a tube segment
\underline{q}		Unit vector normal to the tube cross-section at any time t
$\underline{\bar{q}}$		Affine time derivative of \underline{q}
\underline{r}, r	[m]	End-to-end vector and its length
R, r	[m]	Radius
\mathcal{R}	[J/molK]	Ideal gas constant
$\underline{R}_t(t')$		Relative rotation tensor
s, S	[J/m ³]	Entropy
$S(r)$		Slip function
$\underline{S}_t(t')$		Non-linear strain measure
$\underline{\underline{T}}$	[Pa]	Extra stress tensor
t	[s]	Time
T_{eq}	[s]	Equilibration time
T_d	[s]	Disengagement time
T	[°C]	Temperature
T_0	[°C]	Reference temperature
\underline{u}		Unit vector
\underline{u}', u'		Deformed unit vector and its length
$\langle \ln(u') \rangle$		Average logarithmic stretch
U	[J/m ³]	Internal energy
$\underline{U}_t(t')$		Relative stretch tensor
v, \underline{v}	[m/s]	Velocity, velocity vector
w	[J]	Free energy
W	[J/m ³]	Helmholtz free energy per unit volume
$\underline{\underline{W}}$	[s ⁻¹]	Rate-of-rotation tensor

α		Slip factor in the MSF model
β		Cone angle. Parameter of branching topology
γ		Shear deformation
$\dot{\gamma}$	$[s^{-1}]$	Shear-rate
δ		Phase lag
ϵ		Hencky strain
$\dot{\epsilon}$	$[s^{-1}]$	Extensional strain-rate
$\underline{\underline{\epsilon}}_t(t')$		Linear strain measure
η	[Pas]	Viscosity
η_0	[Pas]	Zero shear viscosity
η^*	[Pas]	Complex viscosity
η_B	[Pas]	Viscosity at brittle polymer breackage
ϑ	[°]	Angular displacement in the cone-and plate geometry
$\underline{\underline{\kappa}}$	$[s^{-1}]$	Velocity gradient
λ		Stretch
μ	[Pas]	Extensional viscosity rescaled to zero-shear viscosity
ρ	$[g/cm^3]$	Density
ω	$[s^{-1}]$	Frequency, angular velocity
σ_{ij}	[Pa]	Stress tensor component
σ_1, σ_2	[Pa]	First and second normal stress difference in extension
σ_B	[Pa]	Stress at break of a filament
$\underline{\underline{\sigma}}$	[Pa]	Stress tensor
$\tau_i = \eta_i/g_i$	[s]	Relaxation time
φ		Average functionality of a network
$\psi_0(r)$		Distribution function
Ψ_1, Ψ_2	$[Pas^2]$	First and second normal stress coefficient in shear

Abstract

Non-linear viscoelasticity of linear and long-chain-branched polymer melts in shear and extensional flows

In many polymer processes, the polymer melt is not only subjected to shear flow, but also to considerable extensional or stretching flows. For simulation of polymer processing by numerical methods, a constitutive equation is necessary which describes the relation between stress and deformation for any deformation history.

In chapter 2, the basics of continuum mechanics at large deformations and the theory of linear viscoelasticity are summarised. Then network models are considered, namely the theory of entropy elasticity and the rubber-like liquid model including the damping function approach. For tube models, non-linear strain measures are derived from a molecular slip-link model in which entanglements are modelled as small rings through which the macromolecular chain can reptate freely. The slip-link model includes the strain measure of the Doi-Edwards (DE) theory. Here, the chain is assumed to be confined inside a tube-like region, as polymer chains cannot pass freely through each other. The major restriction of the Doi-Edwards theory concerning non-linear viscoelasticity is the assumption of a constant tube diameter a_0 independent of the deformation, i.e. according to this model, stress is only the result of chain orientation. As polymer melts show higher stresses than can be accounted for by chain orientation, further developments of constitutive equations considering chain stretch processes are presented, which can be divided into rate-dependent and strain-dependent equations. The molecular stress function (MSF) theory, starting point of all further developments within this work, is a strain-dependent model which describes chain stretch by a reduction of the tube diameter. In the MSF model, chain stretch is taken into account by a molecular stress function f which relates the real tension in the chain to the equilibrium tension, and which can be expressed by the inverse of the relative tube diameter a/a_0 .

In chapter 3, the experimental methods used to investigate the rheology of polymer melts in shear and extensional flows are presented. A literature review is given on uniaxial and biaxial extensional rheometry. Experimental details and problems of a commercial elongational rheometer (Rheometrics RME) are presented, which is used to perform elongational measurements on various polymer melts. By means of rotational rheometry, the linear-viscoelastic characterisation of the investigated polymer melts and the non-linear shear characterisation by stress-relaxation and start-up flow experiments are performed.

In chapter 4, the characteristic properties and test conditions of the investigated linear (HDPE, PS) and long-chain-branched (LDPE, PP) polymer melts are summarised.

In chapter 5, experimental data of shear and extensional flows are compared to the DE and to the MSF theory. While the shear-thinning behaviour of polymer melts is at least qualitatively predicted, the Doi-Edwards (DE) model cannot predict any strain-hardening behaviour in extensional flows. However, this is possible with the MSF model: Derived from a strain energy function, the molecular stress function f depends on the average logarithmic stretch $\langle \ln(u') \rangle_0$. For linear melts, a linear dependence of f on $\exp(\langle \ln(u') \rangle_0)$ is found, which is called the linear molecular stress function (LMSF) model. Long-chain-branched melts show a stronger viscosity upturn which can be taken into account by a quadratic dependence on $\exp(\langle \ln(u') \rangle_0)$, and which is called the quadratic molecular stress function (QMSF) model. Extensional viscosities of both linear and long-chain-branched melts show a saturation effect and approach steady-state values at large deformations. This is modelled by the assumption that the reduction of the tube diameter is limited, i.e. a maximum stretch of the macromolecular chains exists. Therefore, a maximum value of the molecular stress function, f_{max} , is introduced. A large value of f_{max} is responsible for enhanced strain-hardening, a small value of f_{max} for a small amount of strain-hardening, and $f_{max} = 1$ corresponds to the DE limit. When f_{max} is fitted to the uniaxial viscosity, a consistent description of all extensional deformation modes is possible. However, with the same f_{max} , it is not possible to describe shear flow quantitatively. A smaller value of f_{max} is necessary.

To understand the difference between rotational and irrotational flows, the kinematics of tube deformation is further investigated in chapter 6. Constraint release (CR) is introduced as a dissipative process which modifies the energy balance of the MSF model and leads to a strain-dependent evolution equation for the molecular stress function. The new constraint release mechanism is based on the difference between affine convection of unit vectors describing tube segment orientation and tube cross-section orientation. Tube kinematics is fundamentally different for rotational and irrotational flows, and therefore distinguishes explicitly between simple shear and pure shear (planar extension). This new MSF model, consisting of a history integral for the stress tensor and a differential evolution equation for the molecular stress function, allows a consistent, quantitative prediction of shear flow and uniaxial, equibiaxial and planar flow with only two non-linear parameters a_1 and a_2 , both of which govern dissipation in simple shear flow, while dissipation in extensional flows (being irrotational) depends on a_1 only, and a_1 determines the maximum molecular stress f_{max} .

Hence, a constitutive equation is now available which can be expected to model accurately the non-linear viscoelasticity of linear and long-chain-branched polymer melts for any deformation history.

Zusammenfassung

Nichtlineare Viskoelastizität von linearen und langkettenverzweigten Polymer-schmelzen in Scherung und Dehnung

Bei vielen Prozessen der Kunststoffverarbeitung unterliegt die Polymerschmelze nicht nur Scher-, sondern auch Dehndeformationen. Damit die Auslegung dieser Prozesse mit Hilfe von numerischen Methoden durchgeführt werden kann, ist eine allgemeingültige rheologische Zustandsgleichung erforderlich, die den Zusammenhang von Spannung und Deformation erklärt. Diese muß sowohl für uniaxiale, äquibiaxiale und planare Dehnungen als auch für Scherung gültig sein.

Zunächst werden in Kapitel 2 die kontinuumsmechanischen Grundlagen großer Deformationen vorgestellt. Anschließend wird die Theorie der linearen Viskoelastizität betrachtet, die bei kleinen Deformationen auch den Grenzfall nichtlinearer Modelle darstellt. Anhand von Netzwerkmodellen werden die Theorie der Entropielastizität polymerer Materialien, die daraus entwickelte Theorie der gummiartigen Flüssigkeit von Lodge sowie deren Modifizierung durch Einführung einer deformationsabhängigen Dämpfungsfunktion erläutert. Bei "Slip-Link"-Modellen nimmt man an, daß die Wechselwirkung der Makromoleküle untereinander auf lokalisierte "Entanglements" beschränkt ist, die man sich als kleine Ringe vorstellt, durch die die Makromoleküle diffundieren oder "reptieren". Ein Spezialfall der "Slip-Link"-Modelle ist die Doi-Edwards (DE)-Theorie, bei der die Dynamik eines Makromoleküls auf eine Röhre mit dem Durchmesser a_0 beschränkt ist. Die Röhre stellt die umgebenden Makromoleküle dar, da sich Makromoleküle gegenseitig nicht durchdringen können. Mit der Annahme von Doi und Edwards, daß sich der Röhrendurchmesser bei Deformation nicht ändert, kann jedoch nur die Orientierung der Molekülketten beschrieben werden. Da Polymerschmelzen jedoch insbesondere bei Dehndeformationen höhere Spannungen zeigen als durch Orientierungseffekte allein zu erwarten wären, muß bei Weiterentwicklungen der Theorie zusätzlich zur Orientierung eine Streckung der Makromoleküle berücksichtigt werden. Prinzipiell lassen sich Modelle mit einer Abhängigkeit der Kettenstreckung von der Deformationsgeschwindigkeit und von der Deformation unterscheiden. Die Theorie der Molekularspannungsfunktion (MSF), die Ausgangspunkt für alle weiteren Entwicklungen in dieser Arbeit ist, gehört zu den deformationsabhängigen Modellen, die davon ausgehen, daß die Kettenstreckung durch eine Abnahme des Röhrendurchmessers bewirkt wird. Dies wird beim MSF-Modell mit der molekularen Spannungsfunktion f beschrieben, die das Verhältnis der tatsächlich im Molekül wirkenden Kraft zur Gleichgewichtskraft berücksichtigt und sich als Inverse des relativen Röhrendurchmessers a/a_0 ausdrücken läßt.

In Kapitel 3 werden die rheometrischen Methoden zur Untersuchung von Polymerschmelzen in Dehnung und Scherung dargestellt. Nach einer kurzen Übersicht über Entwicklungen in der Dehnrheometrie werden die experimentellen Besonderheiten und Probleme des kommerziellen uniaxialen Dehnrheometers RME aufgezeigt, mit dem Messungen an zahlreichen Polymerschmelzen durchgeführt wurden. Anschließend wird kurz die Rotationsrheometrie vorgestellt, mit deren Hilfe die lineare Charakterisierung der Polymerschmelzen und die nichtlineare Untersuchung in Scherung mit Spannungsrelaxations- und Spannversuchen vorgenommen wurde.

In Kapitel 4 erfolgt die Zusammenstellung aller wichtigen Materialkennwerte der untersuchten linearen (HDPE, PS) und langkettenverzweigten (LDPE, PP) Polymerschmelzen.

In Kapitel 5 werden die experimentellen Daten in Dehnung und Scherung mit der Doi-Edwards (DE)-Theorie und der MSF-Theorie verglichen. Während die DE-Theorie das Scherverhalten von Polymerschmelzen zumindest qualitativ beschreibt, unterschätzt sie die bei Dehndeformationen auftretende Dehnverfestigung deutlich. Leitet man die Molekularspannungsfunktion f von einer Deformationsenergiefunktion ab, so läßt sich zeigen, daß f eine Funktion der mittleren logarithmischen Streckung $\langle \ln(u') \rangle_0$ ist. Für lineare Polymerschmelzen hängt f linear von $\exp(\langle \ln(u') \rangle_0)$ ab, was als lineare Molekularspannungsfunktion (LMSF) bezeichnet wird. Langkettenverzweigte Polymerschmelzen zeigen mit zunehmender Deformation einen stärkeren Anstieg der Molekularspannung, was durch die quadratische Molekularspannungsfunktion (QMSF) mit einer quadratischen Abhängigkeit der Molekularspannungsfunktion f von $\exp(\langle \ln(u') \rangle_0)$ berücksichtigt werden kann. Die Dehnverfestigung von linearen und langkettenverzweigten Polymerschmelzen ist nach oben hin begrenzt; dies läßt sich durch die Annahme eines maximalen Wertes f_{max} für die Molekularspannungsfunktion beschreiben. Der nichtlineare Materialparameter f_{max} berücksichtigt, daß die Abnahme des Röhrendurchmessers nach unten hin begrenzt ist, und ist direkt mit dem Dehnverfestigungsverhalten von Polymerschmelzen verknüpft: Ein großer f_{max} -Wert ist für eine hohe Dehnverfestigung, ein kleiner f_{max} -Wert für eine geringe Dehnverfestigung verantwortlich. Für $f_{max} = 1$ erhält man den Grenzfall der DE-Theorie. Wenn f_{max} an uniaxiale Dehndaten angepaßt wird, ist eine konsistente Beschreibung des rheologischen Verhaltens bei allen Dehndeformationen möglich. Die Analyse der Scherdaten liefert jedoch davon abweichende (kleinere) Molekularspannungen.

Um diese Diskrepanz in der Beschreibung von Scher- und Dehnverhalten zu beseitigen, wird in Kapitel 6 die Energiebilanz des MSF-Modells durch Einführung von "Constraint-Release" als dissipativer Prozess so modifiziert, daß eine Differentialgleichung 1. Ordnung für die Molekularspannungsfunktion entsteht. Unter "Constraint-Release" versteht man, daß sich topologische Hindernisse, modelliert durch das Röhrenmodell, teilweise auflösen durch die Relativbewegung zwischen den einzelnen Ketten bei Dehn- oder Scherströmungen. Dabei wird "Constraint-Release" als Folge unterschiedlicher Konvektionsmechanismen für Röhrenorientierung und

Röhrenquerschnitt betrachtet. Die dissipativen "Constraint-Release"-Prozesse für rotationsbehaftete und rotationsfreie Strömungen zeigen grundlegende Unterschiede, weshalb das erweiterte MSF-Modell explizit zwischen einfacher Scherung und planarer ("reiner Scherung") Dehnung unterscheiden kann. Das neue Modell, bestehend aus einer Integralgleichung für den Spannungstensor und einer differentiellen Entwicklungsgleichung für die Molekularspannungsfunktion, erlaubt eine einheitliche, quantitative Beschreibung des rheologischen Verhaltens von Polymerschmelzen bei Scherdeformation und uniaxialen, äquibiaxialen und planaren Dehndeformationen mit nur zwei nichtlinearen Materialparametern a_1 und a_2 . Während die Dissipation in Scherung von beiden Materialparametern abhängt, ist die Dissipation in Dehnung nur von dem Materialparameter a_1 abhängig, der die maximale Spannung f_{max} bestimmt.

Damit steht jetzt eine rheologische Zustandsgleichung zur Verfügung, von der zu erwarten ist, daß sie die nichtlineare Viskoelastizität von linearen und langkettenverzweigten Polymerschmelzen bei beliebiger Deformationsgeschichte modelliert.

1 Introduction

In many polymer processes, the polymer melt is not only subjected to shear flow, but also to considerable extensional or stretching flows, especially in blow moulding, vacuum forming, and fibre-spinning, but also in calendering and extrusion. Hence, a constitutive equation which allows a consistent description of polymer melt rheology under shear and biaxial deformations is necessary for simulation of polymer processing by numerical methods. A constitutive equation relates stress and deformation, and should allow predictions of the state-of-stress for any arbitrary deformation history, i.e. not only either for simple shear flow or either for extensional flows. The predictions of shear flow and extensional flows provide material parameters which can be used for simulation and optimisation of polymer processes.

The rheology of polymer melts is intensively influenced by flow kinematics. While the shear viscosity at start-up flow never rises above the zero-shear viscosity η_0 , determined by measurements at small shear-rates, and exhibits shear-thinning, the transient viscosity in uni- and biaxial flow exhibits strain-hardening, except for the second planar viscosity. The quantitative amount of strain-hardening depends on the melt architecture, i.e. whether the polymer melt consists of a linear or a branched structure. This different rheological behaviour makes it extremely difficult to develop a constitutive equation which quantitatively describes both shear and extensional rheology in start-up flows. Furthermore, the experimentally observed time/deformation separability must be verified by the constitutive equation for stress relaxation after a shear step-strain experiment.

By use of the phenomenological K-BKZ single-integral model (1963) [4], first progress was made in qualitatively predicting some aspects of polymer rheology with flexible kernel functions which allow to fit uniaxial and shear data uniformly by empirical material parameters, but which fail for planar flow. Doi and Edwards (1978) [18], [19] introduced the tube model with a universal non-linear strain measure for polymer melts where the stress is governed only by orientation of the polymer chains, and time/deformation separability is observed. While the shear-thinning behaviour of polymer melts is at least qualitatively predicted, the Doi-Edwards (DE) model cannot predict any strain-hardening behaviour in extensional flows [81]. For this reason, the tube model was modified in such a way that stretch processes of the tube segments due to flow and according to the topology of the melt are taken into account [39], [85], [86], [41]. In the molecular stress function (MSF) theory of Wagner et al. (1998) [79], all extensional modes can be described consistently with only one non-linear material parameter, but this model cannot predict shear flow quantitatively.

However, constitutive modelling can only be approached successfully if reliable experimental data are available. While shear flow rheometry has been state of the art for many decades now, the investigation of strain-hardening in extensional flows is still in development, particularly concerning general biaxial extension of polymer melts. Ex-

tensional flow rheometry is difficult to perform as the polymer melt deforms with a free surface in contrast to shear flow rheology where the sample is confined between two adjacent solid surfaces. But after the advent of new experimental techniques, above all the progress in the rotary clamp technique [14], [49], [23], more and more extensional data are available.

In this work, experimental data of a linear (HDPE) and a long-chain-branched (LDPE) polyethylene melt measured in shear flow by Kraft (1996) [27], and in uniaxial, equibiaxial, and planar extensional flow by Hachmann (1996) [23] are analysed with the intention to check and improve tube models. Measurements in shear flow with rotational rheometry, and in uniaxial elongational flow with a commercial elongational rheometer RME [49] were repeated to prove the reliability of the experimental data. Additionally, shear relaxation experiments were performed to extend the number of non-linear rheological experiments for the purpose of verification of improved constitutive equations. Further uniaxial elongational tests were performed on many linear, short-chain-branched and long-chain-branched polymer melts. Simultaneously, experimental problems with the commercial elongational rheometer RME are revealed, and experimental results of our RME are compared to results of other RMEs and of the Mnstedt tensile rheometer (MTR).

The aim of this work is then the development of a general rheological constitutive equation for polymer melts which allows to describe extensional flows and shear flow consistently by taking into account the DE tube model and extending the MSF theory.

2 Basics of Rheology

2.1 Fundamentals

2.1.1 The state-of-stress tensor and constitutive equations

Constitutive equations describe the relationship between the state-of-stress and the deformation history. Generally, stress is defined as force per unit area. If \underline{K} is the force vector per unit area acting on a surface characterised by the normal vector \underline{n} [77], then

$$\underline{K} = \underline{\underline{\sigma}} \cdot \underline{n} \quad (2.1)$$

with the stress tensor $\underline{\underline{\sigma}}$. According to the principle of conservation of angular momentum, the stress tensor is a symmetric tensor. Hence, $\underline{\underline{\sigma}}$ is equal to its transpose $\underline{\underline{\sigma}}^T$ denoted by the superscript T . The nine components of the stress tensor $\underline{\underline{\sigma}}$

$$\underline{\underline{\sigma}} = \begin{pmatrix} \sigma_{11} & \sigma_{12} & \sigma_{13} \\ \sigma_{21} & \sigma_{22} & \sigma_{23} \\ \sigma_{31} & \sigma_{32} & \sigma_{33} \end{pmatrix} \quad (2.2)$$

specify completely the state-of-stress at a material point. The first subscript of σ indicates the surface on which the component acts, and the second subscript the direction corresponding to the coordinate axis (fig. 2.1). A symmetric tensor can be

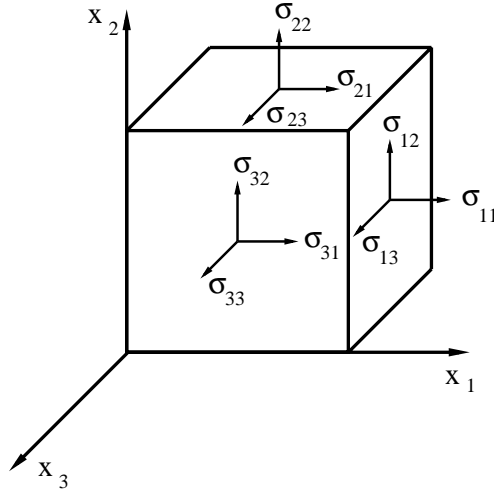


Figure 2.1: Definition of the stress tensor [20].

transformed to principle axes, in which the tensor only has diagonal components. The transformation of the stress tensor $\underline{\underline{\sigma}}$ to its diagonal form leads to the three invariants of $\underline{\underline{\sigma}}$ which are independent of the coordinate system chosen:

$$I_1 = \text{tr} \underline{\underline{\sigma}} = \sigma_{11} + \sigma_{22} + \sigma_{33} \quad (2.3)$$

$$I_2 = \frac{1}{2} [\text{tr}^2(\underline{\underline{\sigma}}) - \text{tr} \underline{\underline{\sigma}}^2] \quad (2.4)$$

$$I_3 = \det \underline{\underline{\sigma}} \quad (2.5)$$

\det is the determinant, and tr the trace of a tensor.

The stress tensor $\underline{\underline{\sigma}}$ can be divided into an isotropic and a deviatoric part [6],

$$\underline{\underline{\sigma}} = -p \underline{\underline{E}} + \underline{\underline{T}} \quad (2.6)$$

where p is the isotropic pressure, $\underline{\underline{E}}$ the unit tensor and $\underline{\underline{T}}$ the extra stress tensor with $\text{tr} \underline{\underline{T}} = 0$. For incompressible materials, a constant isotropic pressure can be added without any influence on the flow field. Hence, only normal stress differences are of relevance in the rheology of incompressible materials. For isotropic, homogeneous and incompressible "simple" liquids, the relationship between the stress tensor and the deformation history can be described by [77]

$$\underline{\underline{\sigma}}(t) = -p \underline{\underline{E}} + \mathfrak{S}_{t'=-\infty}^{t'=t}(\underline{\underline{C}}_t(t')) \quad (2.7)$$

$\mathfrak{S}_{t'=-\infty}^{t'=t}$ is a functional depending on the relative Cauchy tensor $\underline{\underline{C}}_t(t')$. Since $\underline{\underline{C}}_t(t')$ is a rotationfree tensor (chapt. 2.1.2), the principle of frame invariance [32] is obeyed which requires independence of any time-dependent rotation. Equations of the type of Eq. (2.7) are called "constitutive equations".

2.1.2 The deformation gradient

Deformations appear if distances between material points change with motion [1], [6], [32]. To describe arbitrary deformations, it is thus necessary to compare the distance of two fluid particles at some past time t' , given by the vector $d \underline{\underline{x}}'$, and the distance of the same two particles at the instant t of observation, denoted by $d \underline{\underline{x}}$. The relation between these two vectors can be expressed by

$$d \underline{\underline{x}}' = \underline{\underline{F}}_t(t') \cdot d \underline{\underline{x}} \quad (2.8)$$

with the relative deformation gradient tensor $\underline{\underline{F}}_t$ between time t and t' defined as

$$\underline{\underline{F}}_t(t') = \frac{\partial \underline{\underline{x}}'}{\partial \underline{\underline{x}}} \quad (2.9)$$

and $F_{ij} = \partial x'_i / \partial x_j$, respectively.

The inverse deformation gradient $\underline{\underline{F}}_t^{-1}$, $F_{ij}^{-1} = \partial x_i / \partial x'_j$,

$$d \underline{\underline{x}} = \underline{\underline{F}}_t^{-1}(t') \cdot d \underline{\underline{x}}' \quad (2.10)$$

relates the past distant $d \underline{x}'$ to the distance $d \underline{x}$ at the observation time t .

The relative deformation gradient $\underline{\underline{F}}_t(t')$ can be expressed as the product of the relative stretch tensor $\underline{\underline{U}}_t(t')$ and the relative rotation tensor $\underline{\underline{R}}_t(t')$,

$$\underline{\underline{F}}_t(t') = \underline{\underline{R}}_t(t') \cdot \underline{\underline{U}}_t(t') \quad (2.11)$$

Hence, $\underline{\underline{F}}_t(t')$ depends on stretch (i.e. change of the distance between material points) as well as (rigid) rotation.

The square distance $d x'^2$ of two material points before deformation can be determined by

$$d x'^2 = \underline{\underline{F}}_t(t') \cdot d \underline{x} \cdot \underline{\underline{F}}_t(t') \cdot d \underline{x} = d \underline{x} \cdot \underline{\underline{F}}_t^T(t') \cdot \underline{\underline{F}}_t(t') \cdot d \underline{x} = d \underline{x} \cdot \underline{\underline{C}}_t(t') \cdot d \underline{x} \quad (2.12)$$

which defines the relative Cauchy tensor $\underline{\underline{C}}_t(t')$ as

$$\underline{\underline{C}}_t(t') = \underline{\underline{F}}_t^T(t') \cdot \underline{\underline{F}}_t(t') = \underline{\underline{U}}_t^2(t') \quad (2.13)$$

The inverse of the relative Cauchy tensor, the Finger tensor $\underline{\underline{C}}_t^{-1}(t')$, is then given by

$$\underline{\underline{C}}_t^{-1}(t') = (\underline{\underline{F}}_t^T(t') \cdot \underline{\underline{F}}_t(t'))^{-1} = \underline{\underline{F}}_t^{-1}(t') \cdot (\underline{\underline{F}}_t^{-1}(t'))^T = \underline{\underline{U}}_t^{-2}(t') \quad (2.14)$$

$\underline{\underline{C}}_t(t')$ and $\underline{\underline{C}}_t^{-1}(t')$ are rotationfree, symmetric deformation tensors. The three invariants of the Finger tensor $\underline{\underline{C}}_t^{-1}(t')$ are

$$I_1 = \text{tr}(\underline{\underline{C}}_t^{-1}(t')) \quad (2.15)$$

$$I_2 = \frac{1}{2}[(\text{tr}(\underline{\underline{C}}_t^{-1}(t')))^2 - \text{tr}(\underline{\underline{C}}_t^{-2}(t'))] \quad (2.16)$$

$$I_3 = \det(\underline{\underline{C}}_t^{-1}(t')) \quad (2.17)$$

The incompressibility condition corresponds to $I_3 \equiv 1$. For infinitesimal deformations, a linear strain measure $\underline{\underline{\varepsilon}}_t(t')$ can be derived from the gradient of the displacement vector $\underline{u}(t') = \underline{x}(t) - \underline{x}(t')$,

$$\underline{\underline{\varepsilon}}_t(t') = \frac{1}{2} [\underline{\nabla} \underline{u} + (\underline{\nabla} \underline{u})^T] \quad (2.18)$$

where the symbolic vector $\underline{\nabla} = d/d\underline{x}$ denotes the gradient.

Taking the time derivative of $\underline{\underline{F}}_t^{-1}(t')$ and considering $t' \rightarrow t$ [77], the velocity gradient $\underline{\underline{\kappa}}$ is given by

$$\frac{\partial}{\partial t} \underline{\underline{F}}_t^{-1}(t')|_{t' \rightarrow t} = \underline{\nabla} \underline{v} = \underline{\underline{\kappa}} \quad (2.19)$$

with the velocity vector \underline{v} of a fluid particle at time t .

The rate-of-deformation tensor $\underline{\underline{D}} = 1/2(\underline{\underline{\kappa}} + \underline{\underline{\kappa}}^T)$ is defined as the symmetric part of the velocity gradient, and the rate-of-rotation tensor $\underline{\underline{W}} = 1/2(\underline{\underline{\kappa}} - \underline{\underline{\kappa}}^T)$ as the antisymmetric part,

$$\underline{\underline{\kappa}} = \underline{\underline{D}} + \underline{\underline{W}} \quad (2.20)$$

2.1.3 Shear

A simple shear deformation can be achieved by shearing a sample between two parallel plates which have a fixed distance. The shear force is tangential to the moving surface, and the shear stress σ_{12} is defined by the force divided by the tangential area on which the force acts. Considering a unit cube (fig. 2.2), the inverse relative deformation

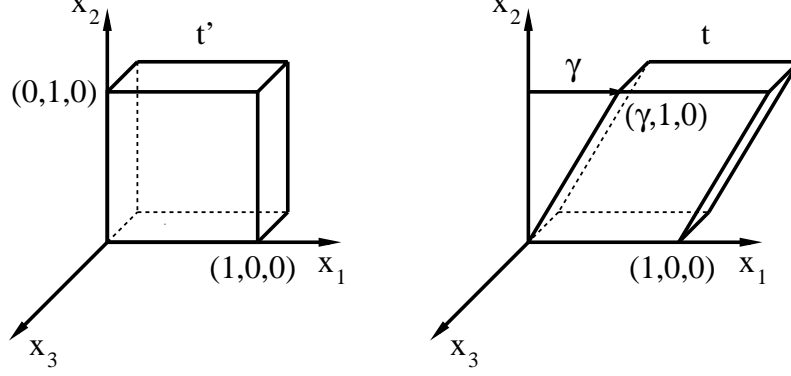


Figure 2.2: Definition of shear.

gradient $\underline{\underline{F}}_t^{-1}(t')$ in shear is given by [6]

$$\underline{\underline{F}}_t^{-1}(t') = \begin{pmatrix} 1 & \gamma(t, t') & 0 \\ 0 & 1 & 0 \\ 0 & 0 & 1 \end{pmatrix} \quad (2.21)$$

with the relative shear deformation $\gamma(t, t')$

$$\gamma(t, t') = \gamma(t) - \gamma(t') \quad (2.22)$$

The relative Finger tensor $\underline{\underline{C}}_t^{-1}(t')$ and the relative Cauchy tensor $\underline{\underline{C}}_t(t')$ in shear are then

$$\underline{\underline{C}}_t^{-1}(t') = \begin{pmatrix} 1 + \gamma^2(t, t') & \gamma(t, t') & 0 \\ \gamma(t, t') & 1 & 0 \\ 0 & 0 & 1 \end{pmatrix} \quad (2.23)$$

$$\underline{\underline{C}}_t(t') = \begin{pmatrix} 1 & -\gamma(t, t') & 0 \\ -\gamma(t, t') & 1 + \gamma^2(t, t') & 0 \\ 0 & 0 & 1 \end{pmatrix} \quad (2.24)$$

For simple shear, the invariants I_1 and I_2 are equal,

$$I_1 = I_2 = 3 + \gamma^2(t, t') \quad (2.25)$$

The velocity gradient $\underline{\underline{\kappa}}$ is given by

$$\underline{\underline{\kappa}} = \underline{\underline{\nabla}} \underline{\underline{v}} = \begin{pmatrix} 0 & \dot{\gamma} & 0 \\ 0 & 0 & 0 \\ 0 & 0 & 0 \end{pmatrix} \quad (2.26)$$

and the rate-of-deformation tensor $\underline{\underline{D}}$ by

$$\underline{\underline{D}} = \frac{1}{2} \begin{pmatrix} 0 & \dot{\gamma} & 0 \\ \dot{\gamma} & 0 & 0 \\ 0 & 0 & 0 \end{pmatrix} \quad (2.27)$$

with $\dot{\gamma}$ being the shear-rate.

If for start-up flow experiments in shear, a material is sheared with a constant shear-rate $\dot{\gamma}$ starting at time $t = 0$,

$$\dot{\gamma} = \begin{cases} 0 & t \leq 0 \\ \dot{\gamma} = \text{const.} & t > 0 \end{cases} \quad (2.28)$$

then the shear viscosity $\eta(\dot{\gamma}, t)$, the first normal stress coefficient $\Psi_1(\dot{\gamma}, t)$, and the second normal stress coefficient $\Psi_2(\dot{\gamma}, t)$ are defined as

$$\eta(\dot{\gamma}, t) = \frac{\sigma_{21}}{\dot{\gamma}} \quad (2.29)$$

$$\Psi_1(\dot{\gamma}, t) = \frac{\sigma_{11} - \sigma_{22}}{\dot{\gamma}^2} = \frac{N_1}{\dot{\gamma}^2} \quad (2.30)$$

$$\Psi_2(\dot{\gamma}, t) = \frac{\sigma_{22} - \sigma_{33}}{\dot{\gamma}^2} = \frac{N_2}{\dot{\gamma}^2} \quad (2.31)$$

with the first normal stress difference $N_1 = \sigma_{11} - \sigma_{22}$, and the second normal stress difference $N_2 = \sigma_{22} - \sigma_{33}$.

$\eta(\dot{\gamma}, t)$, $\Psi_1(\dot{\gamma}, t)$, and $\Psi_2(\dot{\gamma}, t)$ decrease with increasing shear-rate $\dot{\gamma}$, the so-called shear-thinning or softening phenomenon. At long times, $\eta(\dot{\gamma}, t)$, $\Psi_1(\dot{\gamma}, t)$, and $\Psi_2(\dot{\gamma}, t)$ approach constant steady-state values. For small shear-rates, the shear viscosity is equal to the linear-viscoelastic shear viscosity, the so-called zero-shear viscosity $\eta_0(t) = \lim_{\dot{\gamma} \rightarrow 0} \eta(\dot{\gamma}, t)$. Also the normal stress coefficients $\Psi_1(\dot{\gamma}, t)$, and $\Psi_2(\dot{\gamma}, t)$ approach limiting values for small shear-rates, i.e. $\Psi_{1,0}(t) = \lim_{\dot{\gamma} \rightarrow 0} \Psi_1(\dot{\gamma}, t)$ and $\Psi_{2,0}(t) = \lim_{\dot{\gamma} \rightarrow 0} \Psi_2(\dot{\gamma}, t)$ [11].

2.1.4 Extension

Considering a cube with the undeformed side length l at time t' , and a deformed cube with sides l_i ($i = 1, 2, 3$) at time t , the relative Hencky strain $\varepsilon_i = \varepsilon_i(t, t')$ is defined by

$$\varepsilon_i(t, t') = \ln \lambda_i(t, t') = \ln \frac{l_i(t)}{l(t')} = \varepsilon_i(t) - \varepsilon_i(t') \quad (2.32)$$

with the stretch ratio $\lambda_i = \lambda_i(t, t')$.

The Stephenson classification system for extensional flows with constant extensional or strain-rates $\dot{\epsilon}_i$ is described in [51]. Assuming incompressibility, for all extensional flows the relation

$$\dot{\epsilon}_1 + \dot{\epsilon}_2 + \dot{\epsilon}_3 = \nabla \cdot \underline{v} = \text{tr} \underline{D} = 0 \quad (2.33)$$

is valid. A Cartesian coordinate system is chosen in such a way that $\dot{\epsilon}_1 \geq \dot{\epsilon}_2 \geq \dot{\epsilon}_3$, which allows to describe all extensional flows with two parameters, $\dot{\epsilon}$ and m , whereby

$$\dot{\epsilon} = \dot{\epsilon}_1 > 0 \quad (2.34)$$

and

$$m = \frac{\dot{\epsilon}_2}{\dot{\epsilon}_1} \quad (2.35)$$

The values of m are in the range of $-0.5 \leq m \leq 1$. Fig. 2.3 shows how samples change

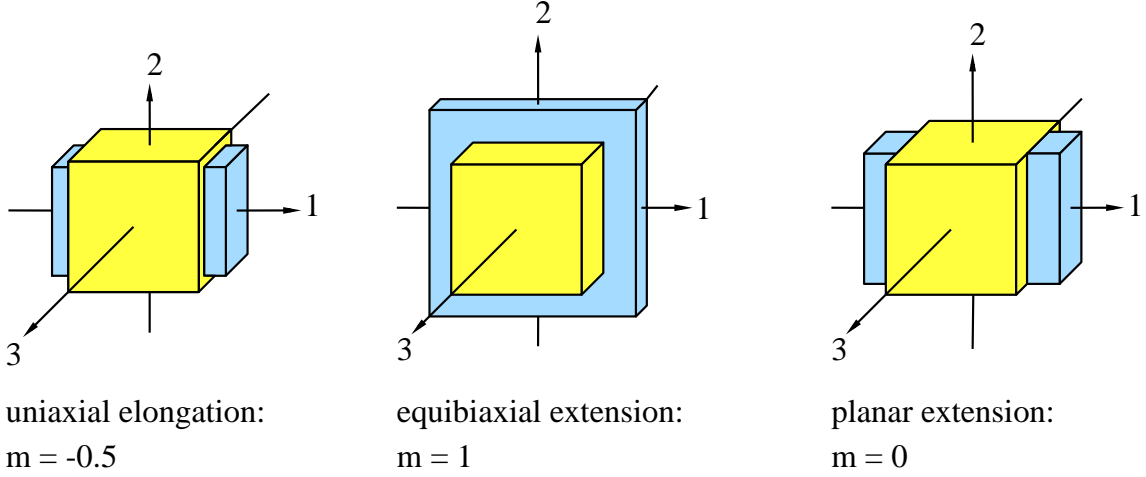


Figure 2.3: Modes of extensional flows.

their shape after simple or uniaxial elongation ($m = -0.5$), equibiaxial extension ($m = 1$), and planar ($m = 0$) extension.

For extensional flows, the rate-of-deformation tensor \underline{D} is equal to the velocity gradient $\underline{\kappa}$

$$\underline{\kappa} = \nabla \underline{v} = \begin{pmatrix} \dot{\epsilon}_1 & 0 & 0 \\ 0 & \dot{\epsilon}_2 & 0 \\ 0 & 0 & \dot{\epsilon}_3 \end{pmatrix} = \dot{\epsilon} \begin{pmatrix} 1 & 0 & 0 \\ 0 & m & 0 \\ 0 & 0 & -(1+m) \end{pmatrix} = \underline{D} \quad (2.36)$$

Hence, extensional flows are also called irrotational flows.

For irrotational flows, the relative inverse deformation gradient $\underline{F}_t^{-1}(t')$,

$$\underline{F}_t^{-1}(t') = \begin{pmatrix} \lambda & 0 & 0 \\ 0 & \lambda^m & 0 \\ 0 & 0 & \lambda^{-(1+m)} \end{pmatrix} = \begin{pmatrix} e^\varepsilon & 0 & 0 \\ 0 & e^{m\varepsilon} & 0 \\ 0 & 0 & e^{-(1+m)\varepsilon} \end{pmatrix} \quad (2.37)$$

is a symmetric tensor. The relative Cauchy tensor $\underline{\underline{C}}_t(t')$ and the relative Finger tensor $\underline{\underline{C}}_t^{-1}(t')$ are then given by

$$\underline{\underline{C}}_t(t') = \begin{pmatrix} \lambda^{-2} & 0 & 0 \\ 0 & \lambda^{-2m} & 0 \\ 0 & 0 & \lambda^{2(1+m)} \end{pmatrix} = \begin{pmatrix} e^{-2\varepsilon} & 0 & 0 \\ 0 & e^{-2m\varepsilon} & 0 \\ 0 & 0 & e^{2(1+m)\varepsilon} \end{pmatrix} \quad (2.38)$$

and

$$\underline{\underline{C}}_t^{-1}(t') = \begin{pmatrix} \lambda^2 & 0 & 0 \\ 0 & \lambda^{2m} & 0 \\ 0 & 0 & \lambda^{-2(1+m)} \end{pmatrix} = \begin{pmatrix} e^{2\varepsilon} & 0 & 0 \\ 0 & e^{2m\varepsilon} & 0 \\ 0 & 0 & e^{-2(1+m)\varepsilon} \end{pmatrix} \quad (2.39)$$

For extensional flows, the first and second invariant are

$$I_1 = e^{2\varepsilon} + e^{2m\varepsilon} + e^{-2(1+m)\varepsilon} \quad (2.40)$$

$$I_2 = e^{-2\varepsilon} + e^{-2m\varepsilon} + e^{2(1+m)\varepsilon} \quad (2.41)$$

I_1 is identical to I_2 for the planar case, which is therefore also called pure shear.

In extensional flows, only normal stresses appear. The state-of-stress can be specified completely by the two normal stress differences $\sigma_1 = \sigma_{11} - \sigma_{33}$ and $\sigma_2 = \sigma_{22} - \sigma_{33}$. The elongational viscosities η_1 and η_2 are then defined as

$$\eta_1 = \frac{\sigma_{11} - \sigma_{33}}{\dot{\varepsilon}} = \frac{\sigma_1}{\dot{\varepsilon}} \quad (2.42)$$

$$\eta_2 = \frac{\sigma_{22} - \sigma_{33}}{\dot{\varepsilon}} = \frac{\sigma_2}{\dot{\varepsilon}} \quad (2.43)$$

Rescaled to the zero-shear viscosity $\eta_0(t)$ [81], the extensional viscosities become

$$\mu_{1,m} = \frac{1}{2(2+m)} \eta_1 \quad (2.44)$$

$$\mu_{2,m} = \frac{1}{2(2m+1)} \eta_2 \quad (2.45)$$

Eqs. (2.42-2.45) define the uniaxial viscosity (η_u or μ_u), the equibiaxial viscosity (η_e or μ_e), the first planar viscosity (η_{p1} or μ_{p1}) in the extensional direction, and the second planar viscosity, the so-called cross-viscosity, (η_{p2} or μ_{p2}) in the neutral direction.

2.2 Linear viscoelasticity

The Boltzmann superposition principle states that the total effect of applying several deformations is the sum of the effects of applying each one separately. It enables the calculation of the stress components resulting from any type of deformation as long as the deformation is small enough. According to the superposition principle, the basic constitutive equation of linear viscoelasticity can be derived by summing the effects of all deformations between times $-\infty$ and t ,

$$\underline{\underline{\sigma}} = -p \underline{\underline{E}} + 2 \int_{-\infty}^t \overset{\circ}{G}(t-t') \underline{\underline{D}}(t') dt' \quad (2.46)$$

$\overset{\circ}{G}(t) = \sigma_{12}/\gamma_0$ is the linear-viscoelastic shear relaxation modulus which describes the stress relaxation after a small step-shear deformation of magnitude γ_0 .

An alternative form of the constitutive equation of linear viscoelasticity is obtained by introducing the linear-viscoelastic memory function $\overset{\circ}{m}(t-t')$,

$$\overset{\circ}{m}(t-t') = d \overset{\circ}{G}(t-t') / dt' \quad (2.47)$$

and integrating Eq. (2.46),

$$\underline{\underline{\sigma}} = -p \underline{\underline{E}} + 2 \int_{-\infty}^t \overset{\circ}{m}(t-t') \underline{\underline{\epsilon}}_t(t') dt' \quad (2.48)$$

Linear viscoelasticity can be modelled by considering several Maxwell models consisting of linear spring elements with moduli g_i and viscous dashpot elements with constant viscosities η_i which are connected in series as shown in fig. 2.4 [21]. Liquids with memory possess viscous as well as elastic properties. Viscosities η_i and moduli g_i define relaxation times $\tau_i = \eta_i/g_i$. Introducing a discrete spectrum of relaxation times,

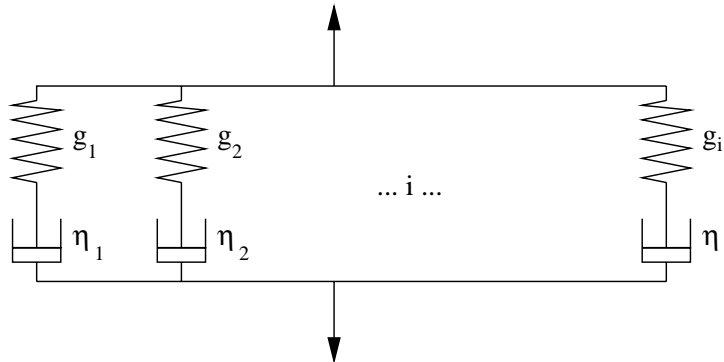


Figure 2.4: Maxwell model [21].

Eq. (2.46) can be expressed as

$$\underline{\underline{\sigma}} = -p \underline{\underline{E}} + 2 \int_{-\infty}^t \sum_i g_i e^{-(t-t')/\tau_i} \underline{\underline{D}}(t') dt' \quad (2.49)$$

The most common way of determining the spectrum of relaxation times is small amplitude oscillatory shear deformation in the cone-and-plate geometry. A sample is subjected to a sinusoidal shear deformation

$$\gamma = \gamma_0 \sin \omega t \quad (2.50)$$

where γ_0 is the strain amplitude and ω the frequency. The response of the shear stress to such a strain history is

$$\underline{\underline{\sigma}} = \gamma_0 [G'(\omega) \sin \omega t + G''(\omega) \cos \omega t] \quad (2.51)$$

The shear stress is proportional to the strain amplitude γ_0 , if γ_0 is small enough. G' is called the storage modulus and is in phase with the strain, G'' is the loss modulus and in phase with the strain-rate. A complete elastic material stores all mechanical energy ($G'' = 0$), a Newtonian liquid dissipates all mechanical energy ($G' = 0$). For a discrete relaxation spectrum, G' and G'' are given by [21]

$$G'(\omega) = \sum_i g_i \frac{\omega^2 \tau_i^2}{\omega^2 \tau_i^2 + 1} \quad (2.52)$$

$$G''(\omega) = \sum_i g_i \frac{\omega \tau_i}{\omega^2 \tau_i^2 + 1} \quad (2.53)$$

For viscoelastic fluids, the time-dependent linear-viscoelastic shear relaxation modulus $\overset{\circ}{G}(t)$ decreases monotonically with increasing time (i.e. viscoelastic liquids show a "fading memory") and is given by

$$\overset{\circ}{G}(t) = \sum_i g_i e^{-t/\tau_i} \quad (2.54)$$

The memory function $\overset{\circ}{m}(t)$ can then be expressed by

$$\overset{\circ}{m}(t) = \sum_i \frac{g_i}{\tau_i} e^{-t/\tau_i} \quad (2.55)$$

The linear-viscoelastic zero-shear viscosity $\eta_0(t)$ for start-up of steady shear flow is calculated from Eq. (2.49),

$$\eta_0(t) = \sum_i g_i \tau_i (1 - e^{-t/\tau_i}) \quad (2.56)$$

$\eta_0(t)$ forms an envelope for all shear viscosities $\eta(\dot{\gamma}, t)$ (Eq. (2.29)) measured in start-up of steady shear flow experiments [11].

Also for small constant shear-rates, the second order limit of the first normal stress coefficient $\Psi_1(\dot{\gamma}, t)$ (Eq. (2.30)), can be calculated from Eq. (2.49)

$$\Psi_{1,0}(t) = 2 \sum_i g_i \tau_i^2 \left(1 - \left(1 + \frac{t}{\tau_i}\right) e^{-t/\tau_i}\right) \quad (2.57)$$

which forms an envelope for all first normal stress coefficients $\Psi_1(\dot{\gamma}, t)$ [11].

Rheological properties are temperature-dependent [12]. Measurements of G' and G'' at different temperatures can be shifted onto a single master curve by use of the principle of "time-temperature superposition". For polymer melts, the shift factor a_T for shift of data measured at the test temperature T , to the reference temperature T_0 can be calculated by the Arrhenius equation with an activation energy E_a , an activation energy for flow [12], which is valid for temperatures higher than 100 K above the glass transition temperature.

For relaxation times $\tau_{i,T}$ at test temperature T and τ_{i,T_0} at reference temperature T_0 , the shift factor a_T is

$$\ln\left(\frac{\tau_{i,T}}{\tau_{i,T_0}}\right) = \ln a_T = \frac{E_a}{\mathcal{R}} \left(\frac{1}{T} - \frac{1}{T_0}\right) \quad (2.58)$$

\mathcal{R} is the ideal gas constant.

There is also a shift factor b_T in the vertical direction, which takes into account the temperature-dependent change in density and modulus,

$$\ln\left(\frac{\rho_{T_0} T_0}{\rho_T T}\right) = \ln b_T = \frac{E_b}{\mathcal{R}} \left(\frac{1}{T} - \frac{1}{T_0}\right) \quad (2.59)$$

ρ_{T_0} is the density at T_0 , and ρ_T the density at T . The activation energy E_b is determined experimentally by measurements at different temperatures. b_T is often neglected; however, as shown in [27], it should not be neglected.

2.3 Network models

2.3.1 Entropy elasticity

The theory of entropy elasticity [73], [72] is developed for rubber by considering a three-dimensional network model consisting of flexible, long-chain molecules which are connected permanently by chemical bonds. Although the topology of the network is fixed by chemical cross-links, the molecular strands between the cross-links are free to move which allows for an enormous number of conformations due to random thermal (Brownian) motion of the chain elements. Already a small number of cross-links between chains forms a coherent network with only weak forces between the molecules. The given test macromolecule will be continually changing its conformation in a very short time. Therefore, it is necessary to characterise the statistical

properties of the long-chain molecule by an idealised model, the freely jointed chain (fig. 2.5). The freely jointed chain between two cross-links contains n_0 links of equal length b , the so-called Kuhn segments, and is described by its end-to-end vector \underline{r} , involving the distance between two cross-links $|\underline{r}|$ and the completely random direction in space of the chain. The cross-links are separated on average by a distance $a_0 = |\underline{r}|$ at equilibrium. Of interest are the time-averaged values of the end-to-end distance, $\sqrt{\langle \underline{r}^2 \rangle}$, which are fluctuating wildly with time.

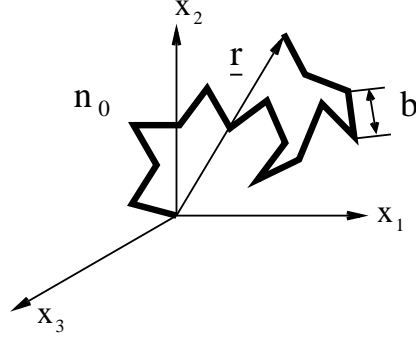


Figure 2.5: The freely jointed chain.

The probability $P_r(r) dr$ to find a chain with end-to-end distance between $|\underline{r}|$ and $|\underline{r} + d\underline{r}|$ is independent of the orientation of the end-to-end vector \underline{r} and is given by a Gaussian distribution function $\psi_0(r)$ [73], if $|\underline{r}| \ll n_0 b$,

$$P_r(r) dr = \psi_0(r) d^3 r = \left(\frac{3}{2\pi n_0 b^2} \right)^{3/2} \exp\left(-\frac{3r^2}{2n_0 b^2} \right) d^3 r \quad (2.60)$$

ψ_0 is the isotropic distribution function at equilibrium. The square of the average distance a_0 is then given by

$$a_0^2 = \langle \underline{r}^2 \rangle_0 = \int \psi_0(r) \underline{r}^2 d^3 r = n_0 b^2 \quad (2.61)$$

If the end-to-end distance is increased, the increase of the Helmholtz free energy dW can either be caused by an increase of the internal energy dU or by a decrease of the entropy dS ,

$$dW = dU - TdS \quad (2.62)$$

According to the assumption of a freely jointed chain, the change of the internal energy dU is zero, and the stress results from a decrease of the entropy only

$$S = k \ln \psi_0(r) = \text{constant} - \frac{3kr^2}{2n_0 b^2} \quad (2.63)$$

which simplifies Eq. (2.62) to

$$dW = \frac{3kT}{n_0 b^2} \underline{r} \cdot d\underline{r} \quad (2.64)$$

with the Boltzmann constant k .

Differentiating the free energy W with respect to the vector \underline{r} , the force $\underline{K}(\underline{r})$, which acts on the chain ends, can be derived as

$$\underline{K}(\underline{r}) = \frac{dW}{d\underline{r}} = \frac{3kT}{n_0 b^2} \underline{r} = \frac{3kT}{\langle r^2 \rangle_0} \underline{r} \quad (2.65)$$

Eq. (2.65) gives the tension in a single polymer strand. To derive the stress for a network consisting of an enormous number of molecular strands, the following assumptions have to be made [73]:

1. The network contains N_0 chain segments per unit volume. (A chain segment is defined as a segment of a macromolecule between two successive points of cross-links.)
2. The mean-square end-to-end distance for all chain segments in the undeformed state of the network is equal to a corresponding set of free chains.
3. The volume remains constant and the cross-links move affinely with the macroscopic deformation.
4. The entropy of the network is the sum of the entropies of each single chain according to Eq. (2.63).

Due to the affine deformation assumption, the undeformed end-to-end vector \underline{r}_0 is transformed by the inverse deformation gradient \underline{F}_t^{-1} to the deformed vector \underline{r}

$$\underline{r} = \underline{F}_t^{-1} \cdot \underline{r}_0 = \sqrt{\langle r^2 \rangle_0} \cdot \underline{F}_t^{-1} \cdot \underline{u} = \sqrt{\langle r^2 \rangle_0} \underline{u}' \quad (2.66)$$

which can also be expressed by introducing the unit vector \underline{u} and the deformed unit vector $\underline{u}' = \underline{F}_t^{-1} \cdot \underline{u}$. The stress tensor of this network model is given by [5]

$$\underline{\sigma} = -p\underline{E} + N_0 \langle \underline{K} \underline{r} \rangle = -p\underline{E} + 3N_0 kT \langle \underline{u}' \underline{u}' \rangle \quad (2.67)$$

where $\langle \dots \rangle$ denotes an integral over an isotropic distribution of unit vectors before deformation.

It can be shown that $3\langle \underline{u}' \underline{u}' \rangle$ is equal to the Finger tensor $\underline{C}_t^{-1}(n)$ with n indicating the undeformed, stress-free state [66]. Thus, the classical constitutive equation of a neo-Hookean elastic solid is obtained as

$$\underline{\sigma} = -p\underline{E} + N_0 kT \underline{C}_t^{-1}(n) \quad (2.68)$$

which introduces a linear relation between the stress tensor $\underline{\sigma}$ and the Finger tensor $\underline{C}_t^{-1}(n)$. Eq. (2.68) allows a qualitative description of experimental stress-strain measurements of rubbers with deviations at large and small deformations. At large deformations, the Gaussian distribution fails because the chain length is limited. At small deformations, intermolecular interactions, which are not considered in the classical theory, lead to deviations between experimental results and theory.

2.3.2 Rubberlike-liquid theory

Polymeric melts behave not only elastic but also viscous. For this reason, Lodge extended the theory of neo-Hookean elasticity to polymeric melts by "liquifying" the rubber. For this purpose, he made the following additional assumptions [36]:

5. The network cross-links are no longer chemical junctions, but physical junctions ("entanglements"). A physical junction is defined as "a connection between two chains which are constraint in such a way that the link points move together for at least a minimum length of time greater than the fluctuation period τ^* " [36]. Junctions are dissolved and reformed immediately due to their thermal motion. Hence, network segments are characterised by creation rates N_i^* and loss rates τ_i . i denotes network strands of type i .
6. Upon creation, network strands have an isotropic distribution function.
7. N_i^* and τ_i are constant.

Assumptions 5 and 7 lead to a differential equation describing the loss of junctions [76]:

$$\frac{dN_i(t, t')}{dt} + \frac{1}{\tau_i} N_i(t, t') = 0 \quad (2.69)$$

If $N_i^* dt'$ chains of type i are created between times t' and $t' + dt'$, the number of chains $N_i(t, t') dt'$ of type i per unit volume at time t is obtained by integration of Eq. (2.69),

$$N_i(t, t') dt' = N_i^* \exp\left(-\frac{t-t'}{\tau_i}\right) dt' \quad (2.70)$$

Replacing N_0 in Eq. (2.68) by Eq. (2.70) and n by t' , and integrating from $-\infty$ to t results in the stress tensor of the rubberlike liquid,

$$\underline{\underline{\sigma}} = -p \underline{\underline{E}} + \int_{-\infty}^t kT \sum_i N_i^* \exp\left(-\frac{t-t'}{\tau_i}\right) \underline{\underline{C}}_t^{-1}(t') dt' \quad (2.71)$$

Contributing to the stress are only those chains which have experienced a deformation described by the relative Finger tensor $\underline{\underline{C}}_t^{-1}(t')$, and which still exist at time t . Due to the fading memory, deformations in the distant past are less relevant for the state-of-stress than deformations in the near past.

Introducing the memory function $\overset{\circ}{m}(t-t')$ (Eq. (2.47)),

$$\overset{\circ}{m}(t-t') = \frac{\partial \overset{\circ}{G}(t-t')}{\partial t'} = kT \sum_i N_i^* \exp\left(-\frac{t-t'}{\tau_i}\right) \quad (2.72)$$

the rubber-liquid constitutive equation of Lodge can be expressed as [76]

$$\underline{\underline{\sigma}} = -p \underline{\underline{E}} + \int_{-\infty}^t \overset{\circ}{m}(t-t') \underline{\underline{C}}_t^{-1}(t') dt' \quad (2.73)$$

For infinitesimal deformations, this constitutive equation reduces to the equation of linear viscoelasticity, Eq. (2.46). Eq. (2.73) qualitatively predicts many of the phenomena of viscoelastic flow [32], i.e. the first normal stress difference in shear, gradual stress relaxation after cessation of flow, elastic recovery of strain and strain-hardening in elongation. Major problems of the rubber-liquid constitutive equation of Lodge are that it does not describe a shear thinning viscosity and that it overemphasises elasticity of viscoelastic fluids, i.e. it overpredicts elastic stresses and elastic recoverable strains [83].

2.3.3 Damping function

The rubberlike-liquid theory overpredicts the stress of polymer melts because three assumptions of this theory are questionable [76], i.e. the assumption of affine deformation, of isotropy of the distribution function and of constant creation and loss rates. Modifying the last assumption, Wagner suggested that there exist 'two independent decay mechanisms for network strands of type i' [83], namely

1. the linear-viscoelastic (time-dependent) relaxation with decay probability $1/\tau_i$,
2. decay of network junctions with increasing deformation due to disentanglement.

The probability $h(I_1, I_2)$ for a network strand to survive a certain deformation was assumed to depend on scalar measures of the deformation, i.e. the first (I_1) and second (I_2) invariant of the Finger tensor. As $0 < h(I_1, I_2) \leq 1$, $h(I_1, I_2)$ describes an additional damping of the memory of a rubberlike liquid with increasing deformation, $h(I_1, I_2)$ was called "damping function".

The constitutive equation of the modified rubberlike-liquid theory is given by [76]

$$\underline{\underline{\sigma}} = -p \underline{\underline{E}} + \int_{-\infty}^t \overset{\circ}{m}(t-t') h(I_1, I_2) \underline{\underline{C}}_t^{-1} dt' \quad (2.74)$$

Eq. (2.74) is also called the "Wagner I" equation [32]. Wagner [76] showed that Eq. (2.74) describes shear viscosity η and first normal stress coefficient Ψ_1 as well as elongational data quantitatively, but it does not allow to predict the second normal stress coefficient Ψ_2 . Furthermore, Demarmels and Meissner [13] demonstrated that a linear combination of I_1 and I_2 cannot describe multiaxial extensions and shear simultaneously.

The damping function $h(I_1, I_2)$ depends only on deformation and is temperature-independent. While the memory function $\overset{\circ}{m}(t - t')$ can be determined from the linear-viscoelastic relaxation spectrum, $h(I_1, I_2)$ has to be determined by appropriate non-linear experiments.

One possibility are relaxation tests in which the polymer melt is subjected to various step-strains at time $t = 0$. The corresponding stress relaxation is from Eq. (2.74),

$$\underline{\underline{\sigma}}(t) = -p \underline{\underline{E}} + \overset{\circ}{G}(t) h(I_1, I_2) \underline{\underline{C}}_t^{-1}(0) \quad (2.75)$$

By measuring the non-linear relaxation modulus $G(t, I_1, I_2)$ at large step-strains,

$$G(t, I_1, I_2) = \overset{\circ}{G}(t) h(I_1, I_2) \quad (2.76)$$

the damping function can be determined from the ratio of the non-linear to the linear relaxation modulus [76],

$$h(I_1, I_2) = \frac{G(t, I_1, I_2)}{\overset{\circ}{G}(t)} \quad (2.77)$$

Step-strain experiments are usually used to determine the damping function for simple shear flow.

Another possibility to determine $h(I_1, I_2)$ are start-up flow experiments in which the sample is deformed at a constant deformation rate. The stress tensor is then from Eq. (2.74),

$$\underline{\underline{\sigma}} = -p \underline{\underline{E}} + \int_0^t \overset{\circ}{m}(t - t') h(t - t') \underline{\underline{C}}_t^{-1}(t - t') d(t - t') + h(t) \overset{\circ}{G}(t) \underline{\underline{C}}_t^{-1}(0) \quad (2.78)$$

By partial integration and solving for $h(t)$, the damping function can be calculated from measured data by [76]

$$h(t) = \frac{\frac{[\underline{\underline{\sigma}} + p \underline{\underline{E}}]_{ij}}{\overset{\circ}{G}(t)} - \int_0^t [\underline{\underline{\sigma}} + p \underline{\underline{E}}]_{ij} \frac{\overset{\circ}{m}(t')}{\overset{\circ}{G}^2(t')} dt'}{[\underline{\underline{C}}_t^{-1}(0)]_{ij}} \quad (2.79)$$

Start-up flow experiments are mainly used to determine damping functions in extensional flows.

Several possibilities exist to fit the damping functions to deformation-dependent approximation functions, i.e. by a single exponential function or a linear combination of exponential functions [33], [76] or by functions of a sigmoidal form [57].

2.4 Tube models

Doi and Edwards (1978) [18], [19] developed a non-linear strain measure from a molecular theory which is based on the tube model introduced by Edwards (1968). In combination with the reptation theory of de Gennes (1971), this model predicts a specific linear-viscoelastic relaxation spectrum for monodisperse melts. Here, only the non-linear aspects of the tube model are considered.

Polymer chains cannot pass freely through each other. Surrounding chains act as topological constraints, and confine each chain inside a tube-like region (fig. 2.6). Hence, a macromolecular chain cannot move laterally, but only longitudinally within the tube. The tube model is characterised by the equilibrium (i.e. "no-flow") tube diameter a_0 .

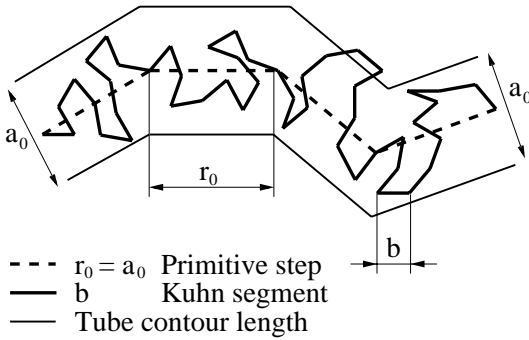


Figure 2.6: Tube model in equilibrium

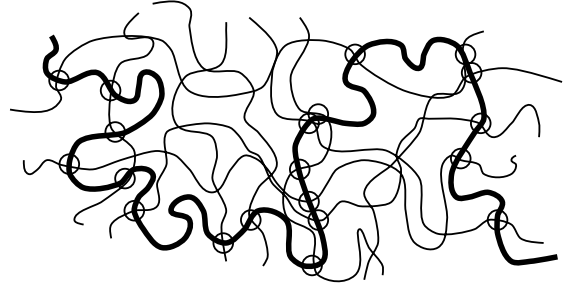


Figure 2.7: Slip-link model

The number n of Kuhn segments of length b ("monomer units") which are found per length l of the tube, i.e. the line density n/l , is related to the tube diameter a_0 by

$$n/l = a_0/b^2 \quad (2.80)$$

The centre line of the tube, called the primitive path by Doi and Edwards [18], is a random walk with a primitive step length r_0 corresponding to a_0 . The real chain is wriggling around the primitive chain.

According to Doi and Edwards, stress relaxation after a step-strain deformation occurs by two different mechanisms. Firstly, after deformation the chain retracts fast by equilibrating along the tube contour and secondly, the chain diffuses out of the chain by reptation. The first relaxation process in a stress relaxation experiment is schematically represented in fig. 2.8. In the undeformed state $t < 0$, the chain is at equilibrium. Immediately after deformation ($t \geq 0$), the polymer chain is stretched affinely within the affinely deformed tube. Shortly after deformation, the polymer molecule relaxes to its original length L_0 by the first, very rapid relaxation mechanism. This relaxation process is terminated at a time T_{eq} which depends on the square of the molecular weight ($T_{eq} \sim M^2$). Then, the second, very slow relaxation process occurs. Due to thermal motion, the polymer chain reptates longitudinally within the tube. In doing so, the

chain ends evacuate the deformed and thereby oriented tube, and form, constrained by surrounding chains, a new, randomly oriented tube. The time-dependent percentage

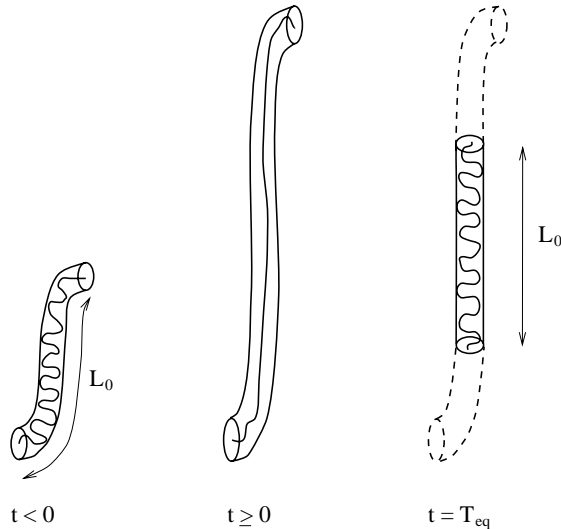


Figure 2.8: Tube model in the stress relaxation experiment

of the deformed tube which is still occupied by the macromolecule at a time t (with $t \geq T_{eq}$) and which gives a contribution to the stress tensor is given by [9]

$$P_i(t) = \sum_{i \text{ odd}} \frac{8}{\pi^2 i^2} \cdot e^{-\frac{i^2 t}{T_d}} \quad (2.81)$$

After a disengagement time T_d , the polymer chain has completely evacuated the original tube, and the stress has completely relaxed. According to reptation theory, T_d depends on the third power of the molecular weight ($T_d \sim M^3$). Since the dependence of T_{eq} on molecular weight M is only quadratic, and M is a large number, T_d and T_{eq} represent widely different time scales, which explains why polymer melts show time/deformation separability.

Alternatively, the constraints formed by surrounding chains can be modelled as slip-links (fig. 2.7) [19]. Slip-links are small rings through which the chain can reptate freely and which are separated randomly by a distance $r_0 = a_0$ (corresponding to the tube diameter). Wagner and Schaeffer implemented the slip-link idea into the rubberlike-liquid theory [84], [85]: At equilibrium, a network strand between two slip-links contains n_0 monomer units of length b (fig. 2.9),

$$n_0 b^2 = a_0 r_0 = a_0^2 \quad (2.82)$$

The orientation distribution of network strands is isotropic. The mean field of surrounding chains is equivalent to an equilibrium force \underline{K}_{eq} which acts on the chain ends and is given with Eqs. (2.61) and (2.65) by

$$\underline{K}_{eq} = \frac{3kT}{n_0 b^2} \underline{r}_0 = \frac{3kT}{a_0 r_0} \underline{r}_0 = \frac{3kT}{a_0} \underline{u} \quad (2.83)$$

The vector $\underline{r}_0 = a_0 \underline{u}$ joins two slip-links in equilibrium conformation, with \underline{u} being the unit vector, k the Boltzmann constant and T the absolute temperature.

The stress tensor $\underline{\underline{\sigma}}$ at equilibrium, derived from Eq. (2.67), is given by

$$\underline{\underline{\sigma}} = -p\underline{\underline{E}} + 3N_0kT\langle\underline{u}\underline{u}\rangle_0 = -p\underline{\underline{E}} + N_0kT\underline{\underline{E}} \quad (2.84)$$

with N_0 the number of tube segments per polymer chain. $\langle\dots\rangle_0$ denotes an average over an isotropic distribution function, $\psi_0 = 1/(4\pi)$, of unit vectors \underline{u} and can be expressed as a surface integral over the unit sphere [19],

$$\langle\dots\rangle_0 = \frac{1}{4\pi} \oint \int [\dots] \sin\Theta_0 d\Theta_0 d\varphi_0 \quad (2.85)$$

Eq. (2.84) demonstrates that the stress tensor is isotropic at equilibrium.

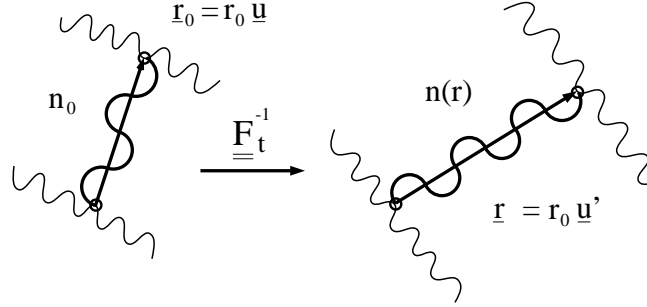


Figure 2.9: Vector \underline{r} joining two slip-links after deformation

Considering now a step deformation at time $t = 0$, and assuming an affine deformation of the slip-links, the vector \underline{r}_0 joining two slip-links is transformed by the relative deformation gradient $\underline{\underline{F}}_t^{-1}$ into the vector \underline{r} (fig. 2.9)

$$\underline{r} = \underline{\underline{F}}_t^{-1} \cdot \underline{r}_0 = a_0 \underline{\underline{F}}_t^{-1} \cdot \underline{u} = a_0 \underline{u}' \quad (2.86)$$

The polymer molecules slide through the slip-links. Consequently, the number of Kuhn segments n_0 between two slip-links will change to $n(r)$, depending on the distance $r = |\underline{r}| = a_0 |\underline{u}'| = a_0 u'$. The slip occurs during the first, fast relaxation process and is characterised by a slip-function $S(r)$ describing the degree of slip. Relating the number of Kuhn segments $n(r)$ between two slip-links after deformation to the number n_0 before deformation, $S(r)$ can be defined as

$$S(r) = n(r)/n_0 \quad (2.87)$$

The force $\underline{K}(\underline{r})$ in the chain between two slip-links after the step deformation can be derived from Eq. (2.83) with Eqs. (2.82) and (2.87),

$$\underline{K}(\underline{r}) = \frac{3kT}{n(r)b^2} \underline{r} = \frac{3kT}{S(r)a_0} \underline{u}' \quad (2.88)$$

Some of the tube segments are destroyed by deformation not only at the chain ends, but also along the chain because of constraint release. Starting at equilibrium with $N_0 d\Omega/4\pi$ chain segments in a space angle $d\Omega/4\pi$, the number of chain segments which survive a given deformation is described by $N(r)d\Omega/4\pi$. $N(r)$ is a unique function of the distance $\underline{r} = a_0 \underline{u}$ of two slip-links. Considering the mass balance, $N(r)$ and $n(r)$ are related by

$$\langle N(r)n(r) \rangle = N_0 n_0 = P_0 \quad (2.89)$$

in which P_0 is the degree of polymerisation (the total number of monomer units in a chain). The disentanglement function $D(r)$ is the relation of the number of chains ($N(r)$) after deformation to the one (N_0) before deformation, and expresses the degree of disentanglement,

$$D(r) = \frac{N(r)}{N_0} \quad (2.90)$$

Eq. (2.89) relates the disentanglement function $D(r)$ to the slip-function $S(r)$,

$$\langle D(r) \cdot S(r) \rangle = 1 \quad (2.91)$$

The stress tensor for times $t = T_{eq}$ is given by

$$\underline{\underline{\sigma}}(T_{eq}) = -p\underline{\underline{E}} + 3N_0 kT \langle (D(r)/S(r)) \underline{u}' \underline{u}' \rangle_0 \quad (2.92)$$

Introducing the percentage $P_t(t)$ of still occupied tube into Eq. (2.92), the stress relaxation can be described by

$$\underline{\underline{\sigma}}(t) = -p\underline{\underline{E}} + 3N_0 kT P_t(t) \langle (D(r)/S(r)) \underline{u}' \underline{u}' \rangle_0 \quad (2.93)$$

The time-dependent linear relaxation modulus $\overset{\circ}{G}(t)$ is given by

$$\overset{\circ}{G}(t) = 3N_0 kT P_t(t) g^{-1} \quad (2.94)$$

with the norm g^{-1}

$$g^{-1} = \lim_{\underline{\underline{E}}_t^{-1} \rightarrow \underline{\underline{E}}} \langle (D(r)/S(r)) \underline{u}' \underline{u}' \rangle_0 : \langle (D(r)/S(r)) \underline{u}' \underline{u}' \rangle_0 \quad (2.95)$$

Defining the non-linear strain measure $\underline{\underline{S}}_t$,

$$\underline{\underline{S}}_t = g \langle (D(r)/S(r)) \underline{u}' \underline{u}' \rangle_0 \quad (2.96)$$

the stress tensor $\underline{\underline{\sigma}}$ is given by

$$\underline{\underline{\sigma}}(t) = -p\underline{\underline{E}} + \overset{\circ}{G}(t) \underline{\underline{S}}_t \quad (2.97)$$

With the side condition of Eq. (2.91), Eq. (2.97) contains the constitutive equations of Lodge and Wagner I [84]: Assuming no slip (i.e. $S(r) = 1$) and no disentanglement (i.e. $D(r) = 1$), Eq. (2.97) becomes Lodge's rubberlike-liquid constitutive equation with $\underline{\underline{S}}_t = 3 \langle \underline{u}' \underline{u}' \rangle_0 = \underline{\underline{C}}_t^{-1}$.

Assuming an independence of slip and disentanglement on segmental orientation, Eq. (2.91) reduces to

$$\langle D(r) \cdot S(r) \rangle = D(r) \cdot S(r) = 1 \quad (2.98)$$

and hence, the non-linear strain measure $\underline{\underline{S}}_t$ can be expressed by

$$\underline{\underline{S}}_t = g D^2(r) \langle \underline{u}' \underline{u}' \rangle_0 = D^2(r) \underline{\underline{C}}_t^{-1} = h(I_1, I_2) \underline{\underline{C}}_t^{-1} \quad (2.99)$$

$h(I_1, I_2)$ is the damping function which was introduced phenomenologically by Wagner (chapt. 2.3.3) and is now seen to be due to an isotropic disentanglement of polymer chains.

2.4.1 Doi-Edwards theory

The basic assumption of the Doi-Edwards (DE) theory is that the force \underline{K} in the deformed polymer chain is equal to the force at equilibrium, \underline{K}_{eq} ,

$$|\underline{K}| = |\underline{K}_{eq}| \quad (2.100)$$

i.e. that there is no change of the tube diameter with deformation.

With the assumption that the line density $n(r)/r$ for $t \geq T_{eq}$ is equal to the equilibrium line density n_0/r_0 , or that the tube radius remains constant $a = a_0$, the slip-function is given by

$$S(r) = \frac{n(r)}{n_0} = \frac{a r}{a_0 r_0} = \frac{r}{r_0} = |\underline{u}'| = u' \quad (2.101)$$

Since the degree of polymerisation does not change, $D(r)$ can be obtained from Eq. (2.91),

$$\langle D(r) \cdot S(r) \rangle = \langle D(r) \cdot u' \rangle_0 = 1 \quad (2.102)$$

Doi and Edwards considered two different solutions of Eq. (2.102):

(1) Assuming that disentanglement appears only at the chain ends, leads to an isotropic disentanglement function $D(r)$,

$$D(r) = \frac{1}{\langle S(r) \rangle} = \frac{1}{\langle u' \rangle_0} \quad (2.103)$$

and to a non-linear strain measure $\underline{\underline{S}}_{DE}$

$$\underline{\underline{S}}_{DE} = \frac{g}{\langle u' \rangle_0} \left\langle \frac{\underline{u}' \underline{u}'}{u'} \right\rangle_0 \quad (2.104)$$

with $g = 15/4$.

(2) Assuming that the tube segments deform independently, (the so-called "Independent Alignment (IA) assumption") [19], the disentanglement function $D(r)$ becomes

$$D(r) = \frac{1}{S(r)} = \frac{1}{u'} \quad (2.105)$$

and the non-linear strain measure $\underline{\underline{S}}_{DE}^{IA}$ is given by

$$\underline{\underline{S}}_{DE}^{IA} = g \left\langle \frac{u'u'}{u'^2} \right\rangle_0 = g \underline{\underline{S}} \quad (2.106)$$

with $g = 15/3 = 5$ and $\underline{\underline{S}}$ being the second order orientation tensor. The stress tensor of the Doi-Edwards (DE) theory (with the IA assumption) is then

$$\underline{\underline{\sigma}}(t) = -p \underline{\underline{E}} + \int_{-\infty}^t \overset{\circ}{m}(t-t') \underline{\underline{S}}_{DE}^{IA}(t') dt' \quad (2.107)$$

The linear-viscoelastic memory function $\overset{\circ}{m}(t-t')$ can be expressed as

$$\overset{\circ}{m}(t-t') = \frac{\partial \overset{\circ}{G}(t-t')}{\partial t'} = \frac{G_N^0}{5} \frac{\partial P(t-t')}{\partial t'} \quad (2.108)$$

$G_N^0 = 3ckTb^2/a_0^2$ is the plateau modulus defined by the rubber elasticity theory [73]. c is the concentration of polymer in the material, k the Boltzmann constant, and T the absolute temperature.

2.4.2 Modifications of the Doi-Edwards theory

The material behaviour of monodisperse polymer solutions in step-shear strain experiments can be predicted by the non-linear strain measure $\underline{\underline{S}}_{DE}^{IA}$ of Doi and Edwards. For polydisperse linear and branched melts, it was found that the stress in shear flow and extensional flows is underpredicted by $\underline{\underline{S}}_{DE}^{IA}$, and that no prediction of a maximum in the normal stress is possible [86]. For this reason, many modifications of the DE tube model were developed with the aim to remove these discrepancies.

Rate-dependent stretch equations

Taking into account the discrepancies between the original DE theory and non-linear experiments of polydisperse melts, Doi and Edwards (1986) [17] introduced a dependence of the stress tensor not only on orientation, but on stretch of the contour length. This stretch process is expressed by the stretch ratio $\lambda = L/L_0$, with L_0 being the

length of the primitive path at equilibrium and L after deformation. Both the tensile force and the stretch are assumed to be uniform along the chain. With the stretch being dependent on the observation time t , the stress tensor $\underline{\underline{\sigma}}(t)$ is defined as

$$\underline{\underline{\sigma}}(t) = -p \underline{\underline{E}} + \lambda^2(t) \int_{-\infty}^t \overset{\circ}{m}(t-t') \underline{\underline{S}}_{DE}^{IA} dt' \quad (2.109)$$

Pearson et al. (1989) [59] introduced a stretch evolution equation

$$\frac{\partial \lambda}{\partial t} = (\underline{\underline{\kappa}} : \underline{\underline{S}}_{dyn}(t)) \lambda - \frac{1}{\tau_R} (\lambda - 1) \quad (2.110)$$

where $\underline{\underline{\kappa}}$ is the velocity gradient and $\underline{\underline{S}}_{dyn}$ a dynamical variable describing the orientation of tube segments. The first part of the right hand side of Eq. (2.110) takes into account the affine stretch of the tube segments due to the drag of the surroundings. The second part governs a stretch relaxation process with a Rouse time τ_R . This stretch evolution equation allows to describe the overshoot in both the first normal stress difference and the shear stress. However, the strain-hardening behaviour of extensional flows is not predicted if the strain-rate $\dot{\epsilon}_0$ is smaller than the inverse Rouse time $1/\tau_R$.

McLeish and Larson (1998) [41] derived a constitutive equation, based on Eq. (2.109), for a specially-branched molecule, the pom-pom. The pom-pom is supposed to be a model for long-chain-branched polyethylene. A typical pom-pom molecule consists of a backbone which connects two branch points each of q dangling arms (fig. 2.10). The backbone is confined inside a tube which is formed by other backbones. For

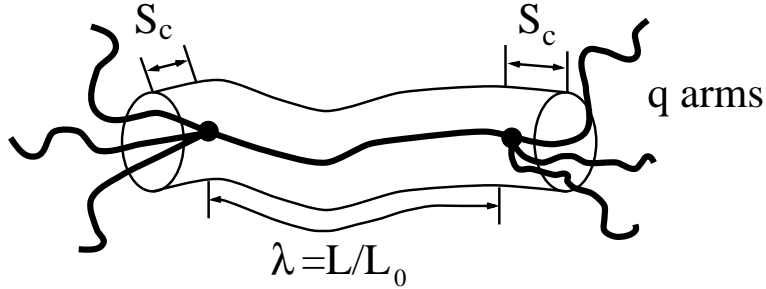


Figure 2.10: Pom-pom model [41]

extensional flows, the backbone can easily be stretched in such a way that it produces strain-hardening, while for shear flows the stretch is only temporary and leads to strain-softening. The configurational distribution of the molecule is defined by three dynamical variables, $\underline{\underline{S}}_{dyn}(t)$, λ , and S_c . $\underline{\underline{S}}_{dyn}(t)$ describes the orientation of tube segments by measuring the distribution of unit vectors

$$\underline{\underline{S}}_{dyn}(t) = \int_{-\infty}^t \frac{dt'}{\tau_b(t')} \exp \left\{ - \int_{t'}^t \frac{dt''}{\tau_b(t'')} \right\} \underline{\underline{S}}_t(t') \quad (2.111)$$

with the second order orientation tensor $\underline{\underline{S}}$ (Eq. (2.106)). The stretch ratio λ of the path length of the backbone to its equilibrium length is again given by Eq. (2.110), but with the Rouse relaxation time τ_R being replaced by τ_S ,

$$\frac{\partial \lambda}{\partial t} = (\underline{\underline{k}} : \underline{\underline{S}}_{dyn}(t))\lambda - \frac{1}{\tau_S}(\lambda - 1), \quad \lambda \leq \lambda_{max} = q \quad (2.112)$$

τ_S is a characteristic stretch relaxation time. The maximum stretch λ_{max} cannot exceed the number q of arms, because it is directly proportional to the tension in the backbone. If the maximum stretch of the backbone is reached, the tension in the backbone is large enough to draw the arms into the tube within a length S_c on each side (fig. 2.10), the so-called branchpoint withdrawal. Both, λ and S_c are time-dependent.

The pom-pom model was then simplified [25] by assuming that the stress is only due to the backbone molecule, and thus neglecting the branchpoint withdrawal (i.e. $S_c = 0$). This leads to the stress tensor

$$\underline{\underline{\sigma}}(t) = -p\underline{\underline{E}} + G_N^0 \phi_b^2 \lambda^2(t) \underline{\underline{S}}_{dyn}(t) \quad (2.113)$$

with the plateau modulus G_N^0 and the fraction ϕ_b of the molecular weight of the backbone,

$$\phi_b = \frac{s_b}{s_b + 2qs_a} \quad (2.114)$$

ϕ_b is defined by the relative molecular weights of the arm s_a and of the backbone s_b . Hence, the state of the pom-pom is defined by two dynamical parameters ($\underline{\underline{S}}_{dyn}(t)$ and λ) and five structure parameters (τ_b , τ_s , q , s_a and s_b).

With a differential approximation and a multimode pom-pom model, Inkson et al. (1999) [25] could describe the rheological behaviour in shear and planar extension of commercial low density polyethylene melts by fitting the non-linear parameters to uniaxial extension data. For each relaxation mode, two non-linear parameters, i.e. the stretching time τ_S and the number of arms q , were fitted to uniaxial elongation data. Rubio and Wagner (2000) [65] found that though the set of constitutive equations in the differential approximation may describe both extensional flows and shear flow, the second normal stress difference in planar flow is not described. Furthermore, the full (integral) model overestimates the shear viscosity and first normal stress difference. Also the time-strain separability for stress relaxation after a step-strain is not ensured due to the time dependence of the stretch. Verbeeten et al. (2000) [74] tried to overcome the problem of vanishing N_2 predictions by incorporating a Giesekus-type constitutive equation for orientation. Whilst a fit of the non-linear parameters to the uniaxial viscosity describes the equibiaxial, the first planar and shear viscosity, an extra parameter is necessary to predict the second planar viscosity. With this extended pom-pom model the predictions of a wide range of rheological data is possible, but again a large number of non-linear parameters is necessary.

Chain stretching was also introduced by Pearson et al. (1991) [58] and Mead et al. (1995) [43], [44] assuming that segmental stretch is non-uniform along the contour

length of the tube. In this model, the so-called DEMG model, the independent alignment assumption is also dropped. The tension in the polymer chain is considered to depend on the position along the chain. Segmental orientation and stretch are completely independent processes. But as shown in [42], the DEMG model has many failings in describing non-linear rheological behaviour.

Marrucci et al. (1996) [38], [24] introduced a "convective constraint release (CCR)" process which is based on the fact that the lateral constraints are lost due to the retraction of surrounding chains in their tubes. Hence, two relaxation mechanisms occur in parallel, the diffusion due to thermal motion and the CCR process. This idea was used by Mead et al. (1998) [42] to develop a new model for the tube stretch based on Eq. (2.110), by subtracting a second term from the right-hand side which corresponds to the relaxation of stretch due to CCR. With this new stretch evolution equation, though better predictions of shear stress and first normal stress differences are obtained, no strain-hardening in extensional flows is found for strain-rates $\dot{\epsilon}_0$ smaller than the inverse Rouse relaxation time $1/\tau_R$.

Strain-dependent stretch equations

In models based on Eq. (2.110) or variations thereof, chain stretch is deformation rate dependent. The tube diameter is assumed to remain constant, i.e. $a = a_0$. However, tube stretch can alternatively be introduced by strain-dependent processes by assuming a deformation of the tube diameter.

Marrucci and de Cindio (1980) [39] introduced segmental stretch by considering an affine deformation of the tube with the macroscopic strain. In contrast to the constant tube diameter assumption in the original DE theory, here the volume of the tube segment is assumed to be constant during deformation, i.e.

$$a^2 r = a_0^2 r_0 \quad (2.115)$$

This leads to a decreasing tube diameter a with

$$a = a_0 / \sqrt{r/r_0} \quad (2.116)$$

Using Eq. (2.116), the slip-link function $S(r)$ can be derived from Eq. (2.101),

$$S(r) = \frac{n(r)}{n_0} = \frac{a r}{a_0 r_0} = \sqrt{\frac{r}{r_0}} = \sqrt{u'} \quad (2.117)$$

With the relationship between the disentanglement function $D(r)$ and $S(r)$ (Eq. (2.91)), the non-linear strain measure $\underline{\underline{S}}_t$ (Eq. (2.96)) is then given by

$$\underline{\underline{S}}_t = \frac{10}{3 \langle \sqrt{u'} \rangle_0} \left\langle \frac{u' u'}{\sqrt{u'}} \right\rangle_0 \quad (2.118)$$

If additionally the independent alignment (IA) assumption is introduced, the non-linear strain measure of Eq. (2.118) simplifies to

$$\underline{\underline{S}}_t^{IA} = \frac{15}{4} \left\langle \frac{u'u'}{u'} \right\rangle_0 \quad (2.119)$$

The strain measures of Eqs. (2.118) and (2.119) lead to significant strain-hardening at start-up of extensional flows, but no steady-state viscosity in extensional flow is predicted.

Another model with strain-dependent tube diameter was introduced by Wagner and Schaeffer (1992) [85] and is called "Molecular Stress Function (MSF)" theory. The MSF theory will be presented in more detail in the next chapter since it is the starting point of further developments in describing the rheological behaviour of polymer melts in shear and extension.

2.4.3 Molecular stress function (MSF) theory

In the molecular stress function (MSF) theory [85], [86], [66] the tube diameter a , the line density of monomer units n/l , and the force in the polymer chain \underline{K} are assumed to vary according to segmental orientation. In contrast to the Doi-Edwards (DE) theory, a and n/l are no longer considered to remain constant during deformation: rather the tube diameter a is assumed to be a function of the average stretch of the tube [85]

$$a = a(\langle r/r_0 \rangle) = a(\langle u' \rangle_0) \quad (2.120)$$

As in the DE theory, the tension in the polymer chain is assumed to be the same along the chain for a step-strain deformation, but with increasing deformation the tension \underline{K} rises above the equilibrium tension \underline{K}_{eq}

$$|\underline{K}| = |\underline{K}_{eq}| \frac{a_0}{a(\langle u' \rangle_0)} = |\underline{K}_{eq}| f(\langle u' \rangle_0) \quad (2.121)$$

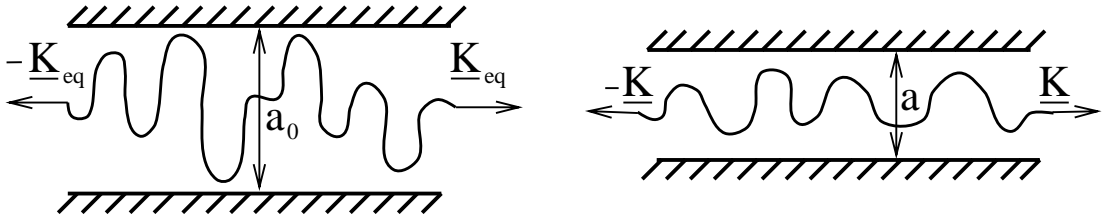


Figure 2.11: Molecular stress function theory [20].

The molecular stress function f is defined by

$$f(\langle u' \rangle_0) = \frac{|\underline{K}|}{|\underline{K}_{eq}|} = \frac{a_0}{a(\langle u' \rangle_0)} \quad (2.122)$$

with the diameter a_0 of the undeformed tube. Hence, the molecular stress function f is the inverse of the relative tube diameter a/a_0 and is assumed to depend on the average stretch of the tube, $\langle u' \rangle_0$. The tension in the polymer chain increases, while the tube diameter decreases with increasing deformation (fig. 2.11).

The non-linear strain measure $\underline{\underline{S}}_{MSF}$ is then given by

$$\underline{\underline{S}}_{MSF} = 5f^2 \left\langle \frac{u'u'}{u'^2} \right\rangle_0 = f^2 \underline{\underline{S}}_{DE}^{IA} \quad (2.123)$$

which consists of the product of the square of the molecular stress function f^2 , and the orientation tensor $\underline{\underline{S}}_{DE}^{IA}$ of the Doi-Edwards theory (Eq. (2.106)). Hence, the constitutive equation of the MSF theory is given by

$$\underline{\underline{\sigma}} = -p \underline{\underline{E}} + \int_{-\infty}^t \overset{\circ}{m}(t-t') \underline{\underline{S}}_{MSF}(t') dt' \quad (2.124)$$

Introducing the constant tube volume assumption with V_0 being the volume of the tube at equilibrium and V the volume of the deformed tube, leads to [85]

$$\frac{V}{V_0} = \frac{a^2 L}{a_0^2 L_0} = 1 \quad (2.125)$$

where L_0 and $L = L_0 \langle u' \rangle_0$ are the contour length of the tube in the undeformed and the deformed state. From this constant volume assumption follows immediately

$$f^2 = \frac{a_0^2}{a^2} = \frac{L}{L_0} = \langle u' \rangle_0 \quad (2.126)$$

i.e. f^2 increases linearly with the average stretch $\langle u' \rangle_0$. However, at larger deformations, it is found that the molecular tension in the chain reaches a maximum value of the molecular stress function f_{max} , which corresponds to a minimum tube diameter [86].

As shown in [66], [87], f^2 can be determined from experiments by relating the experimentally measured damping function h_{exp} , to the Doi-Edwards damping function h_{DE} ,

$$f^2 = \frac{h_{exp}}{h_{DE}} \quad (2.127)$$

The damping functions in uniaxial, equibiaxial and planar extension could be described consistently by the strain measure $\underline{\underline{S}}_{MSF}$, using different approximation functions for f^2 with one or two non-linear parameters. However, with the same parameters, the shear stress and the first normal stress difference in shear are overpredicted [66].

3 Experimental methods

3.1 Extensional experiments

In the last three decades, techniques to measure extensional flows of polymer melts were improved continuously in order to achieve uniform extensional deformations, in spite of the fact that polymer melts are already deformed by gravity and surface tension.

Since no adjacent solid surface exists as in shear flow experiments, the polymer melt has to be supported by a medium to compensate for its gravity by either floating or submerging it without interfering with the extension process. The supporting medium is also responsible for a uniform temperature distribution, and in most cases silicon oil was used. The density of the oil must exactly match the density of the sample at test temperature. Using silicon oil, test temperatures are limited to a maximum of 200 °C because of the thermal stability of the oil. Another problem is that as the sample gets longer and thinner with increasing deformation, the more and more difficult it is to check the uniformity of the cross-section. With increasing deformation, the force measured becomes significantly smaller which results in problems of maintaining a constant stress or strain-rate. Depending on the rheometer design, the maximum strain can be limited by the length of the oil bath. All these problems lead to difficulties in instrument design and development.

Developments were made both for uniaxial and for multiaxial extensional rheometers. Uniaxial elongational rheometers are discussed first. Historically, uniaxial elongational flow was realised either by constant strain-rate experiments with constant sample length but decreasing sample volume or by constant stress experiments with stretching of the sample and conservation of the sample volume [11].

The first important work on constant stress experiments was done by Cogswell (1968) [8] who developed a constant stress melt tensile rheometer. A cylindrical sample is held horizontally between two water-cooled clamps in an oil bath. One of the clamps is fixed and the other one is mounted on a wheeled trolley. At this trolley a chain is fastened, which after passing under a pulley quits the oil bath and is fixed outside the bath to a larger pulley. On the same axis as the pulley, a specially-shaped cam is mounted that provides a constant stress by transforming the gravity of a weight.

More extensive work on a constant stress tensile rheometer was carried out by Vinogradov et al. (1972) [75] using a horizontal set-up as well. In contrast to the rheometer of Cogswell, the sample is fixed between two floating clamps, one of which is movable, the other one is fixed. The force transmission takes place similarly as with the Cogswell rheometer. The hydrodynamic drag is reduced. A photoelectric follower allows the automatic recording of the speed of the movable clamp and thereby of the strain-rate.

With increasing deformation, the force gets very small, and friction finally becomes relevant.

With the intend to reduce the friction of the instrument, Münstedt (1975) [52] developed a rheometer to realise tensile creep tests. The horizontal set-up of the devices of Cogswell and Vinogradov was replaced by a vertical set-up, which eliminates one pulley. The sample is thus suspended vertically in an oil bath, and loaded by a cam which reduces the lever of the load with increasing deformation. The shape of the cam is dependent on the initial sample length. The device allows to measure the force needed for elongation of the sample by a force transducer and records it as a function of time. Samples were prepared by extruding a polymer melt through a capillary die resulting in cylindrically-shaped samples with a diameter from 3 up to 10 mm and a length of 10 up to 50 mm. Samples are glued on small metal clamps. Depending on the initial length, the maximum Hencky strain is limited to $\varepsilon_H = 2.3$. Later, Münstedt (1979)

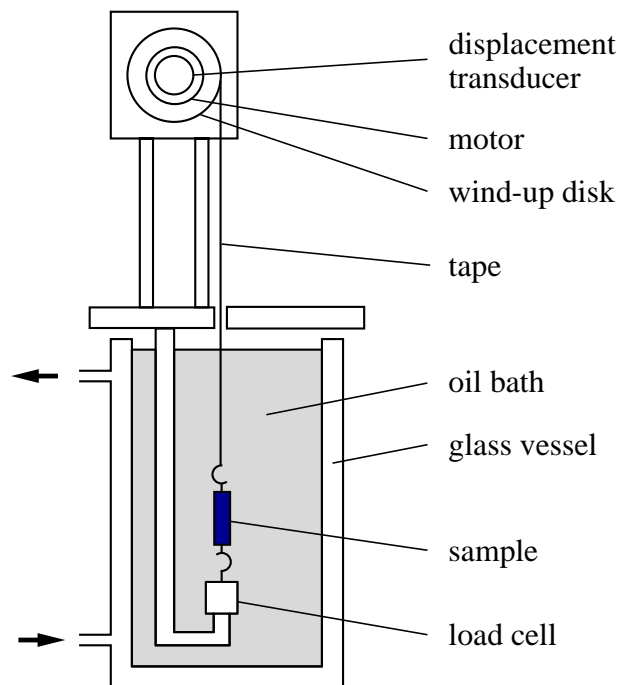


Figure 3.1: Münstedt type tensile rheometer (MTR) [53].

[53] improved his design in order to realise different experimental modes, e.g. constant stress, constant strain-rate, and stress-relaxation experiments. Here, the sample is fixed to a load cell located at the bottom of the oil bath which is situated in a jacketed glass vessel through which a temperature medium flows for heating the oil bath (fig. 3.1). The upper end of the sample is fixed to a thin metal tape which can be rolled up by a disk mounted to the shaft of a DC servomotor. The sample position is indicated by a displacement transducer, which allows a direct measurement of the elongation. It was possible to increase the maximum Hencky strain to $\varepsilon_H = 3.9$. This rheometer

design was commercialised independently by Rheometrics and Göttfert [11]. Lately, the rheometer has been completely redesigned [29] as far as the measuring technique and control engineering are concerned by using new technologies, with a measuring range for temperatures between 25 and 220 °C, strain-rates between 0.001 and 2 1/s, and a maximum Hencky strain of $\varepsilon_H = 3.9$.

The main problem of elongational rheometers with moving clamps is the limitation of the maximum achievable strain due to the finite length of the oil bath. This problem can be resolved by constant strain-rate experiments involving a constant sample length.

Meissner (1969) [45], [47] developed the rotary clamp technique which consists of two pairs of wheels with small gear teeth gripping the sample and providing a uniform stretching by rotating the clamps in opposite directions. The tensile force is determined by mounting one pair of the clamps together with the motor on a leaf spring, the displacement of which is proportional to the force and measured by a linear voltage differential transformer. The sample is not glued on clamps but is gripped between the clamps separated by a fixed distance and driven by synchronous motors. A constant rotational speed of the clamps allows to deform the sample with a constant strain-rate. The material is transported continuously from within the measuring distance to the outside, floating on heated silicon oil at the required temperature. The maximum strain obtainable is not limited by the length of the oil bath. Assuming homogeneous deformations, strains up to a stretch ratio of $\lambda = 400$, corresponding to a Hencky strain of $\varepsilon_H = 6$, could be reached by Laun and Münstedt (1976) [34] by improving the temperature homogeneity and the force measuring device in resolution and stability. By further increasing the temperature homogeneity in such a way that the variation at 150 °C is less than 0.1 K, the maximum Hencky strain could be increased up to $\varepsilon_H = 7$ [50]. Samples are produced by extruding polymer rods of an approximate length of 75 cm and a diameter of 6 up to 8 mm. Hence, samples are quite large which makes it difficult to ensure homogeneity of the initial cross-section along the sample. Along the sample, pairs of scissors are located which allow to cut the sample in several parts. In this way, the recoverable strain can be determined, and the uniformity of the stretched sample can be checked.

Later, Meissner (1994) improved the rotary clamp technique as described in detail in [49]. The basic features are a new type of clamp, using two metal conveyor bands instead of the toothed wheels, and the replacement of the oil bath by a heated nitrogen or air flow as supporting and heating medium. The clamps are located in a heated housing. The major advantage is that measurements of uniaxial elongation can now be performed for polymer melts which react chemically with silicon oil or with melt temperatures above the thermal stability of the oil. The maximum Hencky strain is $\varepsilon_H = 7$, which corresponds to a maximum stretch ratio of $\lambda = 1100$, provided the deformation is homogeneous until the end of the test. This design was commercialised by Rheometric Scientific as "Polymer melt elongational rheometer (RME)". It was used in this work to perform uniaxial elongational experiments, and is described in

more detail in the following chapters 3.1.1 to 3.1.4.

Different possibilities exist to realise multiaxial extensions as for example by the bubble inflation technique, the lubricated squeeze flow technique, diverging pressure flow, and the use of the rotary clamp technique, described and summarised in [11], [12], [60]. In the bubble inflation technique, a circular moulded sample of a polymer melt is fixed between two plates in which circular concentric holes are cut. After melting, the sample is inflated by increasing the pressure in the inflation medium on one side which leads to a biaxial extension. For the squeeze flow technique, the polymer melt is placed between two plates and then subjected to compressional deformation [63]. To avoid shear flows due to wall adhesion of the melt, the surfaces of the two plates are usually lubricated.

Meissner (1981) [50] used the rotary clamp technique to construct a biaxial rheometer by arranging eight clamps circularly for equibiaxial extension [50], and rectangularly for planar extension [51]. The rotary clamp technique was amended in such a way that the force components along and normal to the flow direction can be measured separately. The clamps introduce the required velocity at the rim of the sample and measure the resulting force vector acting from the deforming sample on each end. In equibiaxial extension, samples are flat, circular disks, and in planar extension flat sheets. One direction of the sample is much smaller than the other two directions. A table is located inside the arrangement of clamps to support the sample by a layer of talcum resting on the table. Between the clamps, eight pairs of scissors are positioned to cut the extending sample at the rim within defined time intervals. By photographing a grid at certain time intervals, which was printed on the sample before the test, the biaxial deformation is measured and controlled. The maximum obtainable biaxial Hencky strain was $\varepsilon_H = 2$. The speed of rotation is equal for all clamps which leads to a radial extension of the sample for equibiaxial flow. For planar extension, the directions of the strain-rate in the sample and the force acting on the clamps are different. With this biaxial extensional rheometer, investigations of a polyisobutylene in simple, equibiaxial, and planar extensions were performed by Meissner et al. (1982) [51] at room temperature. These rheometers allowed homogeneous deformations and well-defined boundary conditions, but were restricted to tests at room temperature and involved relatively large samples.

Later, Hachmann (1996) [23] could eliminate some of these problems. The clamps are redesigned as described in [49], and located in a heated housing. The sample is supported by a hot gas flow. Uniaxial, equibiaxial, and planar extensions were performed on a high density (HDPE I), and low density (LDPE I) polyethylene, and uniaxial and equibiaxial extensions on a polystyrene (PS) melt. These data are presented in [23], [80] and in this work.

3.1.1 The elongational rheometer RME

The "polymer melt elongational rheometer RME" is an elongational rheometer designed by Meissner et al. (1994) [49], and commercialised by Rheometric Scientific [61]. The experimental set-up used for conducting uniaxial experiments is shown in fig. 3.2. The system consists of the RME housing, an electronic box, a gas supply system, a personal computer, and a video system.

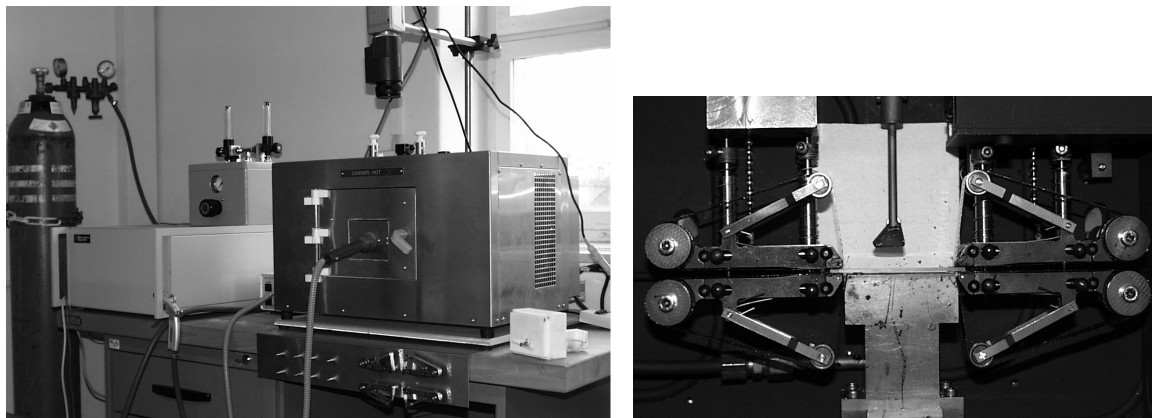


Figure 3.2: Elongational rheometer RME.

The RME housing is formed by six metal plates, blackened to provide a homogeneous temperature field by means of radiation, and heated electrically. The polymer melt is gripped between two clamps, located inside the housing. Each of them consists of two belt holders placed on holder carriers from which they can be removed easily for cleaning. On each belt holder, driven by light-weight motors, metal conveyor belts move in order to transfer the velocity of the belts to the local speed of the sample. The clamps can be opened from outside the housing which avoids temperature fluctuations. The tensile force exerted by the sample on the clamps is measured directly by a displacement transducer linked to the right clamp. The sample is gripped between the clamps and suspended by nitrogen or air flowing through a porous table located between the lower belt holders of both clamps, and providing the required test temperature of the sample (fig. 3.3).

By using nitrogen gas, oxidation of the sample is avoided, and the test temperature can be increased up to $350\text{ }^{\circ}\text{C}$. The sample size was reduced to a rectangular shape of initial length of around 55 mm, initial thickness between 1.4 and 2 mm, and initial widths between 7 and 10 mm. To avoid the sagging of the sample between the table and the metal bands, tongues are welded on the metal bands to bridge the gap between the clamps and the table. A special bending technique of the lower belts is used which raises the sample slightly after releasing the clamps [70]. A pin of a diameter approximately

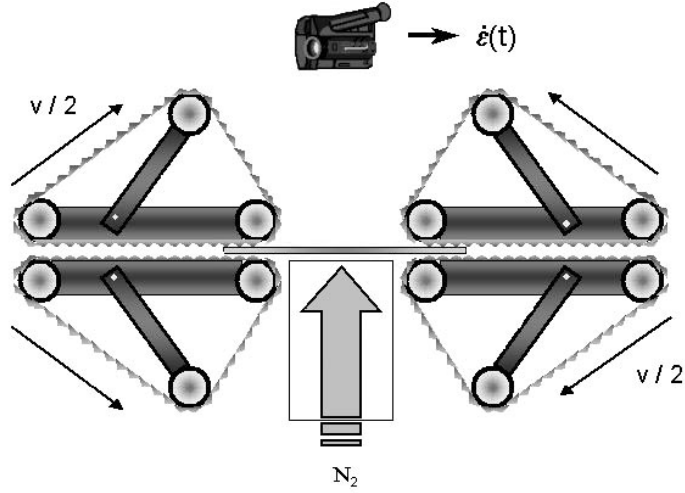


Figure 3.3: Elongational rheometer RME.

0.5 mm larger than the initial sample thickness is placed between each clamp next to both ends of the sample to avoid a squeezing of the sample when releasing the clamps. The sample can very easily be inserted into the rheometer by a specially-designed feeding plug, which helps to prevent temperature fluctuations during the loading of the sample. The strain-rate range is 0.0001-1 1/s, the tensile force range 0.001-2 N with a resolution of 0.001 N, temperature constancy at the sample of $\pm 0.2 K$, and the maximum Hencky strain $\varepsilon_H = 7$ [61]. The maximum Hencky strain is reduced, if metal bands with tongues are used.

With the tensile force $F(t)$ directly measured by the RME, the tensile stress $\sigma_1(t)$ can be determined as

$$\sigma_1(t) = \sigma_{11} - \sigma_{33} = F(t)/A(t) \quad (3.1)$$

with the rectangular cross-section $A(t)$ decreasing with time.

Assuming incompressibility of the polymer melt, the equation of continuity provides for the relation between the initial sample dimension and the one during the experiment,

$$L(t)A(t) = L_0A_0 = L_0W_0H_0 \quad (3.2)$$

with the initial length L_0 , the initial width W_0 , and the initial height H_0 .

For a constant strain-rate $\dot{\varepsilon}_0$, the increase in length $L(t)$ is exponential, i.e. $L(t) = L_0e^{\dot{\varepsilon}_0 t}$. Hence, the decrease of the cross-sectional area $A(t)$ is given by

$$A(t) = A_0e^{-\dot{\varepsilon}_0 t} \quad (3.3)$$

Inserting Eq. (3.3) into the expression for the tensile stress σ_1 (Eq. (3.1)), the elongational or uniaxial viscosity η_u is

$$\eta_u(t) = \frac{\sigma_1(t)}{\dot{\varepsilon}_0} = \frac{F(t)}{\dot{\varepsilon}_0 A_0 e^{-\dot{\varepsilon}_0 t}} = \frac{F(t)e^{\dot{\varepsilon}_0 t}}{\dot{\varepsilon}_0 A_0} \quad (3.4)$$

3.1.2 Experimental results

The tensile force is measured by deflection of the spring system, and is transferred to a personal computer (PC) as digitised voltage. In the PC, it is stored as force $F(t)$ along with the calibration data. A calibration of the force transducer at each required temperature with weights ranging from 1 to 200 g is obligatory. The calibration curve determined for different temperatures is shown in fig. 3.4. The force gain is averaged over all force gains determined from several weights at each temperature. It is necessary to use not only a weight of 200 g, as recommended in the RME manual [61], but also small weights because the force values at high deformations are small.

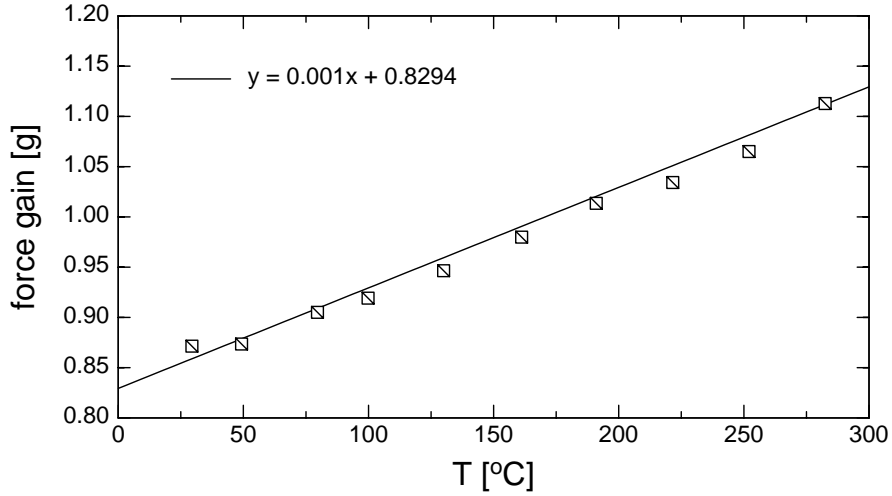


Figure 3.4: Calibration of the force transducer at different temperatures with several weights.

A typical result of the force signal is shown in fig. 3.5 for a low density polyethylene melt LDPE II (fully characterised in the appendix) for a strain-rate of $\dot{\epsilon} = 0.0939$ 1/s, measured at a temperature of $T = 170$ °C. Shortly after the start of the test, the force reaches a maximum and then decreases gradually to zero. Sometimes, a force correction at the end of the test is necessary, and two different cases have to be distinguished [69]: rupture or no rupture of sample at the end of the test. If the sample breaks at the end, a force correction to zero has to be done. If there is no rupture, and the force is still decreasing exponentially to zero, a force correction is critical because the material is still relaxing. On the other hand, if the sample does not break, and the force is constant, the force can be corrected to 0.1-0.2 cN. In fig. 3.5, the resulting tensile stress $\sigma_1(t)$ is also shown which is calculated with the initial cross-section by Eqs. (3.1) and (3.3).

The final result is then the elongational viscosity η_u calculated with the strain-rate $\dot{\epsilon}_0$ by Eq. (3.4). Experimental results for melt LDPE II are shown in fig. 3.6 at $T = 170$ °C for various strain-rates.

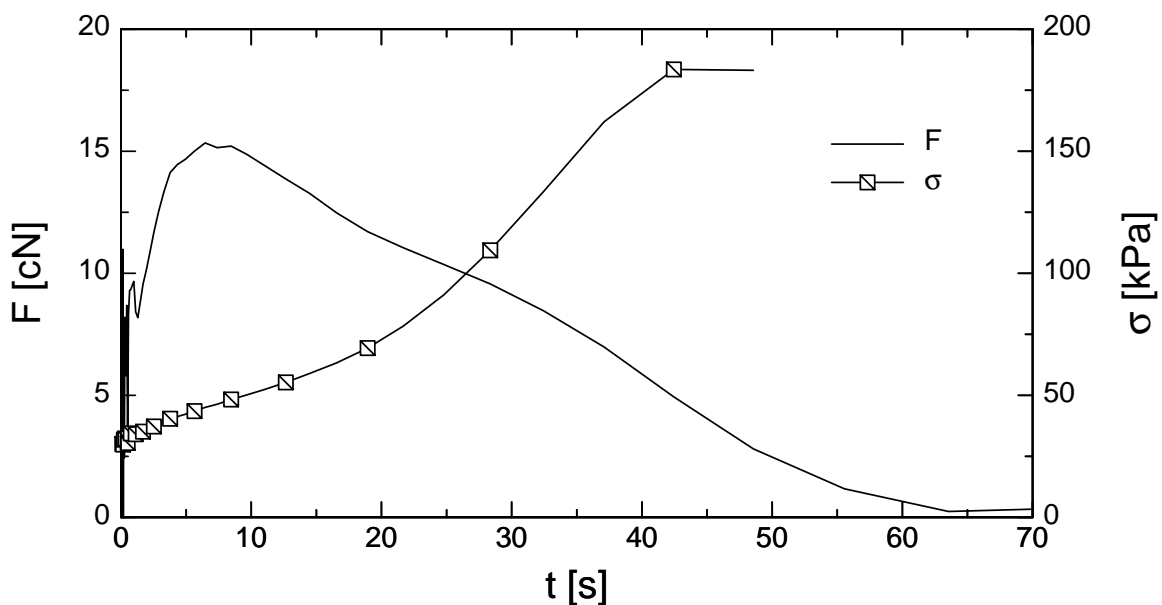


Figure 3.5: Tensile force and stress in elongation of LDPE II melt at a temperature of $T = 170\text{ }^{\circ}\text{C}$ and a strain-rate of $\dot{\epsilon} = 0.0939\text{ }1/s$.

In fig. 3.6, the elongational viscosity measured with the RME is compared to the three-fold zero-shear viscosity $3\eta_0(t)$, calculated from the relaxation spectrum. At the onset of stress growth, both material functions coincide, but after a certain deformation the elongational viscosity rises above the linear-viscoelastic curve. This phenomenon is called "strain-hardening" [32]. As typical for long-chain-branched polyolefin melts, melt LDPE II shows enhanced strain-hardening compared to linear polyolefin melts. Also in fig. 3.6, the RME results of the elongational viscosity are compared to results of a Münstedt type tensile rheometer (MTR), performed at BASF AG, Ludwigshafen/Rhein. The agreement of both measurements of elongational viscosities is excellent for all strain-rates. The comparison shows the pro and cons of both elongational rheometers. While the RME, apart from better sample handling, allows to investigate larger deformations so that for lower strain-rates even a steady-state value is reachable (fig. 3.6), the MTR convinces at the onset of the test. MTR data show better coincidence with the threefold zero-shear viscosity $3\eta_0(t)$, and also after rising above $3\eta_0(t)$, the shape of the curve is more trustworthy. Inaccuracies of the elongational viscosity determined by the RME can be due to problems arising from the force transducer at low force levels which can occur either at the start of test or at the end.

The importance of controlling the force signal of the RME is shown in fig. 3.7, in which the uniaxial viscosity is presented for a POP melt (a Polyolefin Plastomer, characterised in appendix), measured at various strain-rates and at a temperature of $130\text{ }^{\circ}\text{C}$. The amount of strain-hardening observed is very different for the lowest strain-rate of $\dot{\epsilon}_0 = 0.01\text{ }1/s$ depending on the initial cross-section of the sample. The sample

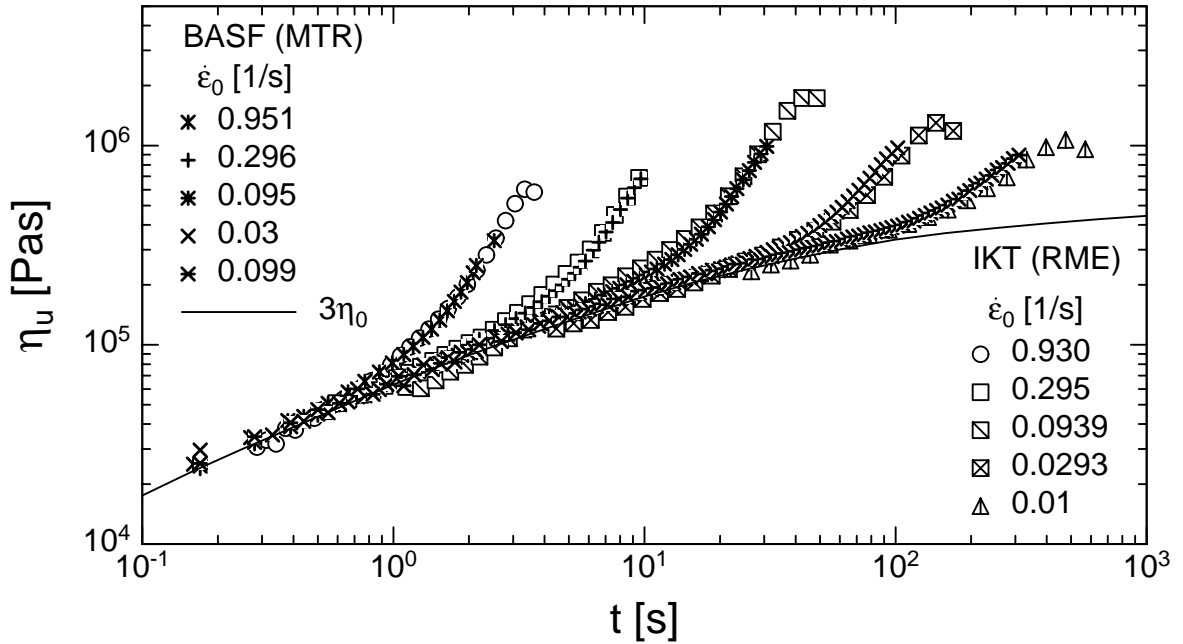


Figure 3.6: Elongational viscosity η_u of melt LDPE II at a temperature of $T = 170 \text{ }^\circ\text{C}$ and for various strain-rates.

with the smaller initial cross-section ($A=10.7 \text{ mm}^2$) produces an enhanced strain-hardening compared to samples with the same initial cross-section at higher strain-rates. This was also found within a round-robin experiment directed by Schulze (1999) [67], in which measurements of elongational viscosity from various commercial RME rheometers were compared to each other and to the ones obtained by the original RME of Meissner in Zürich, and the Münstedt type tensile rheometer (MTR) in Erlangen. While all commercial RME rheometers did find this enhanced strain-hardening at low strain-rates, the original RME and the MTR did not. If the test for $\dot{\epsilon}_0 = 0.01 \text{ 1/s}$ is repeated with a sample of larger cross-section ($A=19.3 \text{ mm}^2$), the strong strain-hardening observed by a test with smaller initial cross-section cannot be reproduced. Regarding the force signal of both tests (fig. 3.8), it is obvious that the force signal of the sample with smaller initial cross-section reaches already at an early time a constant force level which is very close to zero. However, this negligible force signal produces an enhanced strain-hardening because the force is divided by a cross-section of the sample which decreases exponentially. For the sample with larger initial cross-section, the force reaches a higher maximum and decreases until the end of the test. Hence, the cross-section of the sample is large enough to provide a sufficient force signal until the end of test. Tests with both sample dimensions were reproduced and it was verified that at least for this POP melt, the enhanced strain-hardening is an artefact. The maximum of the initial width of the sample is limited to $W_0 = 10 \text{ mm}$ due to the size of the conveyor belts in the RME. This limitation can reduce the lower limit of measurable strain-rates especially for linear or low-viscosity melts.

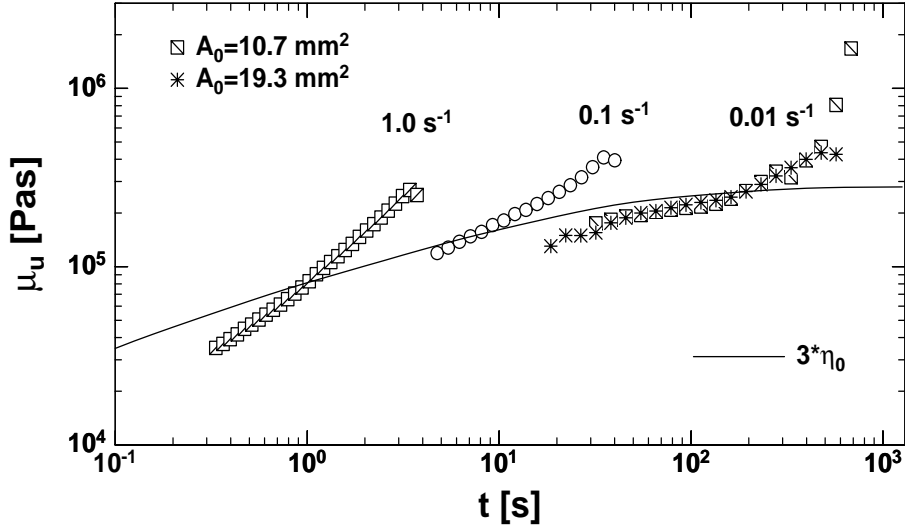


Figure 3.7: Uniaxial viscosity of melt POP.

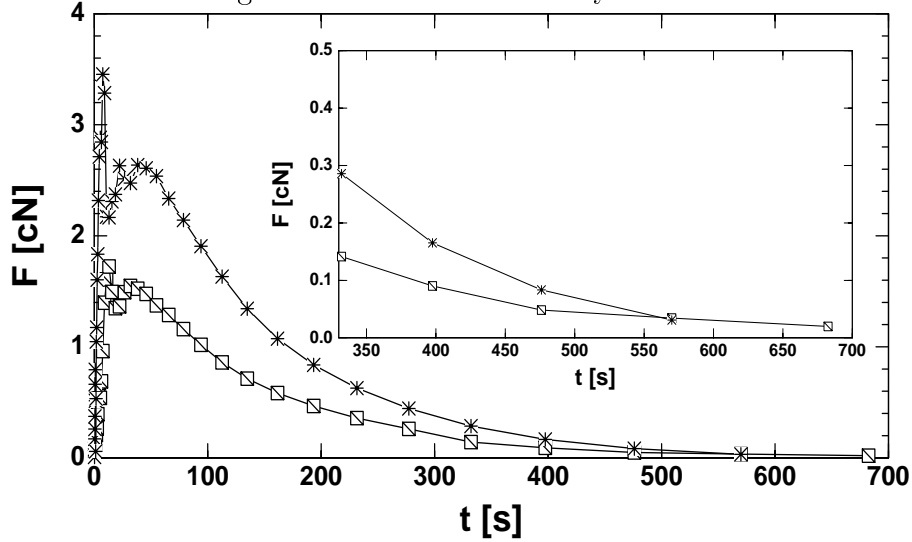


Figure 3.8: Force at low strain-rates.

Another possibility to obtain reliable RME data at low strain-rates is not only to increase the initial cross-section, but also to measure at lower test temperatures. A LLDPE melt (a linear low density polyethylene, characterised in appendix), investigated by Münstedt et al. (1998) [54] at a temperature of 150 °C, was found to show a pronounced strain-hardening only at low strain-rates. For this material, the strain-hardening increases with decreasing strain-rate in contrast to the behaviour of long-chain-branched polyolefin melts for which strain-hardening becomes less pronounced with decreasing strain-rate. This effect was found both at Erlangen with the Münstedt type tensile rheometer (MTR) and at Zürich with the original RME. But measurements performed with our RME at a temperature of 150 °C clearly showed that the force signals for melt LLDPE are rather spurious due to its low viscosity. Decreasing the test temperature down to 130 °C (still above the melting temperature) produces enough force for tests even at a strain-rate of $\dot{\epsilon}_0 = 0.018$ 1/s (fig. 3.9). In

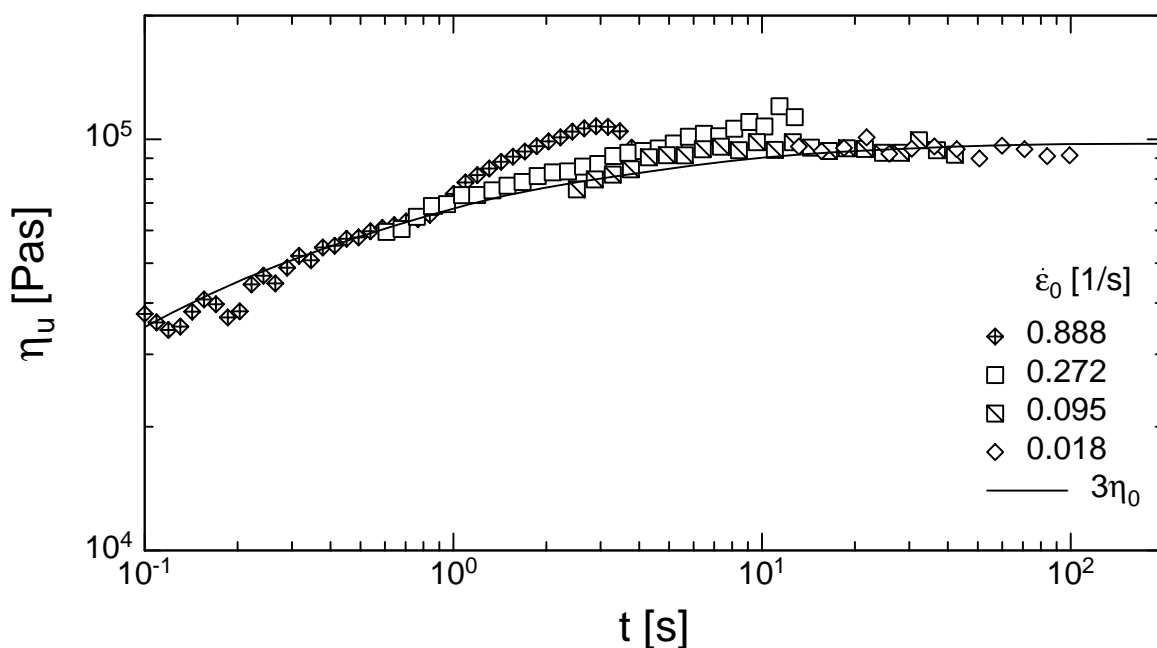


Figure 3.9: Elongational viscosity of melt LLDPE at 130 °C.

[54] a pronounced strain-hardening was already found for $\dot{\epsilon}_0 = 0.1$ 1/s and at 150 °C. Our results for melt LLDPE are within expectations for a linear polymer melt and approach to the threefold zero-shear viscosity $3\eta_0(t)$ at small strain-rates.

To summarise, RME measurements produce reliable results of the elongational viscosity of polymer melts up to Hencky strains of more than $\epsilon = 6$, if the tensile force does not decrease to values below the resolution of the force transducer.

3.1.3 Evaluation of the true strain-rate

Another problem of the elongational rheometer RME is the deviation of the true strain-rate from the set strain-rate. The set strain-rate is calculated using the effective initial length L_0 of the sample and the rotational speed v of the clamps.

$$\dot{\epsilon}_0 = \frac{2v}{L_0} \quad (3.5)$$

The effective sample length is determined by adding two millimetres to the distance between the bearing pins of the small rollers at the front of the belt holders [68]. This value may vary for each RME, the value for our RME is $L_0 = 52.7$ mm. Use of an incorrect value of the effective length can be a reason for a deviation between the set strain-rate and the true strain-rate.

In fig. 3.10, the decrease of the sample cross-section $A(t)$ with time is shown for different values of effective sample length, and in fig. 3.11 the resulting influence on the viscosity is shown. If a value smaller than the true effective length is chosen for L_0 , the uniaxial viscosity shows higher values due to an increased strain-rate $\dot{\epsilon}_0$ according to Eq. (3.5).

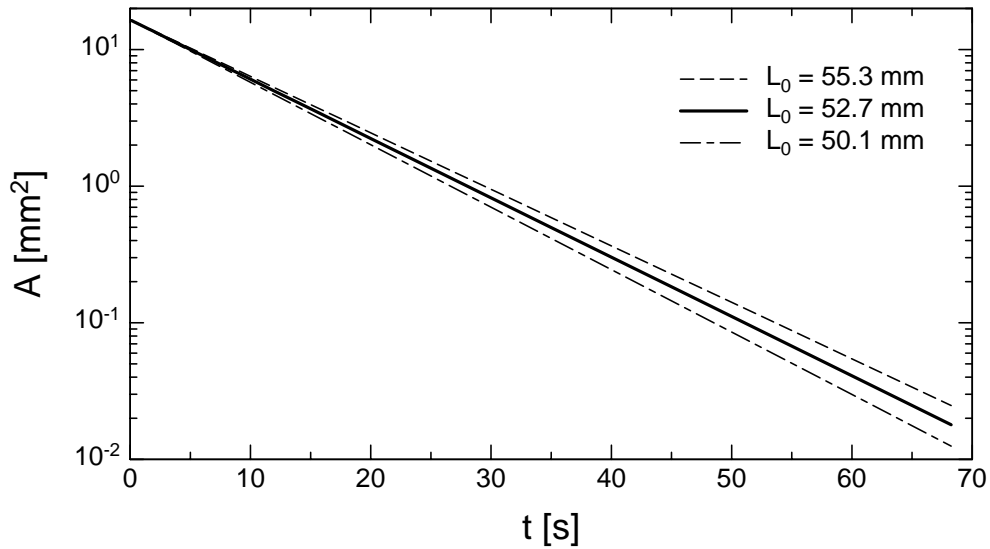


Figure 3.10: Decrease of $A(t)$ with time for different values of effective sample length L_0

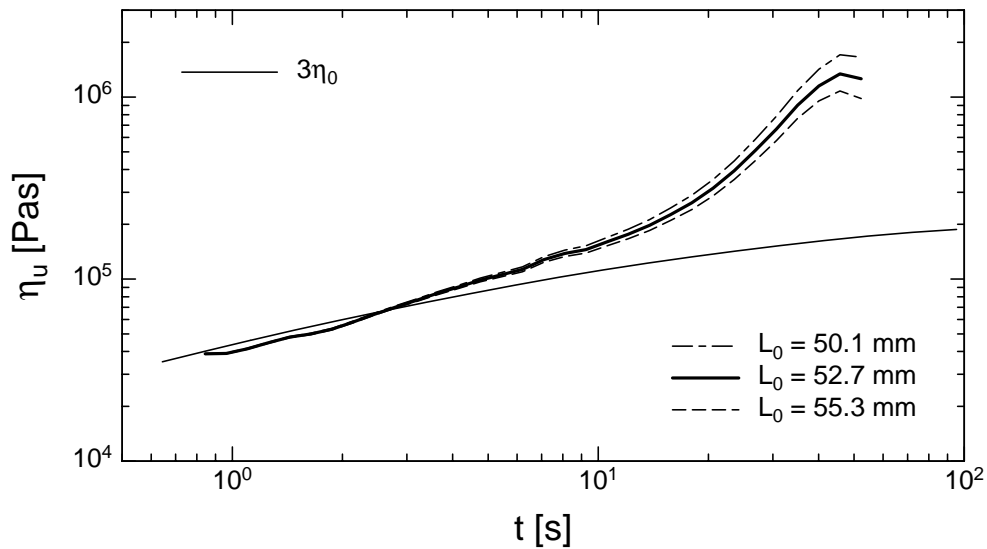


Figure 3.11: Effect of different initial sample lengths on uniaxial viscosity

Other reasons for deviations might be slip of the sample within the clamps, inhomogeneous samples, and a non-uniform cross-sectional area along the sample [70].

In principal, two possibilities exist to check the true strain-rate. One possibility is to measure the decrease of sample width during the experiment [63], [88]. A plot of the natural logarithm of the average sample width over time is then fit to a straight line, whose slope multiplied by -2 gives the true strain-rate. However, this method is not very accurate and can lead to errors, e.g. non-constant strain-rates were found by Waßner (1999) [88].

The other possibility is to evaluate the true strain-rate by the “Particle Tracking Method” [62]. To apply this method, a personal computer equipped with the appropriate software, an illumination system consisting of a light source and a glass fibre cable, a video camera, recorder, and screen, and a timer to report the time to the recorder, are necessary. For marking the polymer sample with tracers after melting, small glass beads of 160 - 180 μm are placed on the sample by use of a metal tube which is inserted into the rheometer, and which allows also to apply glass beads on the sample during the experiment. The glass beads should show a distinctive contrast with the polymer melt and should be distributed on the sample uniformly.

The procedure of evaluation starts with image acquisition, followed by image processing, the particle tracking menu and the calculation of the strain-rate and elongation [62]. By image acquisition, a series of images taken at equidistant times will be digitised. Digitisation is necessary to convert an image into numerical form which can then be processed by the computer [7].

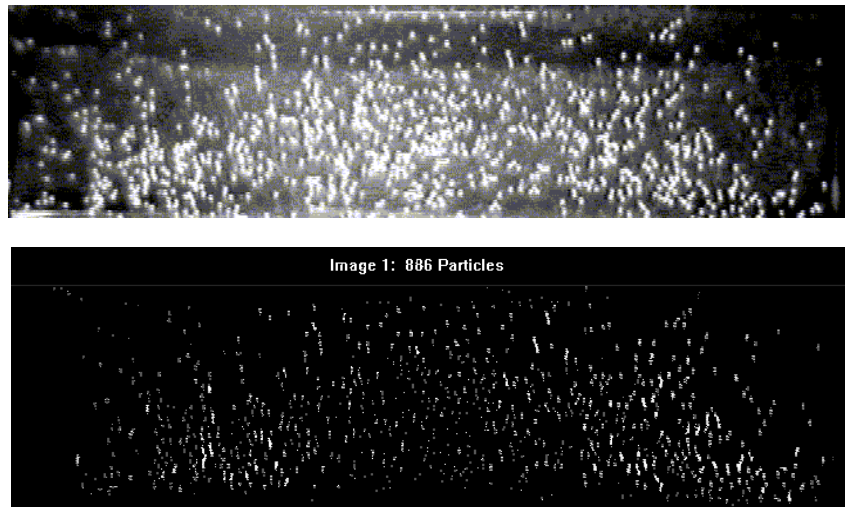


Figure 3.12: Digitised pictures and recognised particles

By image processing, the particle positions on each image will be enhanced by separating the particles from the background as shown in fig. 3.12. Particle brightness and size can be changed by displaying the digitised images.

By particle tracking, individual particles are followed through a predefined number of images by selecting a particle in image one and then searching this particle in image two

in a supposed area defined by a maximum value in x-direction (Dx) and in y-direction (Dy). For all particles found in this area of image two, particles will be searched in the supposed area of the following image. If it is possible to follow a particle through the defined number of images, the results are tracks as shown in fig. 3.13.



Figure 3.13: Tracks.

In the last menu the average strain-rate $\dot{\epsilon}_0$ is calculated from the tracks of pairs of particles by the following equation:

$$\dot{\epsilon}_0 = \frac{\ln(\Delta x_2 / \Delta x_1)}{t_2 - t_1} \quad (3.6)$$

Fig. 3.14 shows the different possibilities of combining particle P_1 with particles situated in the grey area. A limiting factor is the maximum particle angle α and the minimum and maximum particle distance.

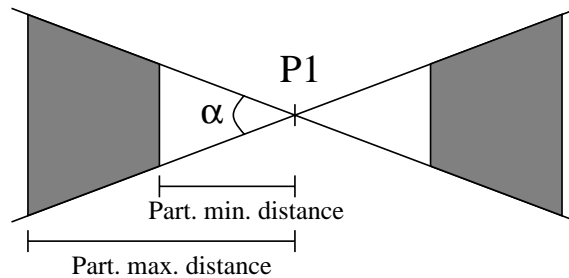


Figure 3.14: Selection of a pair of particles [62].

the tracks at time t_1 and t_2 as shown in fig. 3.15.

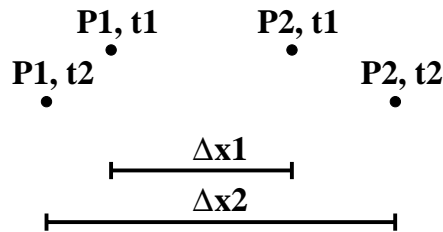


Figure 3.15: Calculation of strain-rate $\dot{\epsilon}_0$ [62].

The programme calculates a maximum and a minimum value of the strain-rate and its standard deviation, and a Hencky strain increment by $\ln(\Delta x_2 / \Delta x_1)$.

The sample can be divided in up to five commensurate zones in which strain-rate and elongation is calculated separately. This allows to check the homogeneity of the sample during the test, and even inhomogeneous deformations invisible to the eye can be detected, as e.g. shown for melt LDPE II (characterised in appendix) in fig. 3.16. Here, the sample was divided into three zones. The strain-rate is constant until nearly the rupture of the sample. At the end of the test, there is an increase of the strain-rate in zone 3 and a decrease in zone 1 and 2 of the sample, i.e. the sample gets thinner and breaks in zone 3.

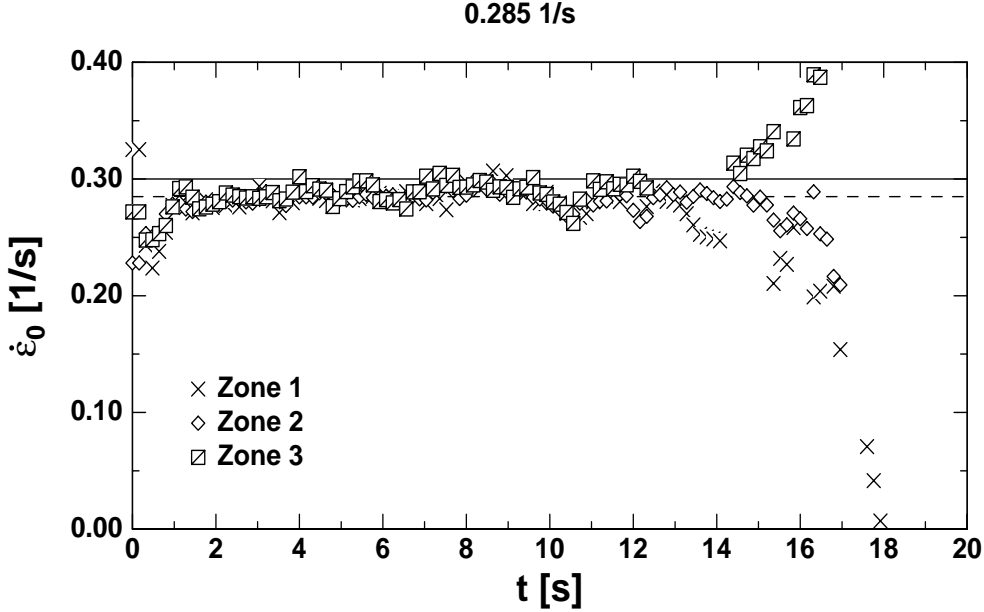


Figure 3.16: Strain-rate $\dot{\epsilon}_0$ for melt LDPE II measured by particle tracking in three zones. Dotted line corresponds to (average) strain-rate of $\dot{\epsilon}_0 = 0.285 \text{ 1/s}$.

With this method, constant strain-rates can be found up to Hencky strains of five. Deviations of the true strain-rate from the set strain-rate found for our RME are not as high as reported by others [88], and lie usually between 5 and 12 %.

3.1.4 Sample preparation

A careful sample preparation is necessary to provide homogeneous and completely relaxed samples of the correct size. Mostly, samples were prepared by direct compression moulding of pellets by means of appropriate metal moulds either into a plate of $1.5 \times 70 \times 100 \text{ mm}^3$ or directly into the desired sample dimensions. The plate can be cut into ten regular samples with a circular saw specially built for the sample preparation of RME measurements. Since the thickness of the plate at the rim is uneven, it is removed by the saw which is an advantage over direct moulding of samples into metal shapes of sample size. However, by using the circular saw the sample width is not

variable which might be necessary to provide enough force signal by larger initial sample dimensions as shown before. The metal moulds are filled with pellets and placed between two metal plates separated by thin sheets of either aluminium or pure PTFE. The pressing tool is placed into a hot laboratory press at moulding temperature for at least 10 min to preheat the polymer. Then the pressure is loaded in steps in order to obtain a relaxed polymer sample. If the required moulding pressure is reached, the polymer melt is pressed for a sufficient time depending on the longest relaxation time [23]. Subsequently, the whole pressing tool is removed from the press and cooled down to at least the heat distortion temperature of the polymer under pressure before the polymer plate is removed from the metal mould. Precise information about pressing temperature and pressure is given in chapter 4.

For linear melts, extrusion before compression moulding is recommended to homogenise the melt [23], [49]. The polymer melt is extruded by an appropriate extruder, and the extrudate is put immediately into the metal mould and the same pressing protocol is used as described above.

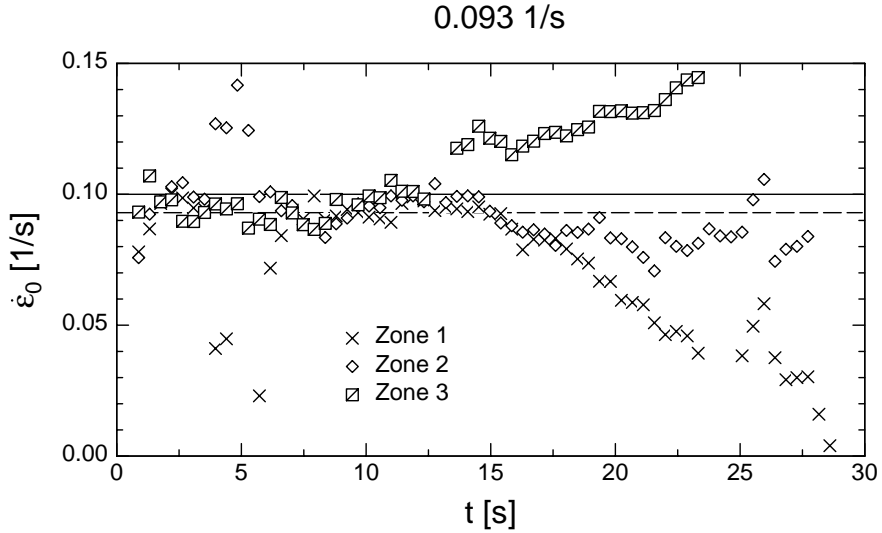


Figure 3.17: Non-homogeneous deformation of melt HDPE III.

The advantage of extrusion over direct compression moulding of pellets is shown for a linear polyethylene melt (HDPE III, characterised in appendix) in figs. 3.17 and 3.18. Particle tracking results are presented for a strain-rate of $\dot{\epsilon}_0 = 0.093$ 1/s; the sample was divided into three commensurate zones. For a sample made from direct moulding of pellets, the deformation is only homogeneous in the first half of test. Then the strain-rate in zone 3 increases while the ones in zone 1 and 2 decrease. If the melt is extruded before compression moulding, the deformation remains constant until rupture of the sample which also occurs at larger deformations. In addition, the scatter of the strain-rate is less for all zones.

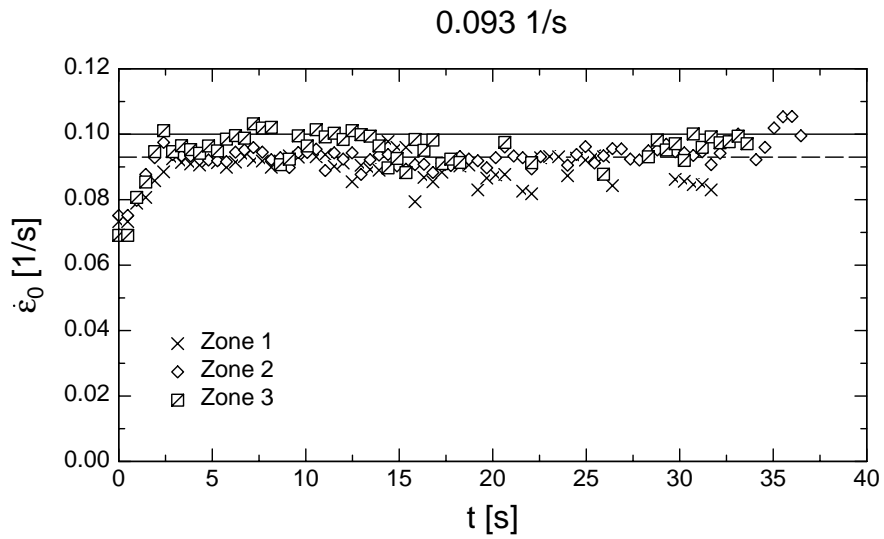


Figure 3.18: Homogeneous deformation of melt HDPE III.

3.2 Shear experiments

Measurements of shear properties can be performed by two types of instruments, namely capillary rheometers, in which the flow is produced by a pressure gradient, and drag flow rheometers, in which one adjacent wall moves relative to a second, stationary one [12]. The polymer melt is thus placed between two fixed solid surfaces which spares the supporting liquid being necessary for the performance of extensional flows. Drag flow rheometers use the principle of either rectilinear or rotational motion of a solid surface.

Fig. 3.19 shows the set-up of a rotational rheometer in the cone-and-plate geometry which is the preferred geometry to measure viscoelastic properties of polymer melts. A polymer sample, produced by compression moulding, is fixed between a plate and

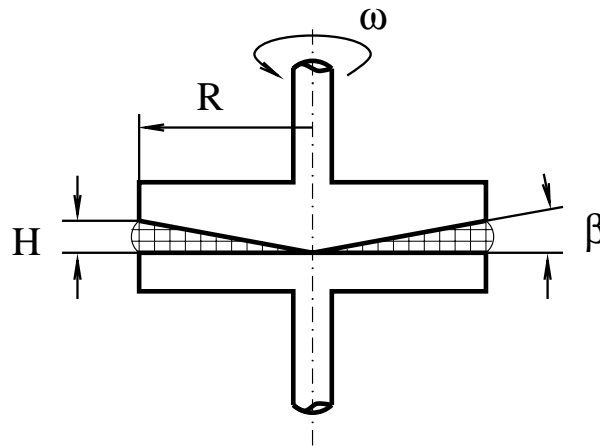


Figure 3.19: Cone-and-plate geometry.

a cone with a radius R and a cone angle β ($\beta < 5^\circ$), one of which is rotating at a

constant angular velocity ω , the other one is fixed. The symmetry axes of cone and plate coincide, and a spherical coordinate system is used. With this geometry, the shear flow is nearly homogeneous when the cone angle is very small, i.e. $\tan\beta \approx \beta$. Hence, shear-rate and shear stress are homogeneous. This allows a direct determination of material functions without differentiating the data. At the stationary part of the system, the torque M and the normal force F_N , introduced by the sample, are measured. With these physical quantities, determined experimentally, and by specifying the flow field, the equations of motion can be solved. This allows the determination of rheological properties like shear and normal stress, shear deformation, and shear-rate and thereby the rheological material functions viscosity, normal stress differences, and shear relaxation modulus, assuming incompressibility.

Another set-up for rotational rheometers is the plate-and-plate geometry in which the sample is located between two coaxial, parallel plates with a radius R , separated by a gap H , one of which is rotating with a constant angular velocity ω , the other one is fixed. Since the shear-rate is not uniform in the gap, direct data acquisition is not possible and data differentiation is necessary. Most frequently, the plate-and-plate geometry is used to determine the linear-viscoelastic properties (chapt. 2.2) by oscillatory measurements in which the storage (G') and loss (G'') moduli are calculated as

$$G' = \frac{2MH}{\pi R^4 \omega} \cos\delta \quad (3.7)$$

$$G'' = \frac{2MH}{\pi R^4 \omega} \sin\delta \quad (3.8)$$

with the measured quantities torque M and its phase lag δ . Mainly, the strain-controlled rheometer DSR of Rheometric Scientific was used in this work for the linear characterisation of the polymer melts investigated.

Start-up flow experiments

In start-up flow experiments, a material is sheared with a constant shear-rate $\dot{\gamma}(t)$ starting at $t = 0$,

$$\dot{\gamma} = \begin{cases} 0 & t \leq 0 \\ \dot{\gamma} = \text{const.} & t > 0 \end{cases} \quad (3.9)$$

The equations for shear-rate $\dot{\gamma}$, shear stress σ_{12} , and first normal stress difference N_1 can be evaluated for the cone-and-plate geometry,

$$\dot{\gamma} = \frac{v(r)}{H(r)} = \frac{r\omega}{r \tan\beta} \approx \frac{\omega}{\beta} \quad (3.10)$$

$$\sigma_{12}(t) = \frac{3M(t)}{2\pi R^3} \quad (3.11)$$

$$N_1 = \sigma_{11}(t) - \sigma_{22}(t) = \frac{2F_N(t)}{\pi R^2} \quad (3.12)$$

with velocity $v(r)$, gap $H(r)$ at a radius r ($r \leq R$), and constant angular velocity ω of the driven part. Using these rheological properties, the viscometric material functions, the shear viscosity η , and the first normal stress coefficient Ψ_1 , can be determined,

$$\eta(t, \dot{\gamma}) = \frac{\sigma_{12}(t)}{\dot{\gamma}} = \frac{3\beta M(t)}{2\pi R^3 \omega} \quad (3.13)$$

$$\Psi_1(t, \dot{\gamma}) = \frac{N_1}{\dot{\gamma}^2} = \frac{2\beta^2 F_N(t)}{\pi \omega^2 R^2} \quad (3.14)$$

In this work, measurements of $\eta(t, \dot{\gamma})$ and $\Psi_1(t, \dot{\gamma})$ were performed using the cone-and-plate geometry in a strain-controlled rheometer RMS800 of Rheometric Scientific.

Step-strain experiments

In a stress relaxation experiment, the sample is deformed by a step deformation γ ,

$$\gamma = \begin{cases} 0 & t \leq 0 \\ \gamma = \text{const.} & t > 0 \end{cases} \quad (3.15)$$

in such a way that the driven part of the system is displaced instantaneously by an angle ϑ , and both the normal force $F_N(t)$ and the torque $M(t)$ are observed. From these measurements, the shear stress (Eq. (3.11)) and the first normal stress difference (Eq. (3.12)) can be determined.

The shear relaxation modulus $G(t, \gamma)$ is then calculated by

$$G(t, \gamma) = \frac{\sigma_{12}(t)}{\gamma} = \frac{N_1}{\gamma^2} \quad (3.16)$$

Step-strain experiments were realised with the cone-and-plate geometry of the RMS800 of Rheometric Scientific. The drive system has a maximum angular displacement of $\vartheta = 0.5 \text{ rad}$ which leads for a cone angle of $\beta = 0.1 \text{ rad}$ to a maximum strain of

$$\gamma_{max} = \vartheta/\beta = 5 \quad (3.17)$$

This maximum strain can be doubled by first displacing the driven part in one direction by $\gamma = -5$ and then, after relaxation of the sample, displacing it to $\gamma = +5$. This procedure leads to a maximum strain of $\gamma_{max} = 10$.

The strain range could be further increased by choosing a smaller cone angle but with the danger of causing errors in the stress measurements [48]. Another possibility is the use of the plate-and-plate geometry and to decrease the gap between the two plates [20], [71]. But for the plate-and-plate geometry, a correction term is necessary in the non-linear strain region to account for the inhomogeneity of the strain due to its dependence on the radius r .

4 Material characterisation and sample preparation

4.1 Linear polymer melts

4.1.1 HDPE I

Melt HDPE I is a commercial high density polyethylene (Statoil 870H, Statoil/Norway), stabilised by Ciba/Switzerland [23]. Infrared measurements showed that melt HDPE I consists only of linear molecules and does not contain long-chain branches [27]. Properties and test conditions for HDPE I are summarised below:

Weight-averaged molecular weight	$M_W = 104000 \text{ g/Mol}$
Number-averaged molecular weight	$M_n = 18900 \text{ g/Mol}$
	$M_W/M_n = 5.5$
Melting temperature	$T_m = 138 \text{ }^\circ\text{C}$
Test temperature for extension	$T = 150 \text{ }^\circ\text{C}$
Test temperature for shear	$T = 170 \text{ }^\circ\text{C}$
Density at room temperature	$\rho_{RT} = 0.951 \text{ g/cm}^3$
Density at test temperature for extension	$\rho_T = 0.778 \text{ g/cm}^3$
Activation energy	$E_a = 27.0 \text{ kJ/Mol}$

i	g_i [Pa]	τ_i [s] ($150 \text{ }^\circ\text{C}$)	τ_i [s] ($170 \text{ }^\circ\text{C}$)
1	1.535E+05	1.414E-02	1.000E-02
2	3.187E+04	1.414E-01	1.000E-01
3	7.818E+03	1.414E+00	1.000E+00
4	1.413E+03	1.414E+01	1.000E+01
5	1.986E+02	1.414E+02	1.000E+02
6	2.065E+01	1.414E+03	1.000E+03
7	4.582E+00	7.069E+03	5.000E+03

Table 4.1: Relaxation spectrum of HDPE I at $150 \text{ }^\circ\text{C}$ and $170 \text{ }^\circ\text{C}$.

With a shift factor $a_T = 0.707$, the relaxation spectrum at $150 \text{ }^\circ\text{C}$ can be shifted to a temperature of $170 \text{ }^\circ\text{C}$ by multiplying the relaxation times with a_T (table 4.1).

Melt HDPE I was investigated by Kraft (1996) [27], [28] in shear, and by Hachmann (1996) [23] in multiaxial extensions with the rotary clamp technique. Experiments in shear with rotational rheometry (chapt. 6.3), and in uniaxial extension with the RME were repeated in this work to verify the results. In addition, step-shear strain experiments were performed, and a damping function was derived from the measured shear relaxation modulus (chapt. 6.3). For the extensional experiments, samples prepared by

Hachmann [23] were extruded before compression moulding (900 min at a temperature of 170 °C and 35 bar). In this work, samples for RME measurements were compression moulded from pellets at IKT. To obtain more homogeneous samples, two plates were produced independently by compression moulding and then remelted together in the moulding form, and compression moulded again for 120 min at a temperature of 170 °C, applying a pressure of 30 bar.

4.1.2 PS

Melt PS is a radically polymerised polystyrene (PS158K, BASF AG/Germany), and is clearly free of any long-chain branches [23]. It is characterised by

Weight-averaged molecular weight	$M_W = 336000$ g/Mol
Number-averaged molecular weight	$M_n = 125000$ g/Mol
	$M_W/M_n = 2.85$
Glass transition temperature	$T_g = 98$ °C
Test temperature	$T = 170$ °C
Density at room temperature	$\rho_{RT} = 1.05$ g/cm ³
Density at test temperature	$\rho_T = 0.979$ g/cm ³

i	g_i [Pa]	τ_i [s]
1	1.120E+05	6.134E-03
2	5.579E+04	5.270E-02
3	4.049E+04	3.106E-01
4	2.199E+04	1.611E+00
5	7.545E+03	7.718E+00
6	1.396E+03	3.998E+01
7	1.565E+02	3.043E+02

Table 4.2: Relaxation spectrum of PS at 170 °C.

Melt PS was investigated by Hachmann (1996) [23] in uniaxial and equibiaxial extension. Again, pellets were extruded before compression moulding [23] to produce homogenous samples (10 min at a temperature of 190 °C and 35 bar).

4.2 Long-chain-branched polymer melts

4.2.1 LDPE I

Melt LDPE I is a commercial, low-density polyethylene melt (Lupolen 1810H, BASF AG/Germany) with long-chain branches [23], stabilised by Ciba/Switzerland. Its characteristic properties and test temperature are:

Weight-averaged molecular weight	$M_W = 188000$ g/Mol
Number-averaged molecular weight	$M_n = 16600$ g/Mol
	$M_W/M_n = 11.3$
Melting temperature	$T_m = 110$ °C
Test temperature	$T = 150$ °C
Density at room temperature	$\rho_{RT} = 0.917$ g/cm ³
Density at test temperature	$\rho_T = 0.778$ g/cm ³
Activation energy	$E_a = 58.6$ kJ/Mol

i	g_i [Pa]	τ_i [s]
1	5.202E+04	1.000E-02
2	2.968E+04	1.000E-01
3	9.797E+03	1.000E+00
4	2.578E+03	1.000E+01
5	2.746E+02	1.000E+02
6	4.587E+00	1.000E+03

Table 4.3: Relaxation spectrum of LDPE I at 150 °C.

Melt LDPE I was again investigated by Kraft (1996) [27], [28] in shear, and by Hachmann (1996) [23] in multiaxial extensions. Experiments in shear with rotational rheometry and in uniaxial extension with the RME were repeated in this work to verify the results (chapt. 6.4). Additionally, step-shear strain experiments were performed to derive a damping function from the shear relaxation modulus (chapt. 6.4). Samples were prepared by compression moulding for 30 min at a temperature of 170 °C and a pressure of 25 bar.

4.2.2 PP II

Melt PP II is a propylene homopolymer with long-chain branches. Long-chain-branching is achieved by electron radiation [30]. The characteristic properties of melt PP II and the test temperature are:

Weight-averaged molecular weight	$M_W = 586600$ g/Mol
Number-averaged molecular weight	$M_n = 61750$ g/Mol
	$M_W/M_n = 9.5$
Melting temperature	$T_m = 162.4$ °C
Test temperature	$T = 180$ °C
Density at room temperature	$\rho_{RT} = 0.909$ g/cm ³
Activation energy	$E_a = 54.9$ kJ/Mol

i	g_i [Pa]	τ_i [s]
1	5.647E+04	4.411E-03
2	1.404E+04	3.252E-02
3	6.240E+03	2.241E-01
4	2.152E+03	1.483E+00
5	6.768E+02	1.061E+01
6	1.231E+02	7.449E+01
7	2.149E+01	5.045E+02

Table 4.4: Relaxation spectrum of PP II at 180 °C.

Melt PP II was investigated with a Mnstedt type tensile rheometer (MTR) by Kurzbeck (1999) [29], [30]. Pellets were extruded through a capillary die and cut into cylindrically-shaped samples. Afterwards, samples were allowed to anneal for 30 min in a silicon oil bath at 180 °C to remove residual stresses.

5 Experimental results and comparison to theory

In the molecular stress function theory (chapt. 2.4.3), the molecular stress function f was originally supposed to be a function of $\langle u' \rangle_0$ [85], [86], [87]. Later, it was shown [80] that f can alternatively be derived from a strain energy function, which leads to a dependence of f on the average logarithmic stretch $\langle \ln(u') \rangle_0$ instead of $\langle u' \rangle_0$. $\langle \ln(u') \rangle_0$ represents the relative orientational free energy of the average tube segment. The contour length of the tube is then given by

$$L = L_0 e^{\langle \ln(u') \rangle_0} \quad (5.1)$$

While the difference of $\langle u' \rangle_0$ and $e^{\langle \ln(u') \rangle_0}$ is limited, the comparison of experimental results to the MSF theory will be based on Eq. (5.1).

5.1 Linear polymer melts

For linear polymer melts, Wagner and Schaeffer (1992) [85] proposed an affine deformation of the average tube diameter with increasing deformation which corresponds to a constant tube volume (see the corresponding Eq. (2.125) in chapt. 2.4.3),

$$\frac{V}{V_0} = \frac{a^2 L}{a_0^2 L_0} = \frac{a^2}{a_0^2} e^{\langle \ln(u') \rangle_0} = 1 \quad (5.2)$$

By use of Eq. (5.1), the molecular stress function f^2 follows immediately as

$$f^2 = \frac{a_0^2}{a^2} = \frac{L}{L_0} = e^{\langle \ln(u') \rangle_0} \quad (5.3)$$

with the average logarithmic stretch $\langle \ln(u') \rangle_0$. Since f^2 is linear in the scalar stretch L/L_0 seen by the average tube segment, this equation is called the "Linear Molecular Stress Function (LMSF)" theory [80], [82].

While V is the hypothetical volume of the average tube segment assuming affine deformation, the physical length L_m of the average tube segment occupied by the macromolecular chain is given by the line density $n/L_m = a/b^2$ of monomers in the tube which leads to [80]

$$L_m = L_0 \frac{a_0}{a} = L_0 f = L_0 e^{\frac{1}{2} \langle \ln(u') \rangle_0} \quad (5.4)$$

Hence, the increase of L_m is only proportional to the square root of the stretch field L , i.e. the physical length L_m is not deformed affinely in contrast to the tube diameter. Consequently, f^2 in Eq. (5.3) describes a non-affine deformation.

Predictions of the non-linear strain measure $\underline{\underline{S}}_{LMSF}$ of the LMSF theory with $\underline{\underline{S}}_{DE}^{IA}$ (Eq. 2.106),

$$\underline{\underline{S}}_{LMSF} = f^2 \underline{\underline{S}}_{DE}^{IA} = e^{\langle \ln(u') \rangle_0} \underline{\underline{S}}_{DE}^{IA} \quad (5.5)$$

describe an unbounded growth of the extensional viscosities in contrast to the experimentally observed behaviour of polymer melts which approach steady-state viscosities at large deformations.

To take into account this saturation effect, the rate-of-change of f^2 according to the LMSF theory is considered

$$\frac{\partial f^2}{\partial t} = \frac{1}{L_0} \frac{dL}{dt} = e^{\langle \ln(u') \rangle_0} \frac{\partial \langle \ln(u') \rangle_0}{\partial t} = e^{\langle \ln(u') \rangle_0} \underline{\underline{\kappa}} : \underline{\underline{S}} \quad (5.6)$$

where use has been made of the relation [32], [82]

$$\frac{\partial \langle \ln(u') \rangle_0}{\partial t} = \underline{\underline{\kappa}} : \left\langle \frac{u' u'}{u'^2} \right\rangle_0 = \underline{\underline{\kappa}} : \underline{\underline{S}} \quad (5.7)$$

$\underline{\underline{S}}$ is the second order orientation tensor (chapt. 2.4.1). Thus, $\partial f^2 / \partial t$ is seen to be equal to the velocity of the stretch field L/L_0 .

If the assumption is made that at larger deformations an increasing slip between the stretching and the stretch field occurs, Eq. (5.6) is changed to

$$\frac{\partial f^2}{\partial t} = (1 - \alpha) \frac{1}{L_0} \frac{dL}{dt} = \left(1 - \frac{f^2 - 1}{f_{max}^2 - 1} \right) e^{\langle \ln(u') \rangle_0} \underline{\underline{\kappa}} : \underline{\underline{S}} \quad (5.8)$$

The slip factor $\alpha = (f^2 - 1)/(f_{max}^2 - 1)$ is equal to zero for $f^2 = 1$, and equal to one (i.e. total slip) for $f^2 = f_{max}^2$. In this way, a maximum value of the molecular stress function, f_{max} , is introduced.

Integration of Eq. (5.8) leads to the following relation for f^2 ,

$$f^2 = 1 + (f_{max}^2 - 1) \left[1 - \exp \left(- \frac{e^{\langle \ln(u') \rangle_0} - 1}{f_{max}^2 - 1} \right) \right] \quad (5.9)$$

which degenerates to Eq. (5.3) at small strains. The strain measure resulting from Eq. (5.9) with the non-linear material parameter f_{max} will simply be denoted by MSF in the following.

Predictions of the non-linear strain measures of the Doi-Edwards (DE) theory, and of the LMSF and MSF model will be presented in comparison to experimental data of a linear polyethylene melt (HDPE I), and a polystyrene melt (PS).

5.1.1 HDPE I

Figs. 5.1-5.4 show the uniaxial or elongational (μ_u), the equibiaxial (μ_e), and both planar (μ_{p1}, μ_{p2}) viscosities of melt HDPE I measured by Hachmann (1996) [23] at a temperature of 150 °C and at constant strain-rates $\dot{\epsilon}_0$ between 0.003 and 1 s⁻¹. Included in the figures is the zero-shear viscosity $\eta_0(t)$. All extensional viscosities are rescaled to $\eta_0(t)$. Melt HDPE I shows a comparatively strong strain-hardening behaviour, which is due to the addition of a high molecular weight fraction. Long-chain-branching, usually responsible for enhanced strain-hardening, can be excluded due to IR measurements of Kraft (1996) [27] who detected no branching. Linster and Meissner (1986) [35] investigated several HDPE melts and found that enhanced strain-hardening effects can be produced by a small amount of very long, linear molecules in the molecular weight distribution.

To demonstrate the inability of the Doi-Edwards (DE) model to describe the strain-hardening behaviour in extensional flows, predictions of the non-linear strain measure $\underline{\underline{S}}_{DE}^{IA}$ (Eq. (2.106)) are presented in figs. 5.1-5.4. It is obvious that the DE theory cannot predict any strain-hardening in extensional flows. In contrast, the non-linear strain measure $\underline{\underline{S}}_{LMSF}$ (Eq. (5.5)) of the LMSF theory allows a precise prediction of the viscosity upturn of μ_u , μ_e and μ_{p1} up to large deformations, and even describes the effect that no strain-hardening behaviour is observed for the second planar viscosity μ_{p2} . It should be noted that this is possible with a simple exponential dependence on the average logarithmic stretch $\langle \ln(u') \rangle_0$ and without any non-linear parameter. To take into account the saturation effect of extensional viscosities at large deformations, a maximum value f_{max} of the molecular stress function was introduced in Eq. (5.9). The resulting non-linear strain measure $\underline{\underline{S}}_{MSF}$ allows a consistent description of all extensional modes with $f_{max}^2 = 30$, estimated from the steady-state elongational viscosity μ_u of melt HDPE I. This corresponds to a maximum stretch ratio of the macromolecular chains of $f_{max} = 5.5$. For the uniaxial and first planar viscosity, a slight discrepancy between the experimental data and the predictions exists with an overprediction at high strain-rates and an underprediction at low strain-rates. At low strain-rates, as shown before (chapt. 3.1.2), enhanced strain-hardening is often only an artefact due to problems in the force measurement system. At large strain-rates, the sample often ruptures before steady-state values are reached.

With the MSF model it is thus possible to describe extensional flows of melt HDPE I consistently by use of the linear-viscoelastic relaxation spectrum and just **one** non-linear material parameter f_{max} , determined from uniaxial experiments.

In the following the shear flow rheology of melt HDPE I in start-up flow tests is presented, investigated by Kraft (1996) [27] at a temperature of 170 °C. Figs. 5.5 and 5.7 show the shear viscosity $\eta(\dot{\gamma}, t)$ (Eq. (2.29)) of melt HDPE I for shear-rates $\dot{\gamma}$ between 0.001 and 10 s⁻¹. All curves pass through a maximum before reaching steady-state. Even at the smallest shear-rate, the linear regime, i.e. the zero-shear viscosity

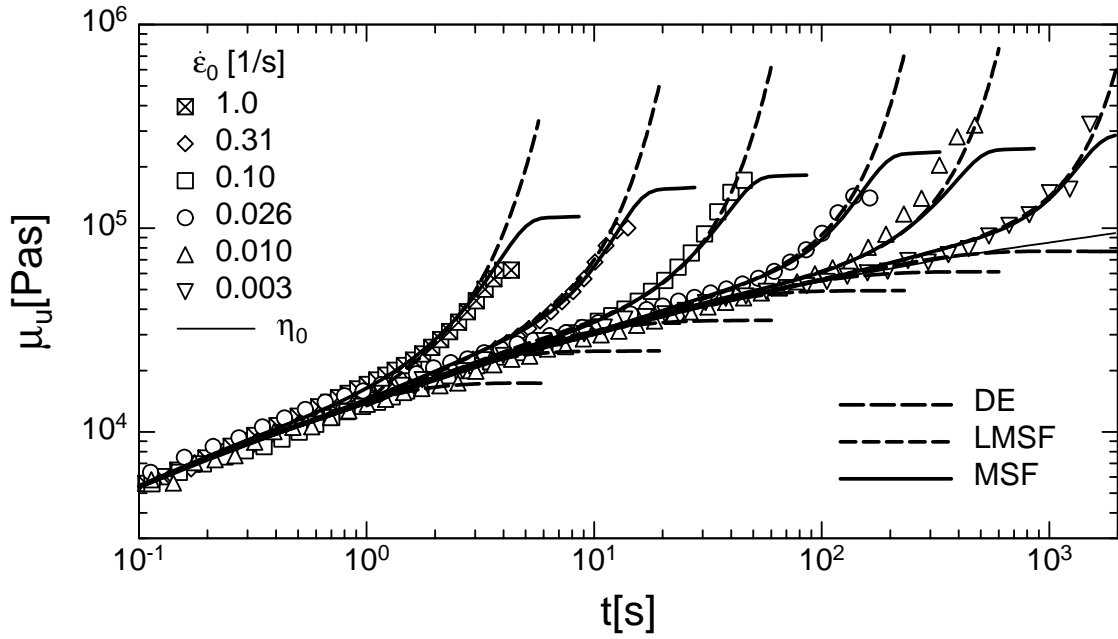


Figure 5.1: Elongational viscosity μ_u of melt HDPE I at a temperature of $T = 150 \text{ }^\circ\text{C}$, with $f_{max}^2 = 30$ (Eq. (5.9)).

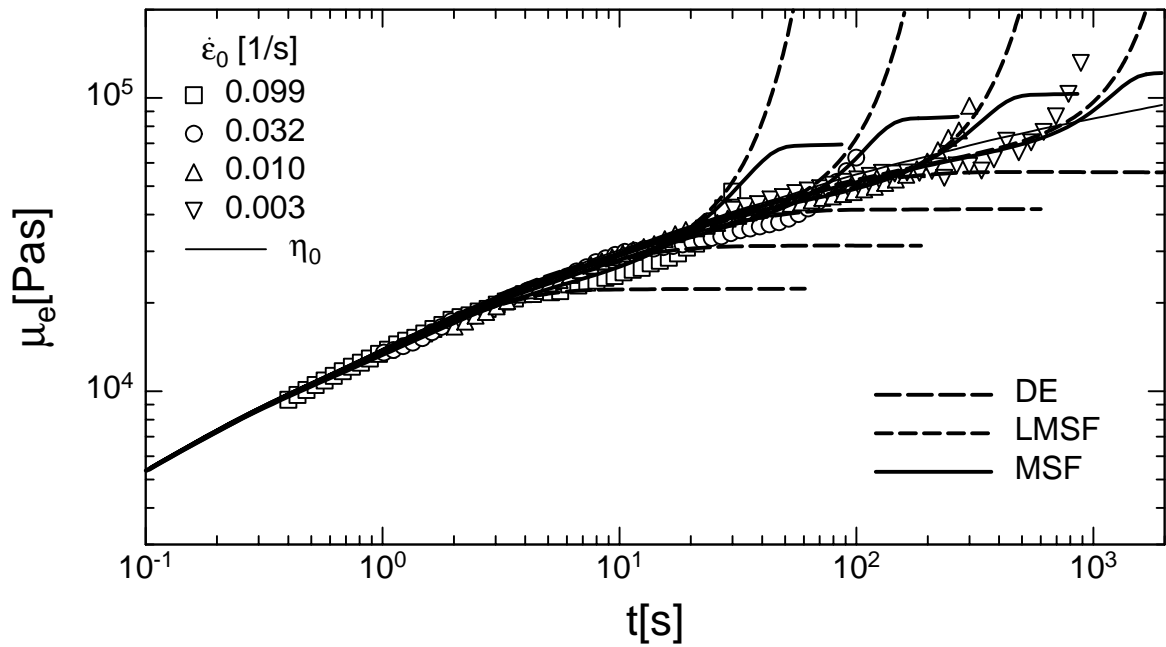


Figure 5.2: Equibiaxial viscosity μ_e of melt HDPE I at a temperature of $T = 150 \text{ }^\circ\text{C}$, with $f_{max}^2 = 30$ (Eq. (5.9)).

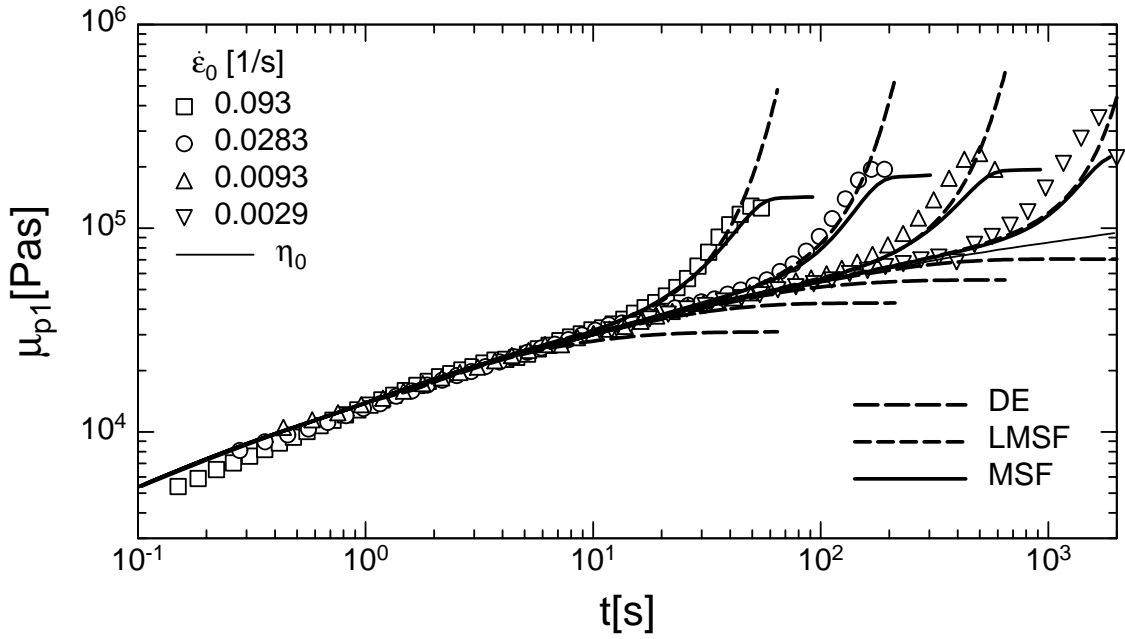


Figure 5.3: First planar viscosity μ_{p1} of melt HDPE I at a temperature of $T = 150 \text{ }^\circ\text{C}$, with $f_{max}^2 = 30$ (Eq. (5.9)).

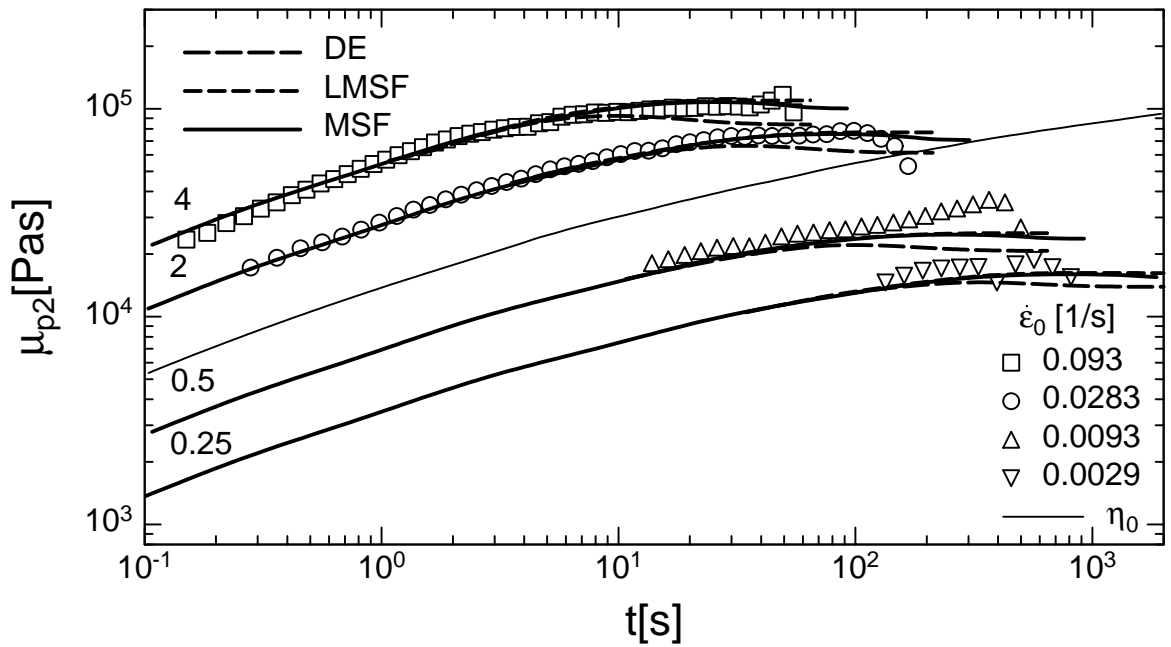


Figure 5.4: Second planar viscosity μ_{p2} of melt HDPE I at a temperature of $T = 150 \text{ }^\circ\text{C}$, with $f_{max}^2 = 30$ (Eq. (5.9)), shifted for clarity by the factors indicated.

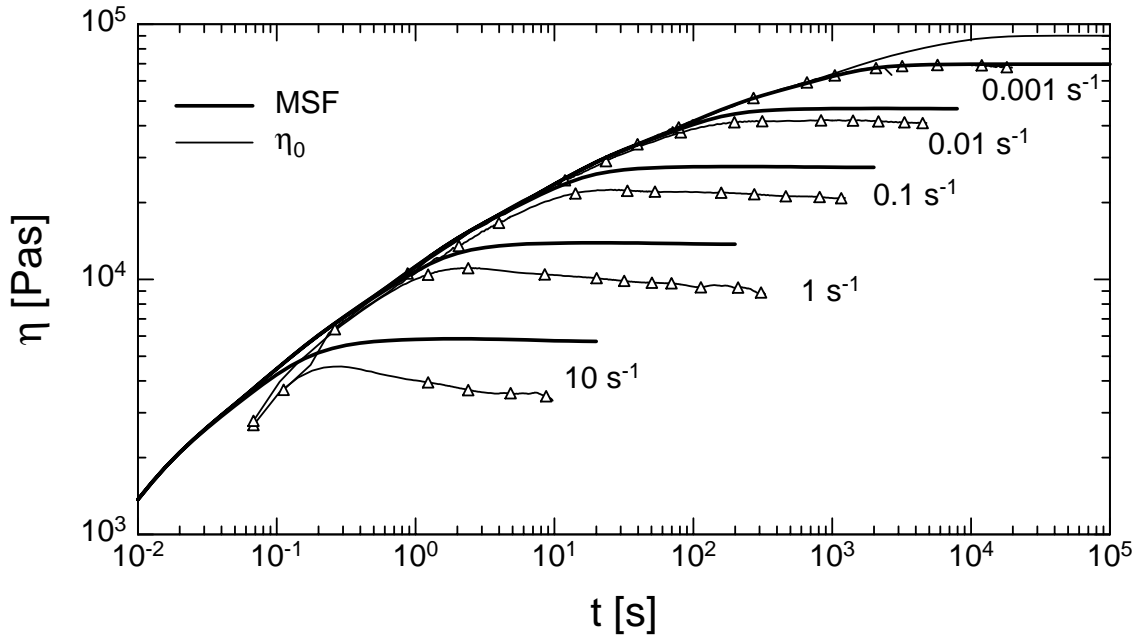


Figure 5.5: Shear viscosity η of melt HDPE I at a temperature of $T = 170\text{ }^\circ\text{C}$, with $f_{max}^2 = 30$ (Eq. (5.9)), determined from extensional data.

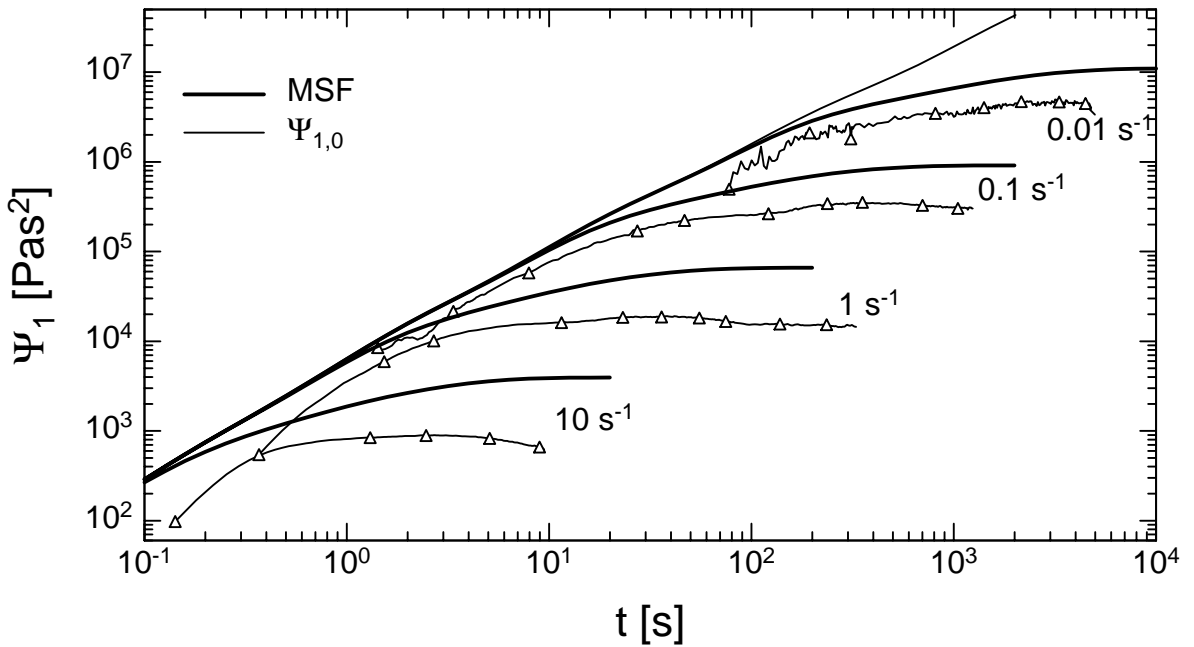


Figure 5.6: First normal stress coefficient Ψ_1 of melt HDPE I at a temperature of $T = 170\text{ }^\circ\text{C}$, with $f_{max}^2 = 30$ (Eq. (5.9)), determined from extensional data.

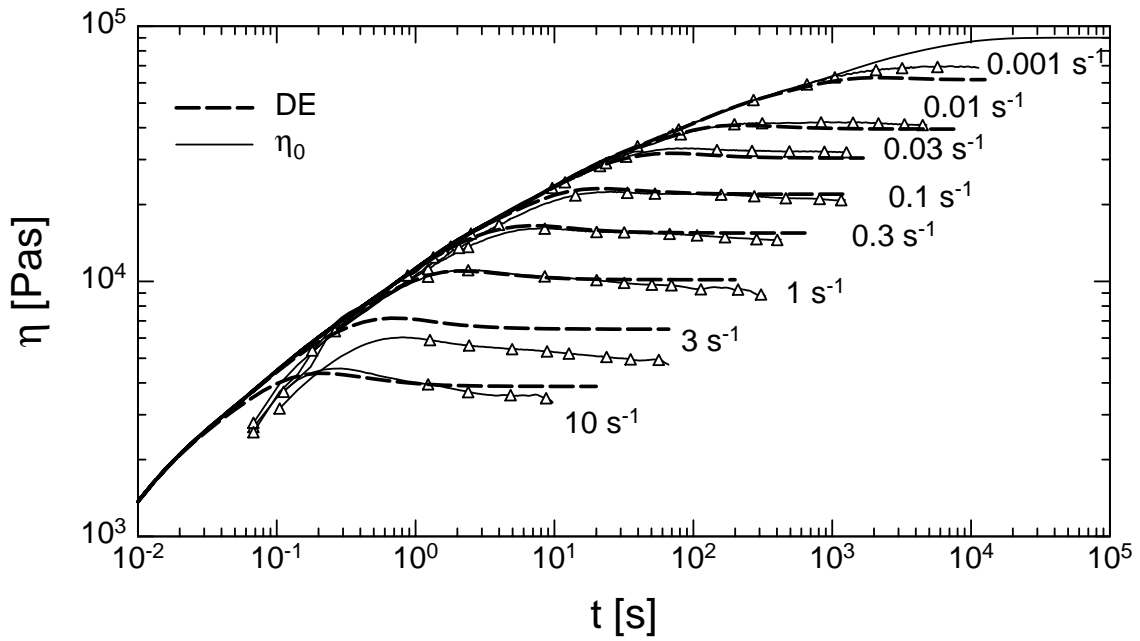


Figure 5.7: Shear viscosity η of melt HDPE I at a temperature of $T = 170\text{ }^\circ\text{C}$ and comparison to the DE model (Eq. (2.107)).

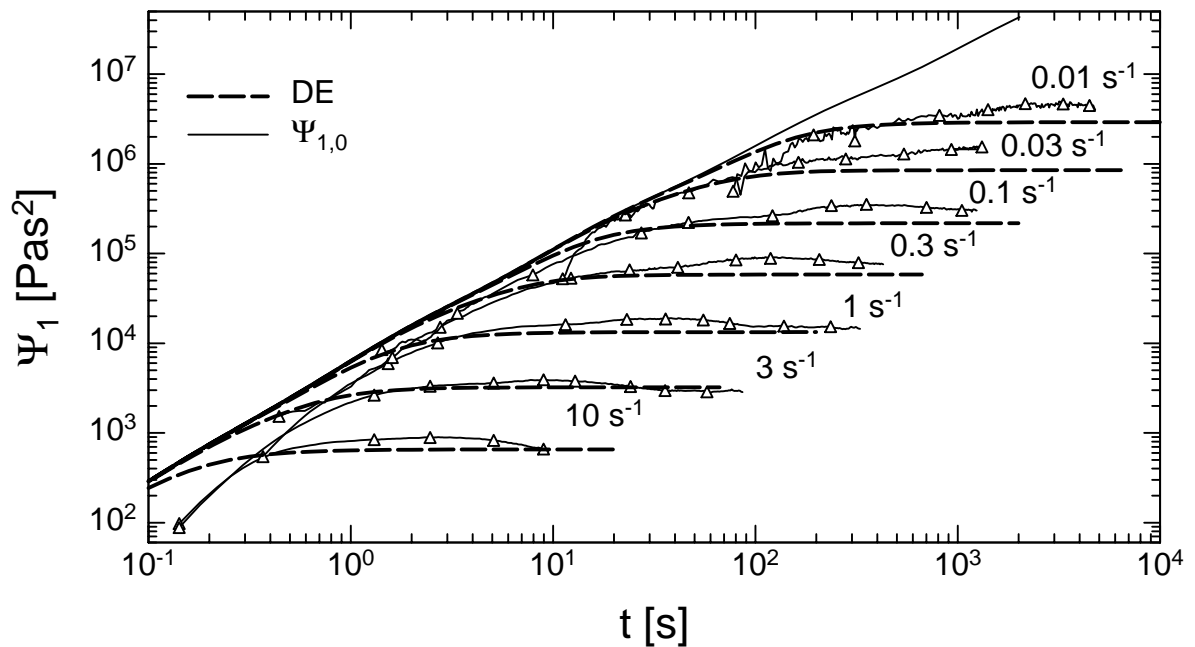


Figure 5.8: First normal stress coefficient Ψ_1 of melt HDPE I at a temperature of $T = 170\text{ }^\circ\text{C}$ and comparison to the DE model (Eq. (2.107)).

$\eta_0(t)$, is not reached. In figs. 5.6 and 5.8, the corresponding first normal stress function $\Psi_1(\dot{\gamma}, t)$ (Eq. (2.30)) is presented for shear-rates $\dot{\gamma}$ between 0.01 and 10 s^{-1} . All curves form a common envelope at small deformations, presented by the linear-viscoelastic function $\Psi_{1,0}$, which is calculated from the spectrum of relaxation times (Eq. (2.57)). The experimental data are compared in figs. 5.5 and 5.6 to the predictions of the MSF theory with $f_{max}^2 = 30$, a value which was found to be appropriate for extensional flows. But both $\eta(\dot{\gamma}, t)$ and $\Psi_1(\dot{\gamma}, t)$ are clearly overpredicted for all shear-rates by the MSF theory with $f_{max}^2 = 30$, and the discrepancy between experiment and theory increases with increasing shear-rate.

Surprisingly, predictions of the non-linear strain measure $\underline{\underline{S}}_{DE}^{IA}$ of the Doi-Edwards (DE) theory show good agreement with experimental data for both $\eta(\dot{\gamma}, t)$ (fig. 5.7) and $\Psi_1(\dot{\gamma}, t)$ (fig. 5.8), and for all shear-rates. The shear viscosity $\eta(t)$ is predicted nearly quantitatively including the maximum of $\eta(t)$ before reaching steady-state. The disagreement for the shear-rate $\dot{\gamma} = 3 s^{-1}$ seems to be an experimental error which is confirmed by new measurements (see chapt. 6.3). Since the DE model does not describe a maximum in the normal stress difference, the $\Psi_1(\dot{\gamma}, t)$ curves are slightly underpredicted, mainly in the region of the maximum.

The discrepancy in the description of shear and extensional rheology of melt HDPE I will be considered in more detail in chapter 6.

In the appendix, the uniaxial viscosity of other linear polymer melts is presented. In particular, two linear high density polyethylenes (HDPE II and III), two linear low density polyethylenes (LLDPE, POP), and two polypropylenes (PP I and III) are considered. Measurements were performed either by use of our elongational rheometer RME or by other commercial RMEs, or by Münstedt type tensile rheometers (MTR). The experimental data are compared to the MSF model of Eq. (5.9) with the non-linear material parameter f_{max} . An encouraging agreement is found between theory and experiment. Depending on the different strain-hardening behaviour of the investigated linear melts, the maximum stretch of the macromolecular chains is between $f_{max} = 1.3$ and $f_{max} = 5.5$. Hence, f_{max} allows to quantify differences in the strain-hardening behaviour. Since the MSF model describes biaxial extensions with f_{max} estimated from the uniaxial experiment (which can be performed by use of a commercial instrument), it is possible to predict the equibiaxial and both planar viscosities for all linear polymer melts investigated.

5.1.2 PS

In figs. 5.9 and 5.11, the uniaxial (μ_u) and equibiaxial (μ_e) viscosities of the polystyrene (PS) melt are shown, measured by Hachmann (1996) [23] at a temperature of 170 °C and at constant strain-rates $\dot{\epsilon}_0$ between 0.003 and 1.5 s^{-1} . Both viscosities are rescaled to the zero-shear viscosity $\eta_0(t)$. The melt PS shows considerable strain-hardening

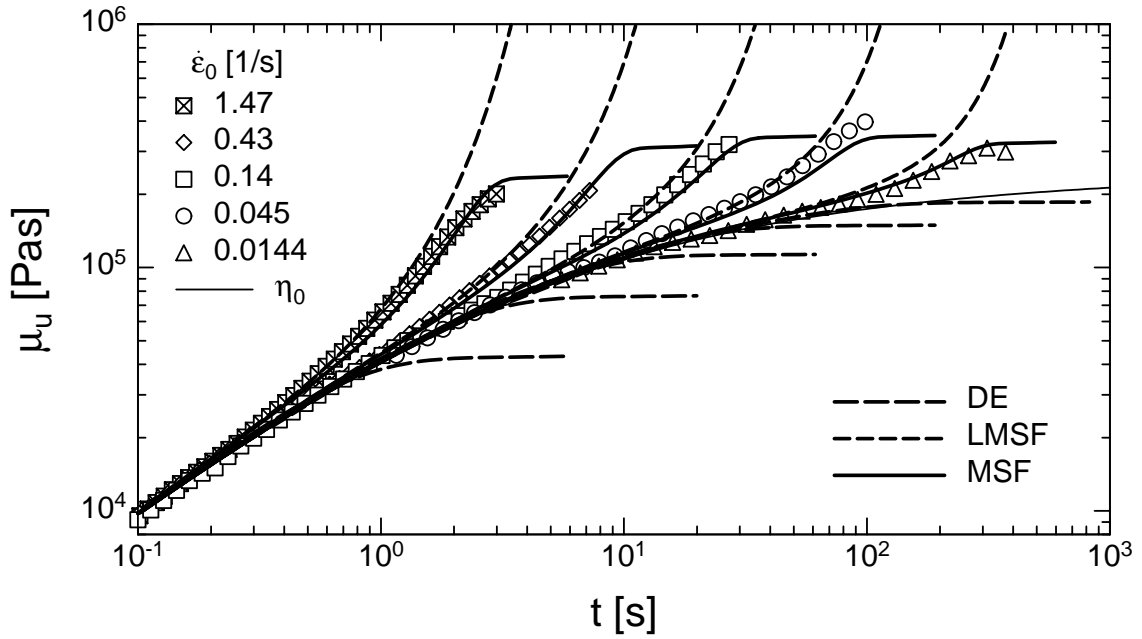


Figure 5.9: Elongational viscosity μ_u of melt PS at a temperature of $T = 170\text{ }^\circ\text{C}$, with $f_{max}^2 = 13$ (Eq. (5.9)).

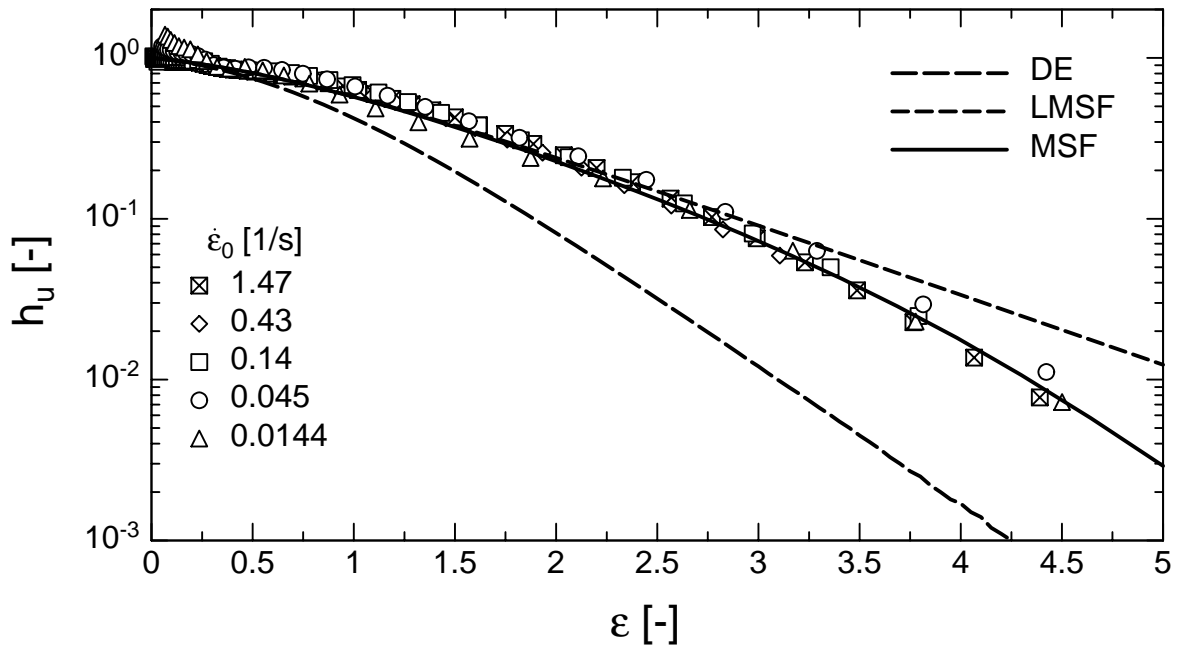


Figure 5.10: Damping function h_u of melt PS calculated from elongational viscosity, with $f_{max}^2 = 13$ (Eq. (5.9)).

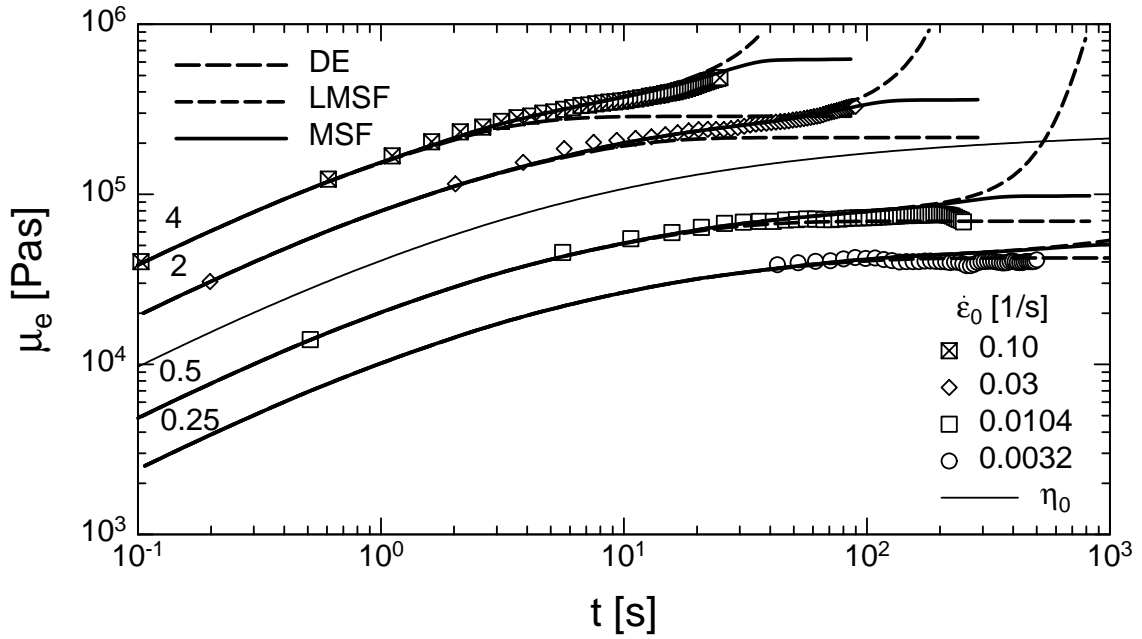


Figure 5.11: Equibiaxial viscosity μ_e of melt PS at a temperature of $T = 170 \text{ }^\circ\text{C}$, with $f_{max}^2 = 13$ (Eq. (5.9)), shifted for clarity by the factors indicated.

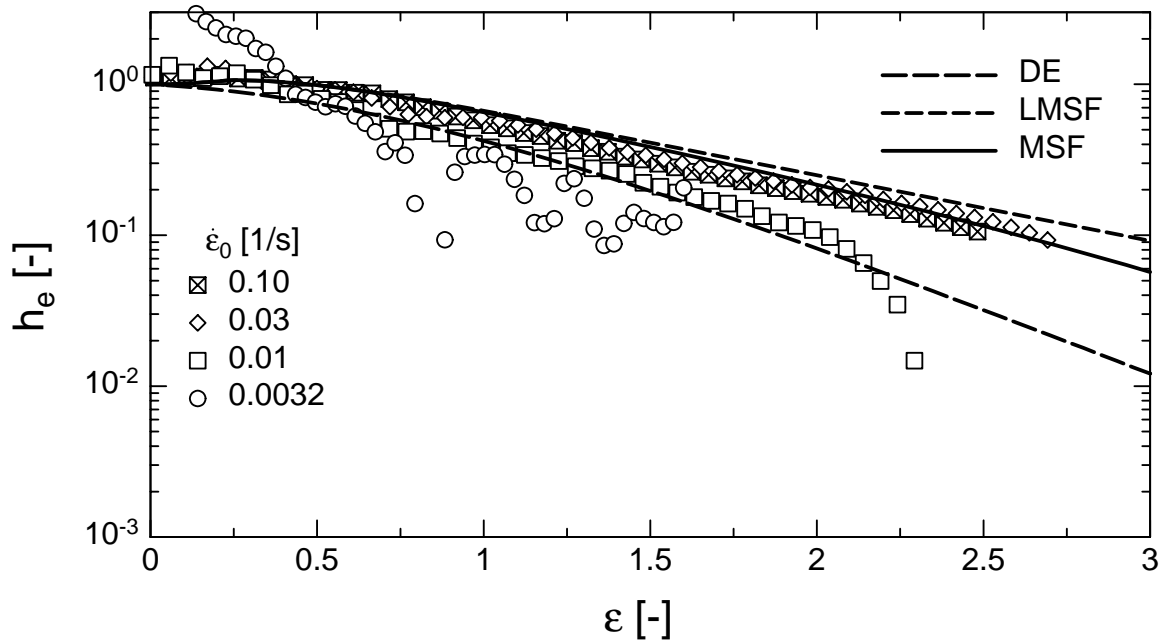


Figure 5.12: Damping function h_e of melt PS calculated from equibiaxial viscosity, with $f_{max}^2 = 13$ (Eq. (5.9)).

in uniaxial extension, although it is free of any long-chain branches, and only little strain-hardening in equibiaxial extension. By use of the linear relaxation spectrum (chapt. 4.1.2), the uniaxial (h_u) and equibiaxial (h_e) damping functions were calculated from the extensional viscosities (figs. 5.10 and 5.12).

Included in all figures are the predictions of the non-linear strain measure of the DE model, the LMSF model of Eq. (5.3) and the MSF model of Eq. (5.9) with a maximum molecular stress function of $f_{max} = 3.6$ (corresponding to $f_{max}^2 = 13$). Although the LMSF model describes the upturn of the viscosities up to rather large deformations, and the damping functions up to a Hencky strain of $\varepsilon_H \approx 1.5$, the MSF model with the non-linear material parameter f_{max} is needed to fit the steady-state values. Fitted to the uniaxial viscosity, the same f_{max} allows to describe the equibiaxial viscosity, although it exhibits only little strain-hardening, and both damping functions (h_u and h_e).

5.2 Long-chain-branched polymer melts

Long-chain-branched polymer melts show a much stronger upturn of the extensional viscosities with increasing deformation and cannot be described by a linear dependence of f^2 on the average logarithmic stretch $\langle \ln(u') \rangle_0$ [78]. To consider this enhanced stress growth, branch points are treated for simplicity as junctions of a cross-linked system [80], following the theory of rubber elasticity. Assuming (in contrast to the LMSF theory) an average affine deformation of cross-links, the length L_m of a network strand between cross-links is given by

$$L_m = L = L_0 e^{\langle \ln(u') \rangle_0} \quad (5.10)$$

upon a deformation by a stretch field L . With $f = a_0/a$ and $L_m a = L_0 a_0$, the square of the molecular stress function, f^2 , can be derived as

$$f^2 = \frac{L_m^2}{L_0^2} = e^{2\langle \ln(u') \rangle_0} \quad (5.11)$$

However, incorporating Eq. (5.11) into the non-linear strain measure $\underline{\underline{S}}_{MSF}$ of Eq. (2.123) even overpredicts the dependence of cross-linked systems, which demonstrates that the deformation of network strands must be non-affine [80].

In the theory of Flory (1976) [22], junction fluctuations are proposed, with

$$L_m^2 = \langle L_m \rangle^2 + (\Delta L_m)^2 \quad (5.12)$$

L_m is the instantaneous end-to-end length of a network strand or a tube segment, which can be presented as the sum of the mean $\langle L_m \rangle$ and a fluctuation ΔL_m from the

mean. According to Flory, $\langle L_m \rangle^2$ and $(\Delta L_m)^2$ are related to the average functionality φ of the network and to the stretch L by

$$\langle L_m \rangle^2 = \left(1 - \frac{2}{\varphi}\right) L^2 \quad (5.13)$$

and

$$(\Delta L_m)^2 = \frac{2}{\varphi} L_0^2 \quad (5.14)$$

respectively. Hence, the mean is deformed affinely with L , while the fluctuations are independent of the constraints. The molecular stress function can then be expressed as

$$f^2 = \frac{L_m^2}{L_0^2} = \left(1 - \frac{2}{\varphi}\right) e^{2\langle \ln(u') \rangle_0} + \frac{2}{\varphi} \quad (5.15)$$

or if an average functionality of $\varphi = 4$ is assumed [80], as

$$f^2 = \frac{1}{2} e^{2\langle \ln(u') \rangle_0} + \frac{1}{2} \quad (5.16)$$

Due to the quadratic dependence of f^2 on the stretch, Eq. (5.16) is called "Quadratic Molecular Stress Function (QMSF)" theory [80].

As in the case of the LMSF theory, predictions of the non-linear strain measure $\underline{\underline{S}}_{QMSF}$ of the QMSF theory with

$$\underline{\underline{S}}_{QMSF} = f^2 \underline{\underline{S}}_{DE}^{IA} = \left(\frac{1}{2} e^{2\langle \ln(u') \rangle_0} + \frac{1}{2}\right) \underline{\underline{S}}_{DE}^{IA} \quad (5.17)$$

describe an unbounded growth of the extensional viscosities, in contrast to the experimentally observed behaviour of polymer melts which show steady-state viscosities at large deformations. Again the rate-of-change of f^2 is regarded

$$\frac{\partial f^2}{\partial t} = \frac{1}{2L_0^2} \frac{dL^2}{dt} = e^{2\langle \ln(u') \rangle_0} \underline{\underline{\kappa}} : \underline{\underline{S}} \quad (5.18)$$

to model the steady-state behaviour at large deformations, with $\partial f^2 / \partial t$ being now proportional to the rate-of-change of the square of the stretch field L/L_0 .

By introducing slip and a maximum value f_{max}^2 of the molecular stress function,

$$\frac{\partial f^2}{\partial t} = \left(1 - \frac{(f^2 - 1)}{(f_{max}^2 - 1)}\right) \frac{1}{2L_0^2} \frac{dL^2}{dt} = \left(1 - \frac{(f^2 - 1)}{(f_{max}^2 - 1)}\right) e^{2\langle \ln(u') \rangle_0} \underline{\underline{\kappa}} : \underline{\underline{S}} \quad (5.19)$$

and by integration, the molecular stress function is given by

$$f^2 = 1 + (f_{max}^2 - 1) \left[1 - \exp\left(-\frac{e^{2\langle \ln(u') \rangle_0} - 1}{2(f_{max}^2 - 1)}\right)\right] \quad (5.20)$$

which reduces to Eq. (5.16) for small strains. As in the case of the LMSF model, the strain measure resulting from Eq. (5.20) with the non-linear material parameter f_{max} will be denoted by MSF. Note that "MSF" is used for both cases, linear and branched polymer melts, and it includes either the LMSF or QMSF theory at small deformations depending on the topology of the melt.

In the following, predictions of the non-linear strain measures of the Doi-Edwards (DE) theory, and of the LMSF, QMSF, and MSF model are compared to experimental data of a long-chain-branched polyethylene melt (LDPE I), and a long-chain-branched polypropylene melt (PP II).

5.2.1 LDPE I

Figs. 5.13-5.16 show the uniaxial (μ_u), equibiaxial (μ_e), and planar (μ_{p1}, μ_{p2}) viscosities of melt LDPE I measured by Hachmann (1996) [23] at a temperature of 150 °C and at constant strain-rates $\dot{\epsilon}_0$ between 0.003 and 1.04 s^{-1} . Again, all extensional viscosities are rescaled to the zero-shear viscosity $\eta_0(t)$. The non-linear strain measure $\underline{\underline{S}}_{DE}^{IA}$ of the Doi-Edwards (DE) model (Eq. (2.106)), including the IA approximation, clearly underpredicts all extensional viscosities. The orientation tensor $\underline{\underline{S}}_{DE}^{IA}$ is not able to predict strain-hardening, and is only responsible for orientation. Included into fig. 5.13 are the predictions of the LMSF theory of Eq. (5.5) to demonstrate that indeed the upturn of the uniaxial viscosity of the long-chain-branched polyethylene melt is more pronounced than for linear melts. This is not only the case for the uniaxial viscosity μ_u , but also for the extensional viscosities μ_e and μ_p [78], [80]. However, the upturn can be described quite accurately for all deformation modes by the zero-parameter model QMSF (Eq. (5.16)) shown for all extensional modes (figs. 5.13-5.16).

The steady-state values of the extensional viscosities cannot be described by the QMSF theory due to its exponential character and the resulting unlimited stress growth. But with a maximum value $f_{max}^2 = 100$, determined from the steady-state values of the uniaxial viscosity (μ_u) of melt LDPE I, a consistent description of all extensional modes is possible by use of Eq. (5.20). This corresponds to a maximum stretch ratio of the macromolecules by a factor of 10. The discrepancy between the steady-state viscosities predicted and observed seems to be more pronounced than in the case of melt HDPE I, with again an overprediction at high strain-rates and an underprediction at low strain-rates for the uniaxial and first planar viscosity. But again at high strain-rates, the tensile stress is very large which might lead to a rupture of the sample in such a way that no steady-state viscosities can be observed. Therefore, a slight overprediction of the viscosity might be reasonable. At low strain-rates, the underpredictions of strain-hardening are probably again due to an artefact caused by the force measurement system.

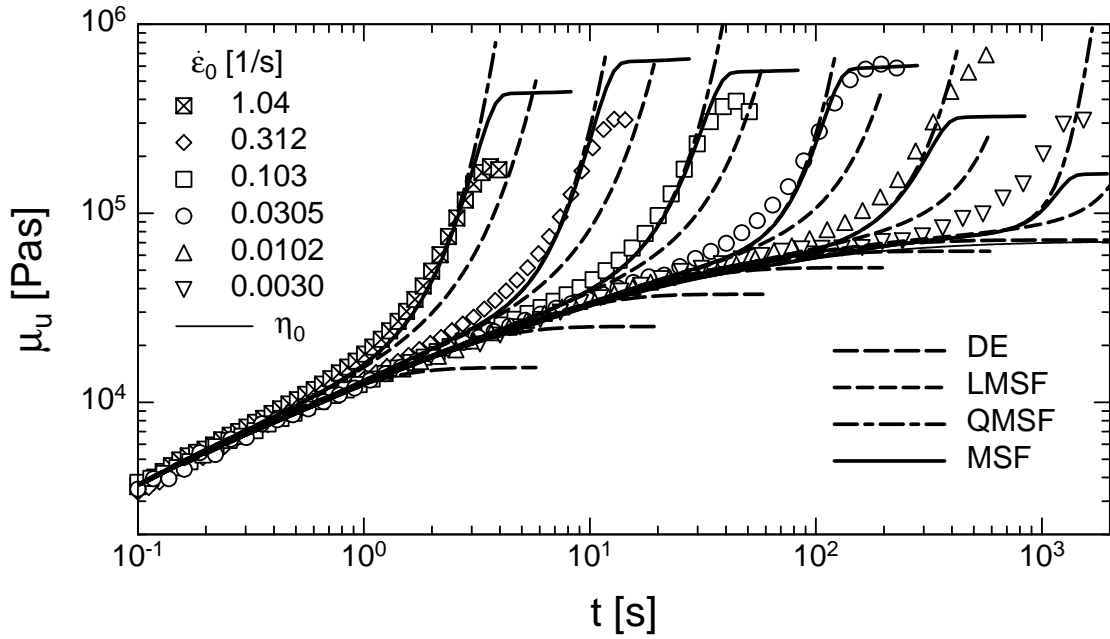


Figure 5.13: Elongational viscosity μ_u of melt LDPE I at a temperature of $T = 150 \text{ }^\circ\text{C}$, with $f_{max}^2 = 100$ (Eq. (5.20)).

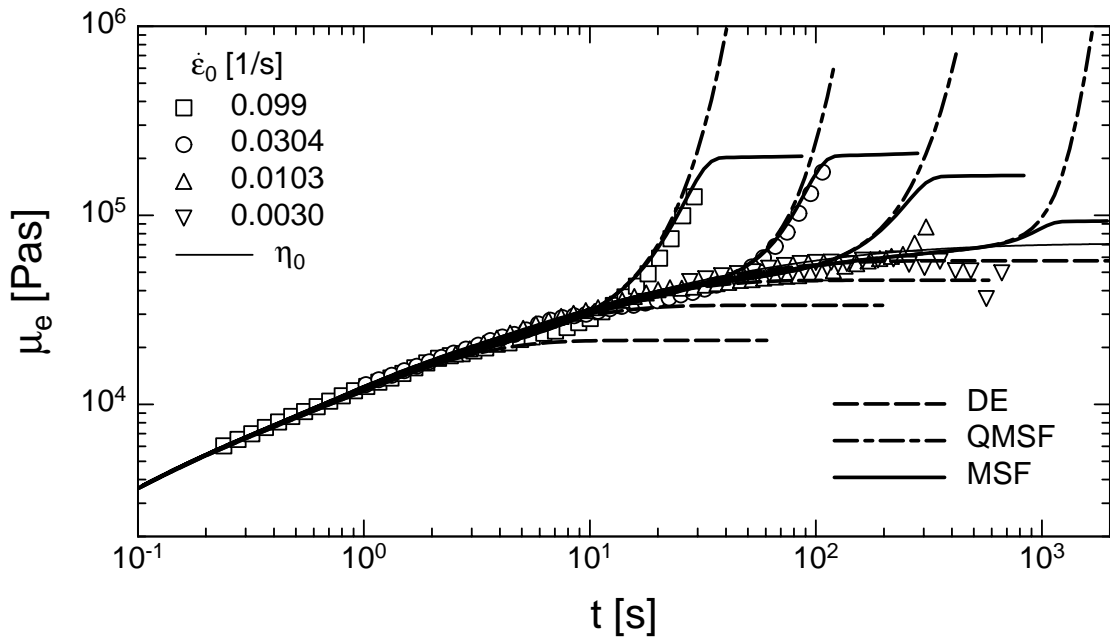


Figure 5.14: Equibiaxial viscosity μ_e of melt LDPE I at a temperature of $T = 150 \text{ }^\circ\text{C}$, with $f_{max}^2 = 100$ (Eq. (5.20)).

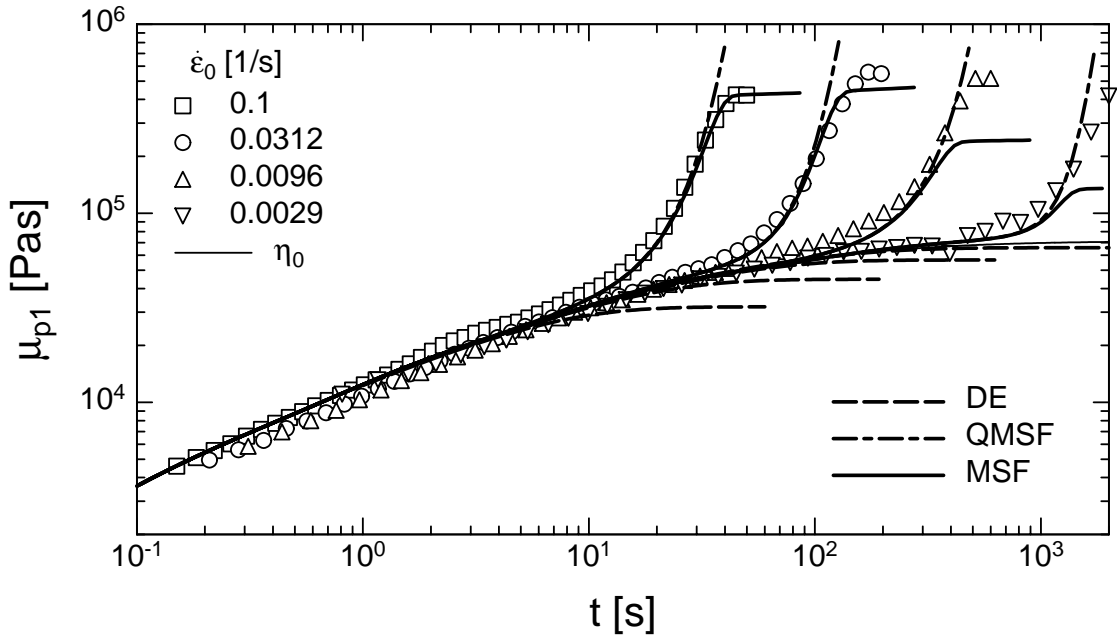


Figure 5.15: First planar viscosity μ_{p1} of melt LDPE I at a temperature of $T = 150 \text{ }^\circ\text{C}$, with $f_{max}^2 = 100$ (Eq. (5.20)).

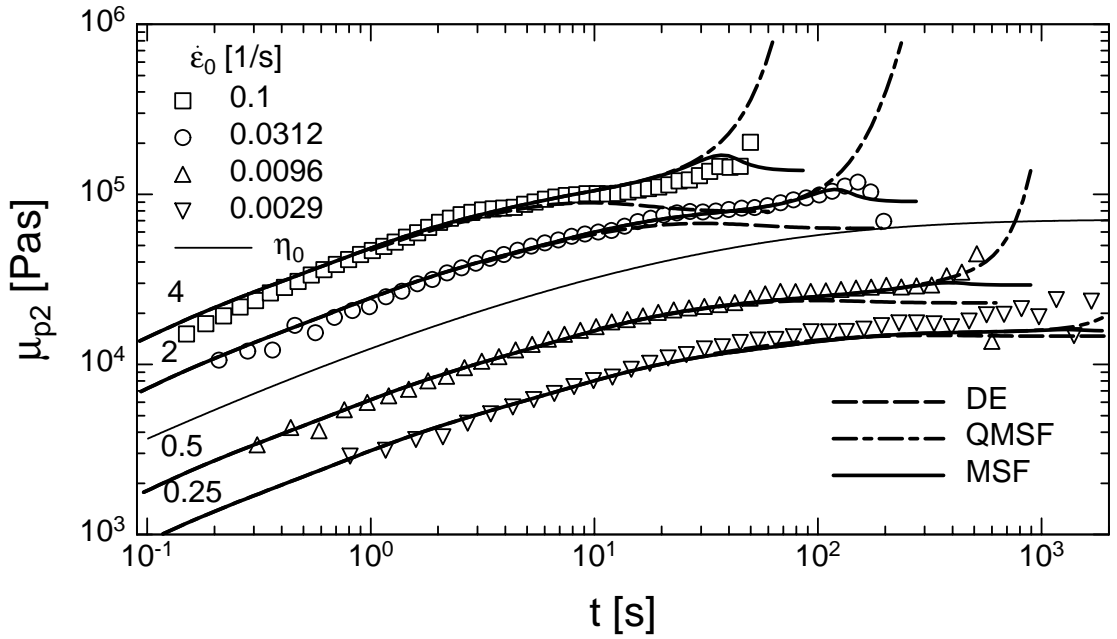


Figure 5.16: Second planar viscosity μ_{p2} of melt LDPE I at a temperature of $T = 150 \text{ }^\circ\text{C}$, with $f_{max}^2 = 100$ (Eq. (5.20)), shifted for clarity by the factors indicated.

New measurements of the uniaxial viscosity with our RME show that the MSF model is also able to describe the uniaxial viscosity at lower strain-rates with the same f_{max} , estimated from the viscosity at strain-rates in the mid-range (fig. 5.17). (By use of a new linear-viscoelastic relaxation spectrum, which gives a better fit to the new measurements, a new value of $f_{max}^2 = 50$ was found to describe the elongational viscosity of melt LDPE I). This is confirmed not only for melt LDPE I, but for several other

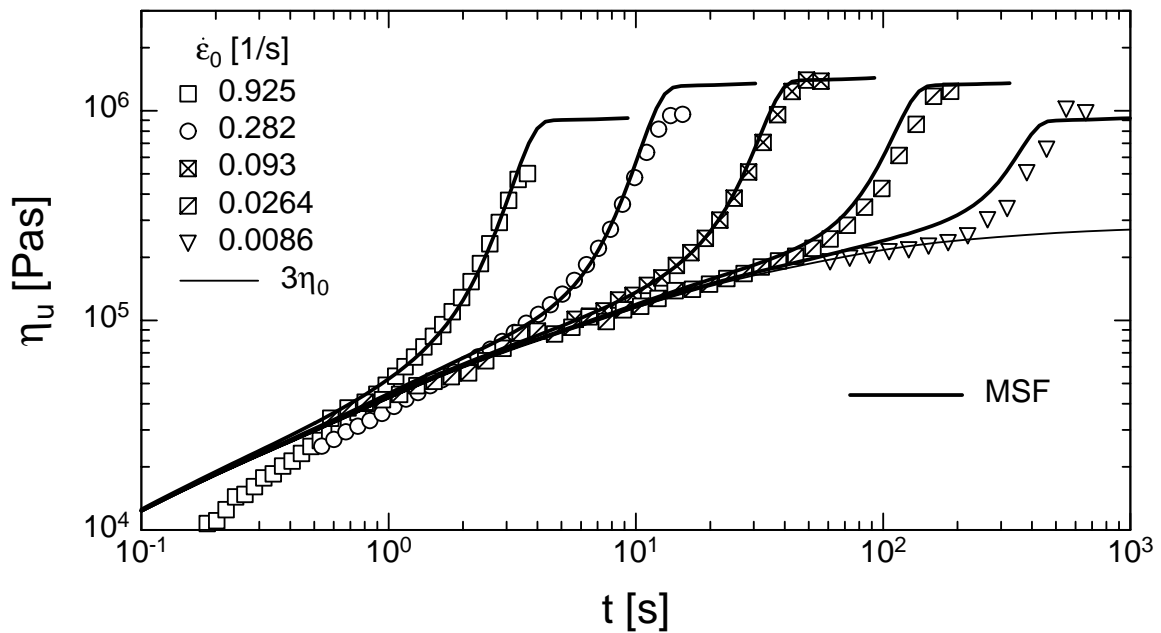


Figure 5.17: Elongational viscosity η_u of melt LDPE I at a temperature of $T = 150 \text{ }^\circ\text{C}$, with $f_{max}^2 = 50$ (Eq. (5.20)), and a new linear-viscoelastic relaxation spectrum (see appendix).

low density polyethylene melts, presented in the appendix. Thus, f_{max} does not seem to be strain-rate dependent.

With the MSF model it is possible to describe biaxial extensions of melt LDPE I uniformly with the linear-viscoelastic relaxation spectrum and just **one** non-linear material parameter f_{max} , determined from uniaxial experiments. The quality of the predictions of the MSF model for the uniaxial viscosity is confirmed for several long-chain-branched polymer melts in the appendix by different values of f_{max} between 6.3 and 10. As in the case of linear polymer melts, f_{max} is able to reveal differences in the strain-hardening behaviour.

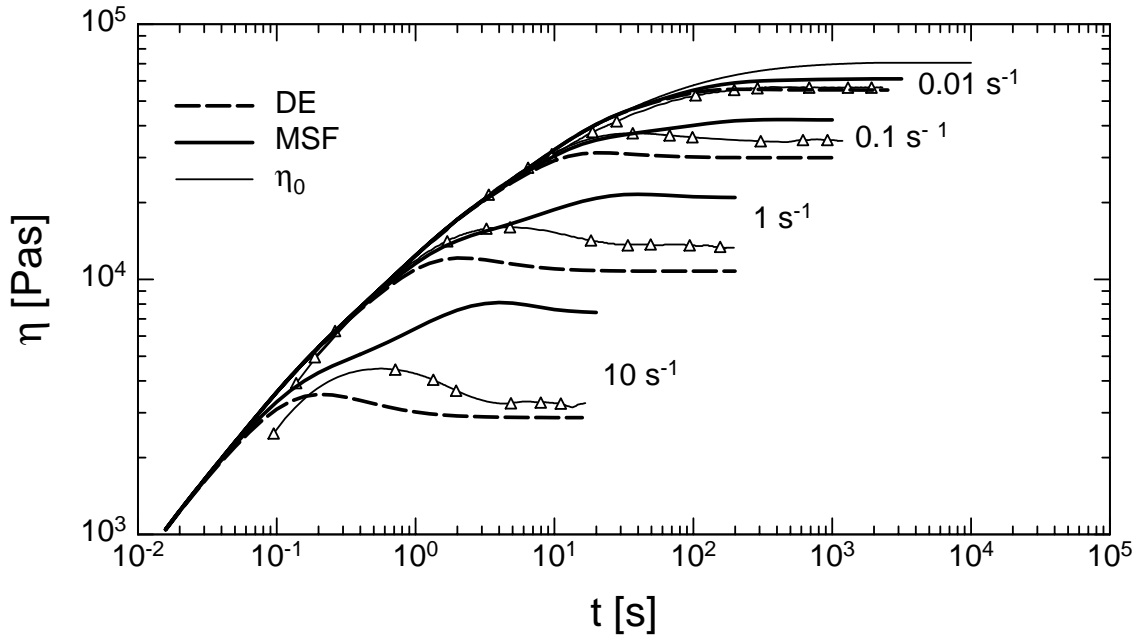


Figure 5.18: Shear viscosity η of melt LDPE I at a temperature of $T = 150\text{ }^\circ\text{C}$, with $f_{max}^2 = 100$ (Eq. (5.20)), determined from extensional data.

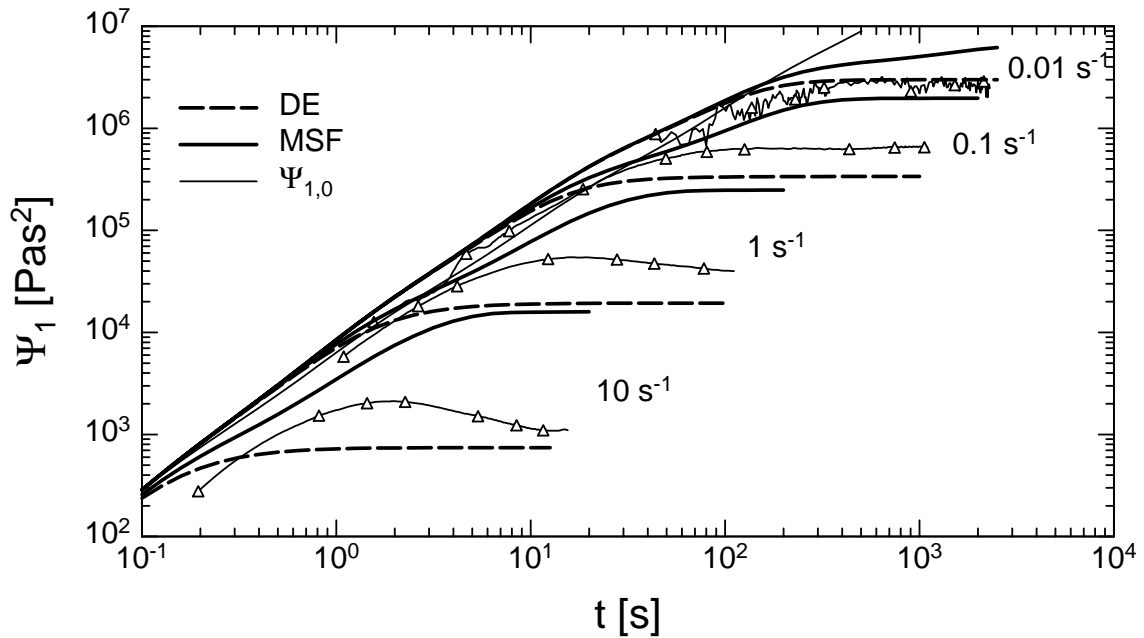


Figure 5.19: First normal stress coefficient Ψ_1 of LDPE I melt at a temperature of $T = 150\text{ }^\circ\text{C}$, with $f_{max}^2 = 100$ (Eq. (5.20)), determined from extensional data.

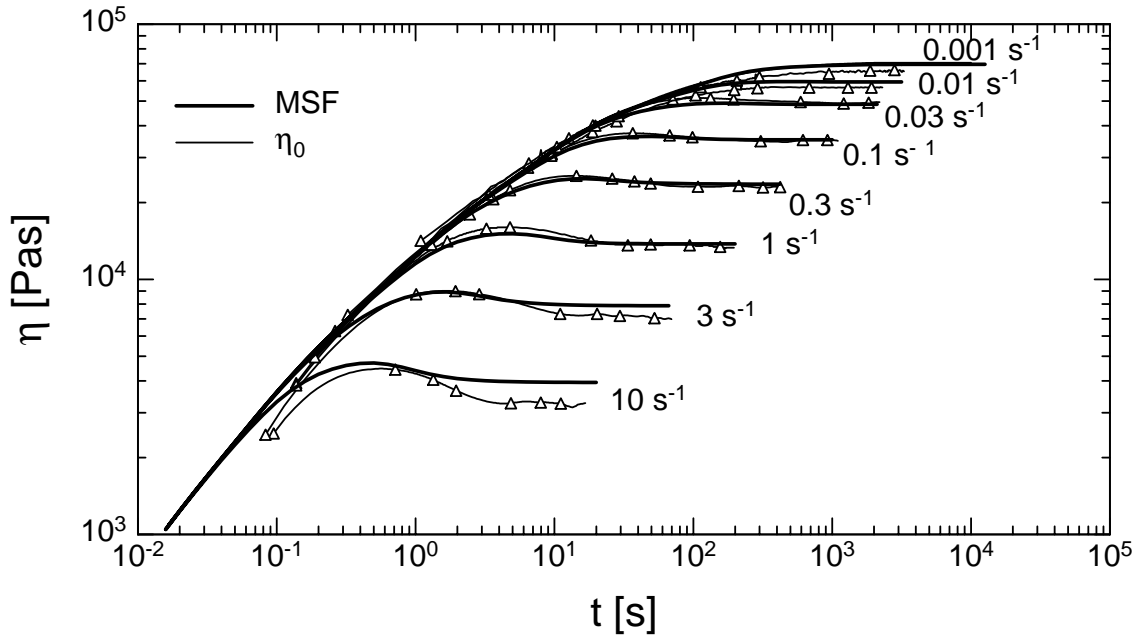


Figure 5.20: Shear viscosity η of melt LDPE I at a temperature of $T = 150\text{ }^\circ\text{C}$, with $f_{max}^2 = 3$ (Eq. (5.20)).

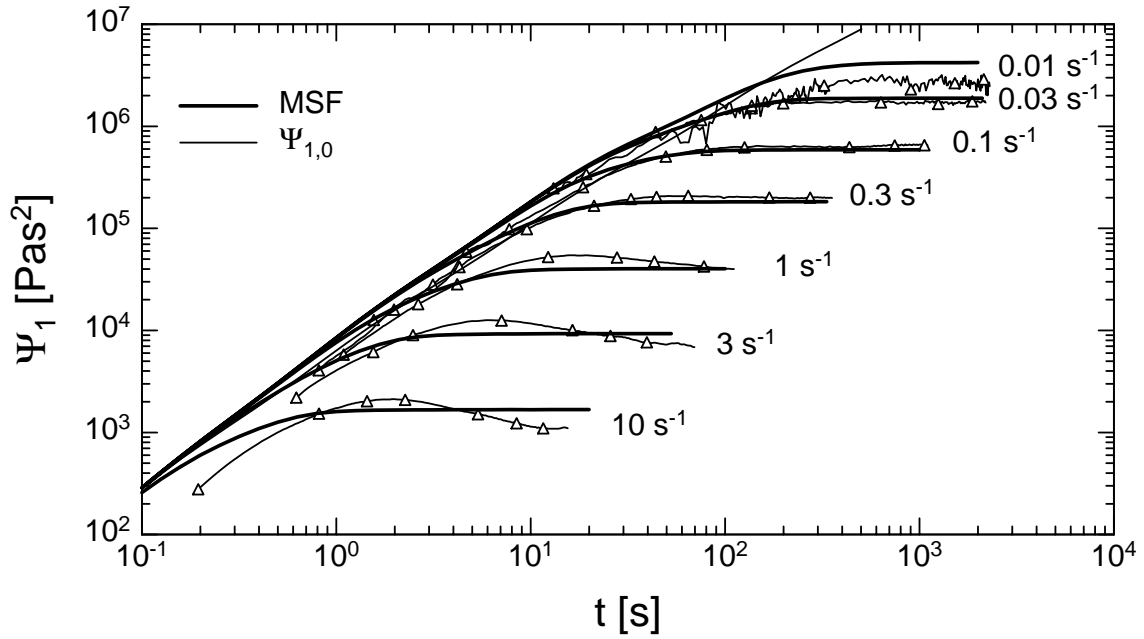


Figure 5.21: First normal stress coefficient Ψ_1 of melt LDPE I at a temperature of $T = 150\text{ }^\circ\text{C}$, with $f_{max}^2 = 3$ (Eq. (5.20)).

The shear flow rheology of melt LDPE I in start-up flow tests was performed by Kraft (1996) [27] at a temperature of 150 °C. Figs. 5.18 and 5.20 show the shear viscosity $\eta(\dot{\gamma}, t)$ (Eq. (2.29)) of melt LDPE I for shear-rates $\dot{\gamma}$ between 0.001 and 10 s^{-1} . All curves pass through a maximum before reaching steady-state. In figs. 5.19 and 5.21, the corresponding first normal stress function $\Psi_1(\dot{\gamma}, t)$ (Eq. (2.30)) is presented for shear-rates $\dot{\gamma}$ between 0.01 and 10 s^{-1} . All $\Psi_1(\dot{\gamma}, t)$ curves form a common envelope at small deformations, presented by the linear-viscoelastic function $\Psi_{1,0}(t)$, which was calculated from the spectrum of relaxation times (Eq. (2.57)).

The predictions of the non-linear strain measure \underline{S}_{MSF} of the MSF model (Eq. (5.20)), which was found to describe all extensional modes consistently with $f_{max}^2 = 100$, is compared to the experimental data (figs. 5.18 and 5.19). Again, $\eta(\dot{\gamma}, t)$ and $\Psi_1(\dot{\gamma}, t)$ are clearly overpredicted for all shear-rates by the molecular stress function determined from the uniaxial experiment. The overprediction increases with increasing shear-rate. But $\eta(\dot{\gamma}, t)$ and $\Psi_1(\dot{\gamma}, t)$ are also underpredicted by the non-linear strain measure \underline{S}_{DE}^{IA} of the Doi-Edwards (DE) theory (Eq. (2.106)), as shown in figs. 5.18 and 5.19.

Choosing a smaller value for the maximum molecular stress function, e.g. $f_{max}^2 = 3$ which corresponds to a maximum stretch of $f_{max} = 1.73$, a surprisingly good agreement between theory and experiment is found for all shear-rates of $\eta(\dot{\gamma}, t)$ (fig. 5.20) and $\Psi_1(\dot{\gamma}, t)$ (fig. 5.21). The shear viscosity $\eta(\dot{\gamma}, t)$ is predicted nearly quantitatively including the maximum of $\eta(t)$ before reaching steady-state, and also the predictions for $\Psi_1(\dot{\gamma}, t)$ at least up to a shear-rate of $\dot{\gamma} = 0.3 s^{-1}$ are extremely well. At higher shear-rates the maximum of $\Psi_1(\dot{\gamma}, t)$ is not predicted.

Though extensional (irrotational) flow can be described consistently by the MSF model and just **one** non-linear material parameter, the chain stretching in shear (rotational) flow seems to be substantially smaller than in extensional flows.

5.2.2 PP II

In fig. 5.22 the uniaxial or elongational viscosity (μ_u) of the polypropylene (PP II) melt is shown together with the threefold zero-shear viscosity $\eta_0(t)$. The measurements were performed by Kurzbeck (1999) [29] at a temperature of 180 °C and strain-rates $\dot{\epsilon}_0$ between 0.002 and 2.0 s^{-1} by use of the MTR. The melt PP II shows extreme strain-hardening, which can be predicted quantitatively by the QMSF model with f^2 according to Eq. (5.16) up to the maximum strains investigated. No saturation effect can be seen for the elongational viscosity. Two experiments with Hencky strains up to $\epsilon_H = 4$ indicate that the viscosity might reach steady-state values at much higher strains. Indeed, creep tests confirmed that a steady-state viscosity exists at viscosities greater than $2 * 10^6$ Pas [29].

By use of the linear-viscoelastic relaxation spectrum (chapt. 4.2.2), the uniaxial (h_u) damping function was calculated from the elongational viscosity. h_u is compared to

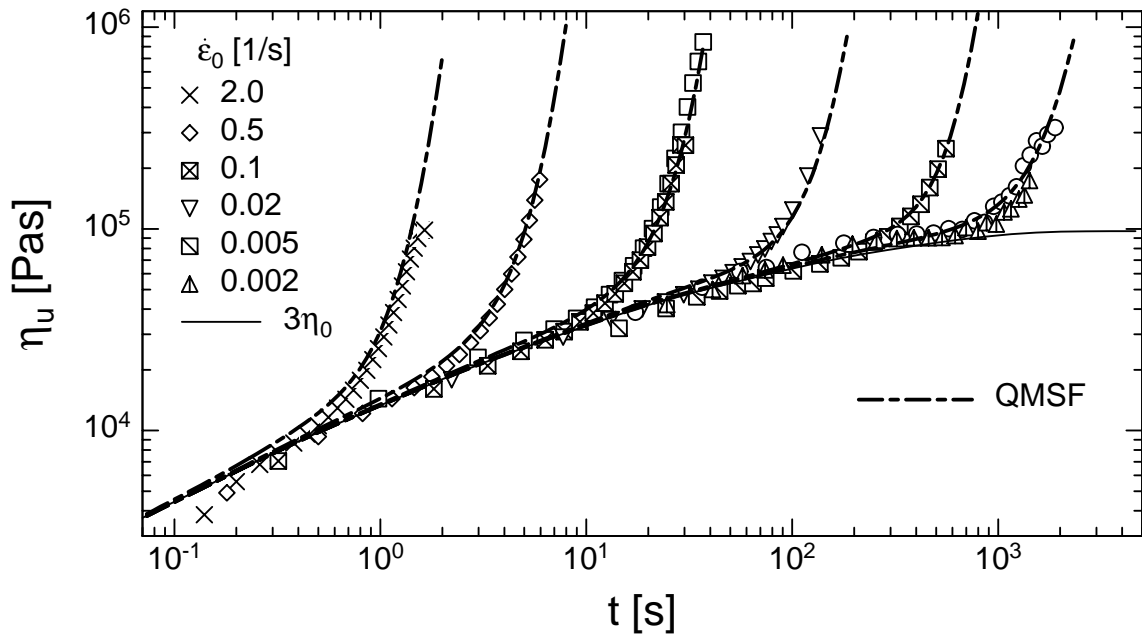


Figure 5.22: Elongational viscosity η_u of melt PP II at a temperature of $T = 180 \text{ }^\circ\text{C}$.

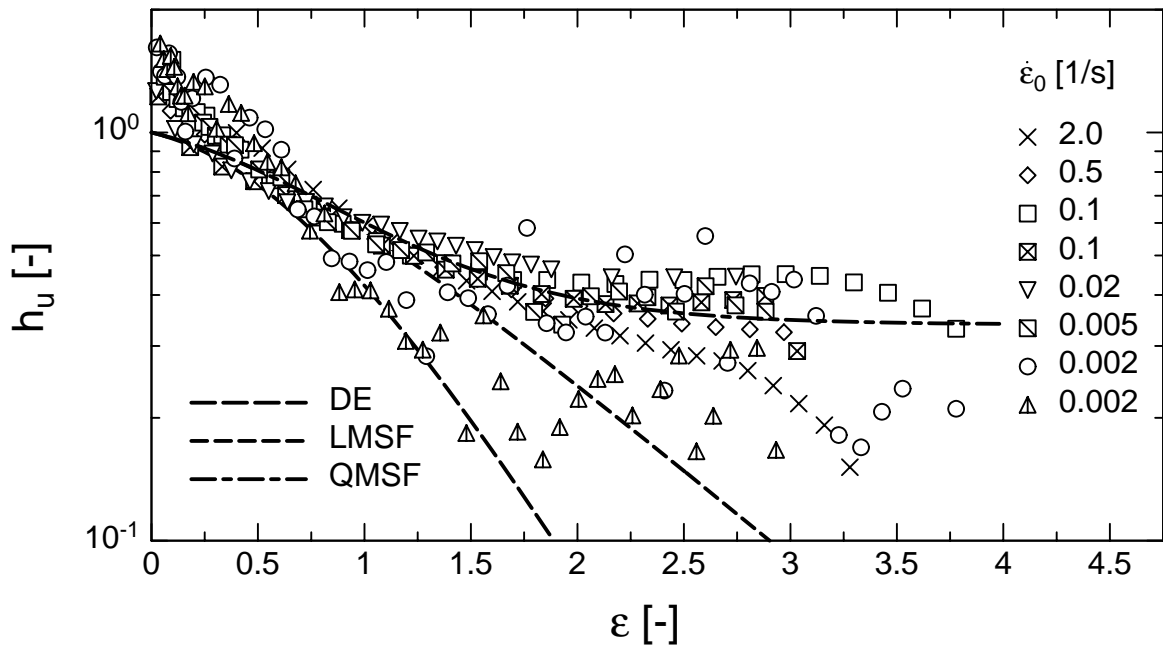


Figure 5.23: Damping function h_u of melt PP II calculated from elongational viscosity.

the predictions of the non-linear strain measure of the DE theory, the LMSF model of Eq. (5.3) and the QMSF model of Eq. (5.16) (fig. 5.23). Whilst the DE theory clearly underpredicts h_u , the LMSF model seems to give a good description up to a Hencky strain of $\varepsilon_H = 1$, neglecting the scatter at small Hencky strains due to experimental difficulties. At larger strains, the experimental data seems to reach a plateau value, which is well described by the QMSF model.

5.3 Consequences for further developments of the MSF theory

The extensional viscosities of the linear and long-chain branched melts investigated are clearly underpredicted by the Doi-Edwards (DE) theory, i.e. the DE model cannot describe strain-hardening behaviour, and is only responsible for the effects of chain orientation. Therefore, strain-hardening can be defined [80] as viscosity upturn above the DE prediction in contrast to the usual definition as upturn above the zero-shear viscosity η_0 [32]. Strain-hardening is quantified in terms of chain stretching, and thus not only long-chain-branched, but also linear polymer melts exhibit strain-hardening for all extensional modes. Macromolecular chains are both orientated and stretched by extensional deformations. In the MSF model, chain stretching is explained by a reduction of the tube diameter with increasing deformation.

The LMSF theory describes the strain-dependence of the viscosity upturn for linear polymer melts with an exponential dependence of the molecular stress function f on the stretch $\langle \ln(u') \rangle_0$. Long-chain branched melts show a more severe upturn of the extensional viscosities with increasing deformation which can be quantified by the QMSF model with a quadratic dependence on $\langle \ln(u') \rangle_0$, derived from the junction fluctuation theory of Flory [22].

Hence, with both zero-parameter models, either LMSF or QMSF depending on the topology of the melt, a quantitative description of the viscosity upturn is possible up to saturation of the extensional viscosities. Hence, the MSF theory can be used to identify the branching structure of polymer melts.

With increasing deformation, the slip between the macromolecular chains and the stretch field L/L_0 increases up to total slip when a maximum value f_{max} of the molecular stress function f or a minimum tube diameter is reached. The maximum value of strain-hardening is governed by f_{max} , the only non-linear material parameter needed to describe the saturation effect in extensional (irrotational) flow, which is directly related to the strain-hardening effect. A large value of f_{max} is responsible for enhanced strain-hardening, a small value of f_{max} for a small amount of strain-hardening. If $f_{max} = 1$, then the DE theory is recovered. For linear polymer melts, f_{max} was found to be between $1.3 \leq f_{max} \leq 5.5$, and for branched polymer melts between $6.3 \leq f_{max} \leq 10$ (including the polymer melts considered in the appendix). f_{max} seems to depend on

the molecular weight distribution and branching topology. If f_{max} is estimated from an uniaxial extension experiment, performed with a commercial elongational rheometer, the steady-state viscosities can be predicted for all extensional deformation modes.

However, shear (rotational) flow of both polyethylene melts, linear (HDPE I) and branched (LDPE I), cannot be described by the non-linear material parameter f_{max} estimated from the respective uniaxial viscosity experiment. Smaller values of f_{max} were found describing the shear flow rheology. For melt HDPE I, $f_{max} \approx 1$ in contrast to $f_{max} = 5.5$ from extension gives a good prediction of the shear flow rheology. Therefore, as f is close to unity, the shear flow of melt HDPE I can be described in good approximation by the DE theory (IA approximation). For melt LDPE I, shear flow rheology is predicted adequately by $f_{max} = 1.73$ instead of $f_{max} = 10$ derived from extension.

In summary, the constitutive equation of the MSF theory with the non-linear strain measure of the LMSF (Eq. (5.9)) or QMSF (Eq. (5.20)) model, is not able to describe extensional and shear flows consistently with just **one** non-linear material parameter f_{max} . The molecular stress function theory for polymer melts has to be extended to find a consistent description for both irrotational and rotational flows.

6 Extended MSF theory including dissipative constraint release

6.1 The free energy of the MSF model

Considering the strain energy function of strain-dependent tube stretch models, the stretch evolution equation has to be written as a function of $\langle \ln(u') \rangle_0$ [82], [80]. This can be shown by deriving the free energy of the MSF theory [64].

The entropic free energy w_{LMSF} of a linear entangled chain segment confined to a tube with strain-dependent tube diameter a is given by [10], [37]

$$\frac{w_{LMSF}}{3kT} = \frac{N_e b^2}{a^2} - 1 = \frac{a_0^2}{a^2} - 1 = f^2 - 1 \quad (6.1)$$

where use has been made of the definition of f (Eq. (2.126)). The linear entangled chain segment consists of a large number $N_e = a_0^2/b^2$ of monomers between entanglements.

In contrast, the free energy w_{DE} of the DE theory is only due to the entropy reduction caused by the orientation of rigid tube segments [40],

$$\frac{w_{DE}}{3kT} = \langle \ln(u') \rangle_0 \quad (6.2)$$

After a step deformation, the stress tensor $\underline{\underline{\sigma}}$ is given by

$$\underline{\underline{\sigma}} = \frac{1}{5} G_N^0 f^2 \underline{\underline{S}}_{DE}^{IA} = G_N^0 f^2 \underline{\underline{S}} \quad (6.3)$$

and the time change of the free energy w_{LMSF} is governed at segmental level by $\partial f^2 / \partial t$,

$$\frac{1}{3kT} \frac{\partial w_{LMSF}}{\partial t} = \frac{\partial f^2}{\partial t} = \underline{\underline{\kappa}} : \frac{\underline{\underline{\sigma}}}{G_N^0} \quad (6.4)$$

which is related to the power of the stress tensor $\underline{\underline{\sigma}}$ and therefore the rate of doing work according to the principle of virtual work [32]. In Eq. (6.4), dissipation is neglected, and it is assumed that all mechanical work done by the stress tensor is stored by tube deformation. This is called the "limiting elastic case". In the terminology of Öttinger [55], [56], this corresponds to the regime of "reversible thermodynamics".

Replacing $\underline{\underline{\sigma}}$ in Eq. (6.4) by Eq. (6.3), the evolution equation of the molecular stress function f is then found to be

$$\frac{\partial f^2}{\partial t} = (\underline{\underline{\kappa}} : \underline{\underline{S}}) f^2 \quad (6.5)$$

Integration of Eq. (6.5) with the respect to time t leads to

$$\ln f^2 = \int_0^t (\underline{\kappa} : \underline{S}) dt' \quad (6.6)$$

Considering the same virtual work argument for the free energy w_{DE} of the DE theory, the following expression is obtained from Eq. (6.2) [80]

$$\frac{\partial \langle \ln(u') \rangle_0}{\partial t} = \underline{\kappa} : \underline{S} \quad (6.7)$$

From Eqs. (6.6) and (6.7), $\ln f^2$ is found to be equal to the average logarithmic stretch $\langle \ln(u') \rangle_0$. This shows that indeed the MSF theory involves a dependence of f on $\langle \ln(u') \rangle_0$ of the form

$$f^2 = e^{\langle \ln(u') \rangle_0} \quad (6.8)$$

For small deformations, the free energy w_{LMSF} is equal to the one calculated from the DE theory (IA),

$$\frac{w_{LMSF}}{3kT} |_{\gamma \rightarrow 0} = e^{\langle \ln(u') \rangle_0} |_{\gamma \rightarrow 0} - 1 \approx \langle \ln(u') \rangle_0 = \frac{w_{DE}}{3kT} \quad (6.9)$$

which demonstrates that the orientation process, described by the DE theory (IA), is the dominant entropic effect at start-up of flows. This fact can explicitly be expressed in Eq. (6.1) by separating the effects of orientation and chain stretch,

$$\frac{w_{LMSF}}{3kT} = \langle \ln(u') \rangle_0 + f^2 - \ln f^2 - 1 \quad (6.10)$$

where use has been made of Eq. (6.8). The orientational part of the free energy, $\langle \ln(u') \rangle_0$, is identical to the free energy of the DE theory (IAA), while the part due to chain stretch has the desired properties, i.e. a minimum at equilibrium ($f^2 = 1$), a quadratic dependence on f^2 in the vicinity of equilibrium, and a divergence at $f^2 = 0$.

So far, the limiting elastic case was considered, i.e. it was assumed that the polymeric system exhibits ideal elasticity, and that the work of the stress tensor $\underline{\underline{\sigma}}$ is totally stored by tube deformation. Assuming now more generally that part of the work of $\underline{\underline{\sigma}}$ will be dissipated, then this dissipation process has to be considered in the energy balance which describes the reduction of the tube diameter. An extra term, simply denoted by "CR", is introduced on the left-hand side of Eq. (6.4) which leads to

$$\frac{1}{3kT} \frac{\partial w_{LMSF}}{\partial t} + CR = \underline{\kappa} : \frac{\underline{\underline{\sigma}}}{G_N^0} \quad (6.11)$$

In the terminology of Öttinger [55], [56], Eq. (6.11) is an expression of "irreversible thermodynamics". As before, the first term on the left-hand side is given by $\partial f^2 / \partial t$ and expresses the energy stored per unit time. By using here Eq. (6.10) instead of Eq. (6.1),

orientation is assumed to be reversible, i.e. orientation has an energy potential, while chain stretch has no potential. The overall power in terms of the stress tensor of Eq. (6.3) is expressed on the right-hand side of Eq. (6.11). This leads to a more general evolution equation of f for linear polymer melts,

$$\frac{\partial f^2}{\partial t} = f^2 \left[(\underline{\underline{\kappa}} : \underline{\underline{S}}) - \frac{CR}{f^2 - 1} \right] \quad (6.12)$$

where CR is a dissipative term, caused by "Constraint Release". The idea of "Constraint Release" was first introduced by Marrucci (1996) [38] and Mead et al. (1998) [42]. For small deformations, the solution of Eq. (6.12) reduces again to Eq. (6.8), as "Constraint Release" can be neglected in this case.

Since the relaxation of the chain occurs mainly by reptation, the Helmholtz free energy W_{LMSF} per unit volume is derived for any arbitrary strain-history by a time-superposition of contributions from c/N_e tube segments which leads to

$$W_{LMSF}(t) = G_N^0 \int_{-\infty}^t \frac{\partial P_t(t-t')}{\partial t'} (\langle \ln(u') \rangle_0 + f^2 - \ln f^2 - 1) dt' \quad (6.13)$$

with the survival probability $P_t(t-t')$ of a tube segment, and the plateau modulus G_N^0 .

The evolution equation Eq. (6.12) was derived considering the free energy of a tube segment of linear entangled chains for which $N_e b^2 = a_0^2$ is valid at equilibrium. However, in the previous chapter it was shown that the LMSF theory cannot describe the onset of the extensional viscosity of long-chain branched polymer melts. Hence, for branched melts the parameter β with $0 < \beta \leq 1$ is introduced [64],

$$N_e b^2 = \beta a_0^2 \quad (6.14)$$

which allows to distinguish between the equilibrium tube diameter a_0 of a polymer made up of linear chains ($\beta = 1$), and βa_0^2 for a branched environment. β is seen as the influence of the effective free energy potential, which is created by the topology of long-chain branching, on the molecular dynamics of the melt.

At small deformations, the free energy of a branched melt must also be dominated by the orientation process of the tube segments (Eq. (6.9)). This can be achieved by assuming the following empirical form of the segmental free energy,

$$\frac{w_{MSF}}{3kT} = \beta(f^2 - 1) + (1 - \beta)\langle \ln(u') \rangle_0 \quad (6.15)$$

which is a linear combination of the entropic elastic free energy w_{LMSF} and the orientational free energy w_{DE} of a segment. From the principal of virtual work (Eq. (6.2)),

a general evolution equation for the molecular stress function f can be derived for any general topology of melts in the limiting elastic case,

$$\beta \frac{\partial f^2}{\partial t} + (1 - \beta)(\underline{\underline{\kappa}} : \underline{\underline{S}}) = (\underline{\underline{\kappa}} : \underline{\underline{S}}) f^2 \quad (6.16)$$

by use of Eqs. (6.4), (6.5), and (6.7).

The general expression of the molecular stress function for any topology of polymer melts in the limiting elastic case can be obtained from Eq. (6.16) by integration,

$$f^2 = \beta e^{\frac{1}{\beta} \langle \ln(u') \rangle_0} + (1 - \beta) \quad (6.17)$$

where dissipation by constraint release has been neglected. For $\beta = 1$, Eq. (6.17) reduces again to Eq. (6.8) which is valid only for linear melts. For long-chain-branched melts, a value of $\beta = 1/2$ has been found to describe the onset of extensional and shear viscosities consistently (chapt. 5.2).

Following the same argument as used in Eq. (6.10) above, the tube deformation process is assumed to involve a dissipative process CR , where by use of Eqs. (6.15) and (6.17), the free energy is expressed again as the sum of the free energies of orientation and chain stretch,

$$\frac{w_{MSF}}{3kT} = \langle \ln(u') \rangle_0 + \beta \left\{ f^2 - \beta \ln \left[\frac{1}{\beta} (f^2 - 1) + 1 \right] - 1 \right\} \quad (6.18)$$

This leads, for $0 < \beta \leq 1$, to an evolution equation for the molecular stress function f of the general form

$$\frac{\partial f^2}{\partial t} = \left[\frac{1}{\beta} (f^2 - 1) + 1 \right] \left[(\underline{\underline{\kappa}} : \underline{\underline{S}}) - \frac{CR}{f^2 - 1} \right] \quad (6.19)$$

where CR is again denoted as a "Constraint Release" mechanism which acts on the tube segment scale, independently of the melt topology, and which represents a dissipative term.

The Helmholtz free energy per unit volume W_{MSF} for any arbitrary strain-history is obtained by time-superposition of contributions from c/N_e tube segments within the material according to

$$W_{MSF}(t) = G_N^0 \int_{-\infty}^t \frac{\partial P_t(t-t')}{\partial t'} \left[\langle \ln(u') \rangle_0 + \beta \left\{ f^2 - \beta \ln \left[\frac{1}{\beta} (f^2 - 1) + 1 \right] - 1 \right\} \right] dt' \quad (6.20)$$

6.2 Kinematics of tube deformation and constraint release

To understand constraint release (*CR*) processes in tube deformation, first the kinematics of tube deformation are considered with the intent to describe the convection mechanisms for tube orientation and tube cross-section. For this purpose, the time derivative of the relative deformation gradient tensor $\underline{\underline{F}}_t$ (Eq. (2.9)) is recalled (chapt. 2.1.2),

$$\frac{\partial \underline{\underline{F}}_t}{\partial t} = -\underline{\underline{F}}_t \cdot \underline{\underline{\kappa}} = -\underline{\underline{\kappa}}^T \cdot \underline{\underline{F}}_t^T \quad (6.21)$$

and the time derivative of the relative inverse deformation gradient $\underline{\underline{F}}_t^{-1}$ (Eq. (2.10)),

$$\frac{\partial \underline{\underline{F}}_t^{-1}}{\partial t} = \underline{\underline{\kappa}} \cdot \underline{\underline{F}}_t^{-1} \quad (6.22)$$

which can be calculated by use of the velocity gradient tensor $\underline{\underline{\kappa}}$.

A unit vector $\underline{p}(t)$ is now considered which is tangential to a tube segment at any time t , and is given by the deformed unit vector \underline{u}' (Eq. (2.86)), normalised by its length u' ,

$$\underline{p}(t) = \frac{\underline{u}'}{u'} \quad (6.23)$$

This corresponds to the DE theory with the IA assumption: Eq. (6.23) describes that the tube segments rotate affinely with the macroscopic strain, and if the continuum deforms at constant volume, the second order orientation tensor $\underline{\underline{S}}$ (Eq. (2.106)) can be expressed as a function of $\underline{p}(t)$ and of the orientational distribution function $\psi(\underline{p}, t) = \psi(\Theta, \varphi, t)$ [15] by

$$\underline{\underline{S}} = \left\langle \frac{\underline{u}'\underline{u}'}{u'^2} \right\rangle_0 = \langle \underline{p}\underline{p} \rangle = \oint \psi(\underline{p}, t) \underline{p}\underline{p} \sin\Theta d\Theta d\varphi \quad (6.24)$$

While on the left-hand side of Eq. (6.24), the integration is over an isotropic distribution of unit vectors at the past time t' , the integration on the right-hand side is performed over the distribution function at time t .

The time rate-of-change of \underline{u}' is given by

$$\frac{\partial \underline{u}'}{\partial t} = \underline{\underline{\kappa}} \cdot \underline{u}' \quad (6.25)$$

according to Eq. (6.22). Normalised by the length u' of the vector \underline{u}' , the result is the affine time change of the vector $\underline{p}(t)$ due to convection,

$$\frac{1}{u'} \frac{\partial \underline{u}'}{\partial t} = \underline{\underline{\kappa}} \cdot \underline{p}(t) = \underline{\bar{p}}(t) \quad (6.26)$$

denoted by $\underline{\bar{p}}$ in the following.

The advantage of introducing the vector $\underline{p}(t)$ is that the scalar $(\underline{\kappa} : \underline{S})$, which corresponds to the average tangential velocity of tube segments assuming affine convection, can be expressed as the average of the projection of $\underline{\bar{p}}$ on the orientation vector \underline{p}

$$\underline{\kappa} : \underline{S} = \langle \underline{\kappa} : \underline{p} \underline{p} \rangle = \langle \underline{\kappa} \cdot \underline{p} \cdot \underline{p} \rangle = \langle \underline{\bar{p}} \cdot \underline{p} \rangle \quad (6.27)$$

According to the MSF theory, affine convection is correlated to the tube diameter reduction process. If $\underline{q}(t)$ is defined as a unit vector normal to the tube cross-section at any time t ,

$$\underline{q}(t) = \underline{p}(t) \quad (6.28)$$

then $\langle \underline{\bar{q}} \cdot \underline{q} \rangle$ is the average rate-of-change of the tube cross-section under affine convection conditions. $\underline{\bar{q}}$ is the affine time derivative of the normal vector \underline{q} , and is given by

$$\underline{\bar{q}}(t) = -\underline{\kappa}^T \cdot \underline{q} = \frac{1}{n'} \frac{\partial \underline{n}'}{\partial t} \quad (6.29)$$

where the affinely deformed surface vector \underline{n}' is introduced,

$$\underline{n}' = \underline{F}_t^T \cdot \underline{n} = \underline{n} \cdot \underline{F}_t \quad (6.30)$$

and use has been made of Eq. (6.21).

If A is the relative average tube cross-sectional area at time t ,

$$A = \frac{a^2}{a_0^2} = \frac{1}{f^2} \quad (6.31)$$

then the time derivative of A is given by

$$\frac{\partial A}{\partial t} = \langle \underline{\bar{q}} \cdot \underline{q} \rangle A \quad (6.32)$$

From Eqs. (6.31) and (6.32), the following evolution equation for the molecular stress function f^2 can be derived,

$$\frac{\partial f^2}{\partial t} = -\langle \underline{\bar{q}} \cdot \underline{q} \rangle f^2 = (\underline{\kappa} : \underline{S}) f^2 \quad (6.33)$$

by use of the relation

$$\langle \underline{\bar{q}} \cdot \underline{q} \rangle = -\underline{\kappa} : \underline{S} \quad (6.34)$$

If constraint release is neglected, and linear melts ($\beta = 1$) are considered, the MSF evolution equation (6.19) reduces to Eq. (6.33). The form of the molecular stress function can thus be explained as a consequence of the decrease of the relative tube cross-sectional area A . However, at large deformations the limiting elastic case is no longer valid for the tube deformation process, as shown in chapter 5.1. The deviation

from the affine convection process can be described by the more general evolution equation [64],

$$\frac{\partial A}{\partial t} = \langle \underline{\bar{q}} \cdot \underline{q} \rangle A + g[\underline{q}, \underline{\bar{q}}, \underline{\bar{p}}] (1 - A) \quad (6.35)$$

$g[\underline{q}, \underline{\bar{q}}, \underline{\bar{p}}]$ is a scalar function of the normal vector \underline{q} and the kinematic vectors $\underline{\bar{q}}$ and $\underline{\bar{p}}$, and is associated with the constraint release process. The term $(1 - A)$ ensures that the relative tube cross-sectional area is equal to one at equilibrium. Incorporating Eqs. (6.31) and (6.34) into Eq. (6.35), the evolution equation for the molecular stress function is given by

$$\frac{\partial f^2}{\partial t} = f^2 \left[(\underline{\kappa} : \underline{\underline{S}}) - (f^2 - 1) g[\underline{q}, \underline{\bar{q}}, \underline{\bar{p}}] \right] \quad (6.36)$$

Comparing this evolution equation with Eq. (6.19) for linear melts ($\beta = 1$), the dissipative constraint release term CR must be written as

$$CR = (f^2 - 1)^2 g[\underline{q}, \underline{\bar{q}}, \underline{\bar{p}}] \quad (6.37)$$

The quantity $(f^2 - 1)^2$ arises from geometrical aspects of tube deformation according to the MSF theory and ensures that the tube has a diameter a_0 at equilibrium. Hence, further work with the intend to model the dissipative constraint release process by tube convection will only concern the function $g[\underline{q}, \underline{\bar{q}}, \underline{\bar{p}}]$.

In order to obtain some guidance on how to model the function $g[\underline{q}, \underline{\bar{q}}, \underline{\bar{p}}]$, the evolution equation Eq. (5.8) for the LMSF model with maximum molecular stress f_{max} is considered first. If the exponential term in Eq. (5.8) is replaced by f^2 , this leads to the following evolution equation:

$$\frac{\partial f^2}{\partial t} = (\underline{\kappa} : \underline{\underline{S}}) f^2 - f^2 (f^2 - 1) \frac{1}{f_{max}^2 - 1} (\underline{\kappa} : \underline{\underline{S}}) \quad (6.38)$$

From Eq. (6.38) follows that the CR term includes a function $g[\underline{q}, \underline{\bar{q}}, \underline{\bar{p}}]$ of the form

$$g[\underline{q}, \underline{\bar{q}}, \underline{\bar{p}}] = -\frac{1}{f_{max}^2 - 1} \langle \underline{\bar{q}} \cdot \underline{q} \rangle \quad (6.39)$$

where use has been made of Eq. (6.34). The numerical pre-factor is associated with the maximum of segmental stored energy, $f = f_{max}$. The convection term $\langle \underline{\bar{q}} \cdot \underline{q} \rangle$ describes the time change of the cross-sectional area projected onto the orientation of the tube. The function $g[\underline{q}, \underline{\bar{q}}, \underline{\bar{p}}]$ can thus be interpreted as being proportional to a loss-rate of constraints in the tube direction. Such a convection mechanism allows to model the tube deformation in extensional flows of linear melts, but is inadequate for shear flow (chapter 5.1).

On the evidence, a constraint release model or more precisely a function $g[\underline{q}, \underline{\bar{q}}, \underline{\bar{p}}]$ is needed, representing a dissipative constraint release process which is substantially

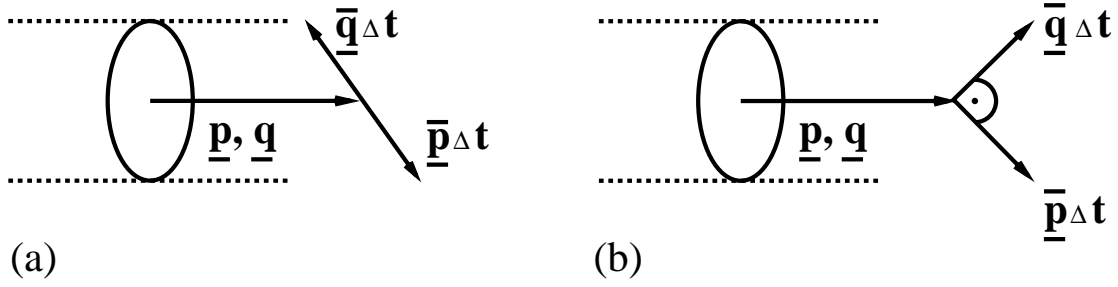


Figure 6.1: Schematic representation of the affine rates-of-change of the tube segment orientation vector \underline{p} and of the cross-sectional surface vector \underline{q} , in the case of extensional flows (a) and simple shear flow (b).

different for shear flow and for extensional flows. Since the model must include the results previously described, $g[\underline{q}, \underline{\bar{q}}, \underline{\bar{p}}]$ must essentially be governed by a convection mechanism along the tube direction, and must be a function of the first order of the absolute strain-rate in order to introduce irreversibility of constraint release.

Tube deformation is subject to basic kinematic differences in terms of the affine rates-of-change in tube orientation and in tube cross-sectional area (fig. 6.1) [64]: $\underline{\bar{q}}$ is **always** coaxial to $\underline{\bar{p}}$ in extensional flows (where the velocity gradient tensor $\underline{\kappa}$ is diagonal, i.e. $\underline{\kappa}^T = \underline{\kappa} = \underline{D}$), whereas $\underline{\bar{q}}$ is **always** perpendicular to $\underline{\bar{p}}$ in simple shear flow,

$$\underline{\bar{p}} \cdot \underline{\bar{q}} = -\underline{\kappa} \cdot \underline{p} \cdot \underline{\kappa}^T \cdot \underline{p} = -\underline{\kappa} \cdot \underline{\kappa} : \underline{p} \underline{p} = 0 \quad (6.40)$$

because each component of the second order tensor $\underline{\kappa} \cdot \underline{\kappa}$ is zero in simple shear flow.

It is therefore assumed that the difference of the rate-of-change of the tube cross-sectional area, $\underline{\bar{q}}$, and the rate-of-change of tube segment orientation, $\underline{\bar{p}}$, is the origin of dissipative constraint release. Restricting attention to constant strain-rate flows, two scalar differences can be constructed from $\underline{\bar{q}}$ and $\underline{\bar{p}}$, which are quadratic in deformation rate,

$$\frac{1}{4}(\underline{\bar{q}} - \underline{\bar{p}})^2 = \frac{1}{4}(\underline{\kappa}^T \cdot \underline{p} + \underline{\kappa} \cdot \underline{p})^2 = \underline{D}^2 : \underline{p} \underline{p} \quad (6.41)$$

and

$$\frac{1}{4}(\underline{\bar{q}} \cdot \underline{\bar{q}} - \underline{\bar{p}} \cdot \underline{\bar{p}}) = \frac{1}{4}(\underline{\bar{q}} + \underline{\bar{p}}) \cdot (\underline{\bar{q}} - \underline{\bar{p}}) = -\underline{W} \cdot \underline{p} \cdot \underline{D} \cdot \underline{p} = \underline{W} \cdot \underline{D} : \underline{p} \underline{p} \quad (6.42)$$

with the rate-of-deformation tensor, \underline{D} , and the rate-of-rotation tensor, \underline{W} (chapt. 2.1.2).

Having thus established two kinematic second-order differences of $\underline{\bar{q}}$ and $\underline{\bar{p}}$, one depending only on the deformation rate, and one depending on the deformation rate and rate-of-rotation, it is assumed that dissipative constraint release is substantially different for rotational and irrotational flows. Two constraint release functions $g_1[\underline{q}, \underline{\bar{q}}, \underline{\bar{p}}]$

and $g_2[\underline{q}, \underline{\bar{q}}, \underline{\bar{p}}]$ can then be introduced

$$g_1[\underline{q}, \underline{\bar{q}}, \underline{\bar{p}}] = \frac{1}{2} \sqrt{\langle (\underline{\bar{q}} - \underline{\bar{p}})^2 \rangle} = \sqrt{\underline{\underline{D}}^2 : \underline{\underline{S}}} \quad (6.43)$$

and

$$g_2[\underline{q}, \underline{\bar{q}}, \underline{\bar{p}}] = \frac{1}{2} \sqrt{\langle (\underline{\bar{q}} \cdot \underline{\bar{q}} - \underline{\bar{p}} \cdot \underline{\bar{p}}) \rangle} = \sqrt{|\underline{\underline{W}} \cdot \underline{\underline{D}} : \underline{\underline{S}}|} \quad (6.44)$$

which are of first order in the absolute value of the strain-rate. The simplest way to express the constraint release function $g[\underline{q}, \underline{\bar{q}}, \underline{\bar{p}}]$ is a linear combination of $g_1[\underline{q}, \underline{\bar{q}}, \underline{\bar{p}}]$ and $g_2[\underline{q}, \underline{\bar{q}}, \underline{\bar{p}}]$,

$$g[\underline{q}, \underline{\bar{q}}, \underline{\bar{p}}] = a_1 g_1[\underline{q}, \underline{\bar{q}}, \underline{\bar{p}}] + a_2 g_2[\underline{q}, \underline{\bar{q}}, \underline{\bar{p}}] \quad (6.45)$$

with the non-linear material parameters $a_1 \geq 0$ and $a_2 \geq 0$.

Introducing Eq. (6.45) into Eq. (6.37), rotational and irrotational flows can clearly be distinguished by the dissipative term CR as the functions $g_1[\underline{q}, \underline{\bar{q}}, \underline{\bar{p}}]$ and $g_2[\underline{q}, \underline{\bar{q}}, \underline{\bar{p}}]$ have different expressions depending on flow kinematics. In simple shear flow with a constant shear-rate $\dot{\gamma}$,

$$g_1[\underline{q}, \underline{\bar{q}}, \underline{\bar{p}}] = \frac{\dot{\gamma}}{2} \sqrt{S_{11} + S_{22}} \quad (6.46)$$

and

$$g_2[\underline{q}, \underline{\bar{q}}, \underline{\bar{p}}] = \frac{\dot{\gamma}}{2} \sqrt{|S_{11} - S_{22}|} \quad (6.47)$$

while in extensional flows

$$g_1[\underline{q}, \underline{\bar{q}}, \underline{\bar{p}}] = \sqrt{\underline{\underline{D}}^2 : \underline{\underline{S}}} = \dot{\epsilon} \sqrt{S_{11} + m^2 S_{22} + (1 + m)^2 S_{33}} \quad (6.48)$$

and

$$g_2[\underline{q}, \underline{\bar{q}}, \underline{\bar{p}}] = 0 \quad (6.49)$$

where $\dot{\epsilon}$ is the largest strain-rate, and the parameter m as defined in chapter 2.1.4.

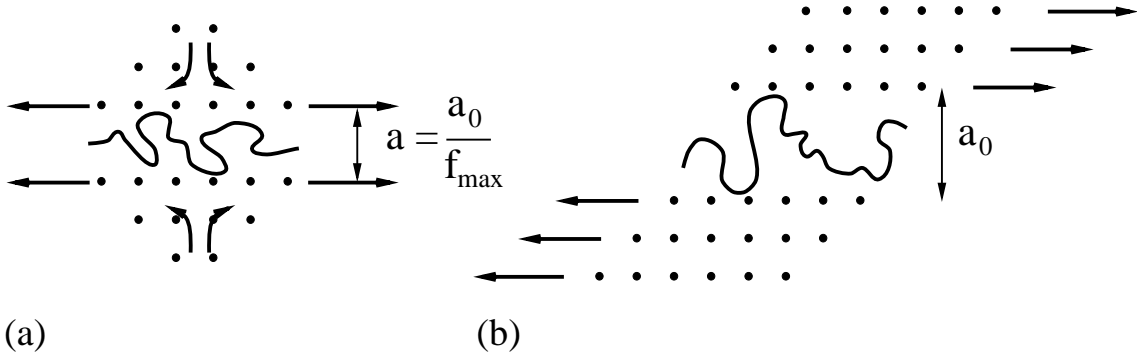


Figure 6.2: Constraint release processes, in the case of extensional flows (a) and simple shear flow (b).

At large deformations, constraint release in extensional flows occurs mainly in the stretching direction, and thus balances the squeeze due to the advection of neighbouring topological constraints (fig. 6.2a). This leads to the assumption previously made in

the MSF theory, namely a minimum tube diameter and a maximum molecular stress function f_{max} . In contrast, in simple shear flow the affine change of tube segment length due to convection tends to zero, while the affine change of tube cross-sectional area continues with the consequence that the tube diameter returns to its equilibrium value a_0 (fig. 6.2b).

To summarise, for linear melts and constant strain-rate flows, the evolution equation (Eq. (6.36)) for the molecular stress function is given by

$$\frac{\partial f^2}{\partial t} = f^2 \left[(\underline{\kappa} : \underline{S}) - a_1(f^2 - 1)\sqrt{\underline{D}^2 : \underline{S}} + a_2(f^2 - 1)\sqrt{|\underline{W} \cdot \underline{D} : \underline{S}|} \right] \quad (6.50)$$

For long-chain-branched melts with $\beta = 1/2$, the corresponding evolution Eq. (6.19) is given by

$$\frac{\partial f^2}{\partial t} = (2f^2 - 1) \left[(\underline{\kappa} : \underline{S}) - a_1(f^2 - 1)\sqrt{\underline{D}^2 : \underline{S}} + a_2(f^2 - 1)\sqrt{|\underline{W} \cdot \underline{D} : \underline{S}|} \right] \quad (6.51)$$

Hence, the extended MSF model involves only two non-linear material parameters, namely a_1 and a_2 , both of which govern the dissipative term in simple shear flow, while dissipation in extensional flows (being irrotational) depends on a_1 only.

The extended MSF model is no longer of the K-BKZ type, although it is strain-dependent. In contrast to the predictions of the K-BKZ model, polymer melts exhibit a different strain dependence for simple shear and planar ("pure shear") flow in the MSF model with stretch evolution equations (Eqs. (6.50), (6.51)), which was also experimentally observed for a polyethylene melt [26]. Material characterisations are necessary both in one extensional flow experiment, preferably an elongational experiment, and in shear flow in order to determine the relevant non-linear material parameters a_1 and a_2 . With the non-linear material parameter a_1 , determined from the elongational experiment, again excellent predictions for all biaxial extensional flows are possible.

The dissipative constraint release function $g[\underline{q}, \underline{\bar{q}}, \underline{\bar{p}}]$ can be expressed in a frame indifferent form for general flows. This is most easily demonstrated by expressing $g_1[\underline{q}, \underline{\bar{q}}, \underline{\bar{p}}]$ and $g_2[\underline{q}, \underline{\bar{q}}, \underline{\bar{p}}]$ as functions of the second-order Rivlin-Erickson tensors $\underline{A}_1^2 = 4\underline{D}^2$ and $\underline{A}_2 = \frac{\partial \underline{A}_1}{\partial t} + \underline{A}_1^2 + 2(\underline{W} \cdot \underline{D} + \underline{D} \cdot \underline{W}^T)$ [6], [32],

$$g_1[\underline{q}, \underline{\bar{q}}, \underline{\bar{p}}] = \frac{1}{2}\sqrt{\underline{A}_1^2 : \underline{S}} \quad (6.52)$$

and

$$g_2[\underline{q}, \underline{\bar{q}}, \underline{\bar{p}}] = \frac{1}{2}\sqrt{|\underline{A}_2 : \underline{S} - \underline{A}_1^2 : \underline{S}|} \quad (6.53)$$

which, for constant strain-rate flows, is identical to Eqs. (6.48) and (6.49).

6.3 Comparison to extensional and shear data of linear polymer melts

As shown before, the MSF theory in extensional flows is correlated with a maximum of storable elastic energy, and accordingly a maximum value of the molecular stress function f_{max} . The evolution equation of the molecular stress function for linear melts in extensional flows is derived from Eq. (6.50) together with Eqs. (6.48) and (6.49),

$$\frac{\partial f^2}{\partial t} = \dot{\epsilon} f^2 \left[S_{11} + m S_{22} - (1 + m) S_{33} - a_1 (f^2 - 1) \sqrt{S_{11} + m^2 S_{22} - (1 + m)^2 S_{33}} \right] \quad (6.54)$$

At large deformations, a maximum f_{max}^2 of the molecular stress function is reached, and $\partial f^2 / \partial t = 0$. The parameter a_1 can thus be expressed as a function of f_{max}^2 ,

$$a_1 = \frac{1}{f_{max}^2 - 1} \quad (6.55)$$

With $f_{max}^2 = 49$ instead of $f_{max}^2 = 30$, as found for Eq. (5.9), a consistent description of all extensional viscosities of melt HDPE I ([23]) is possible (fig. 6.3-6.6). A larger value of f_{max}^2 was chosen because our measurements showed that linear polymer melts might break even at lower strains and accordingly smaller stresses due to inhomogeneity, and consequently the achievable maximum Hencky strains are smaller than for long-chain-branched melts. Since the extensional viscosities of melt HDPE I are rather underpredicted by Eq. (5.9) with $f_{max}^2 = 30$, it is reasonable to increase the maximum of the molecular stress function to $f_{max}^2 = 49$ for melt HDPE I. The predictions of in particular the first planar viscosity are improved. For the same reasons as discussed in chapter 5.1, μ_u , μ_e , and μ_{p1} are slightly underpredicted at low strain-rates, and slightly overestimated at high strain-rates. However, the difference of predictions using Eq. (6.54) as compared to predictions of Eq. (5.9) is not very pronounced for irrotational flows. The uniaxial elongational viscosity at $\dot{\epsilon} = 1$ 1/s is recalculated by use of Eq. (5.9) with $f_{max}^2 = 49$ instead of $f_{max}^2 = 30$, and shown as a dashed line in fig. 6.3. The onset of the elongational viscosity is nearly identical up to a Hencky strain of $\epsilon_H = 3.5$, then a small deviation is observed, but both curves come together again at the same steady-state value, governed by the maximum molecular stress function, $f_{max}^2 = 49$. Hence, both MSF models (Eqs. (5.9) and (6.54)) allow an excellent, consistent description of irrotational flows.

New measurements of the shear viscosity $\eta(\dot{\gamma}, t)$ and of the first normal stress coefficient $\Psi_1(\dot{\gamma}, t)$ (denoted by IKT) in the non-linear range at 170 °C are shown together with the measurements of Kraft [27]. Experiments were performed using the cone-and-plate geometry of the rheometer RMS800 (chap. 3.2) to ensure that experimental uncertainties can be excluded for the new model. The measurements are in good agreement with the results of Kraft, and confirm the experimental error of Kraft at a shear-rate of $\dot{\gamma} = 3$ 1/s for the shear viscosity $\eta(\dot{\gamma}, t)$.

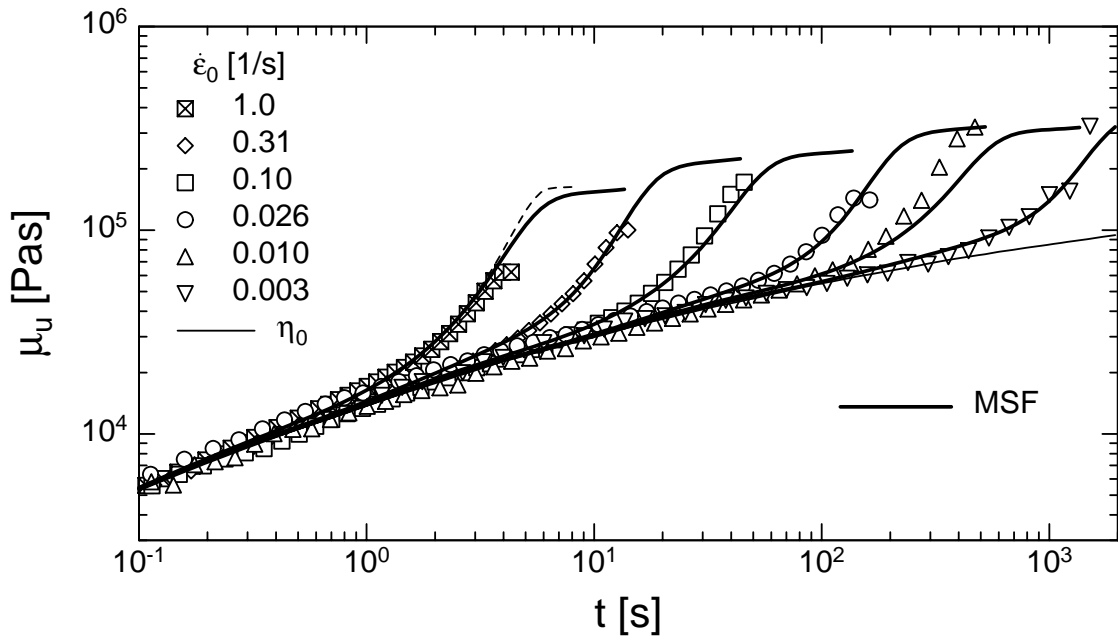


Figure 6.3: Elongational viscosity μ_u of melt HDPE I at a temperature of $T = 150\text{ }^\circ\text{C}$, with $f_{max}^2 = 49$ (Eq. (6.54)). (Dashed line is prediction of Eq. (5.9) with $f_{max}^2 = 49$.)

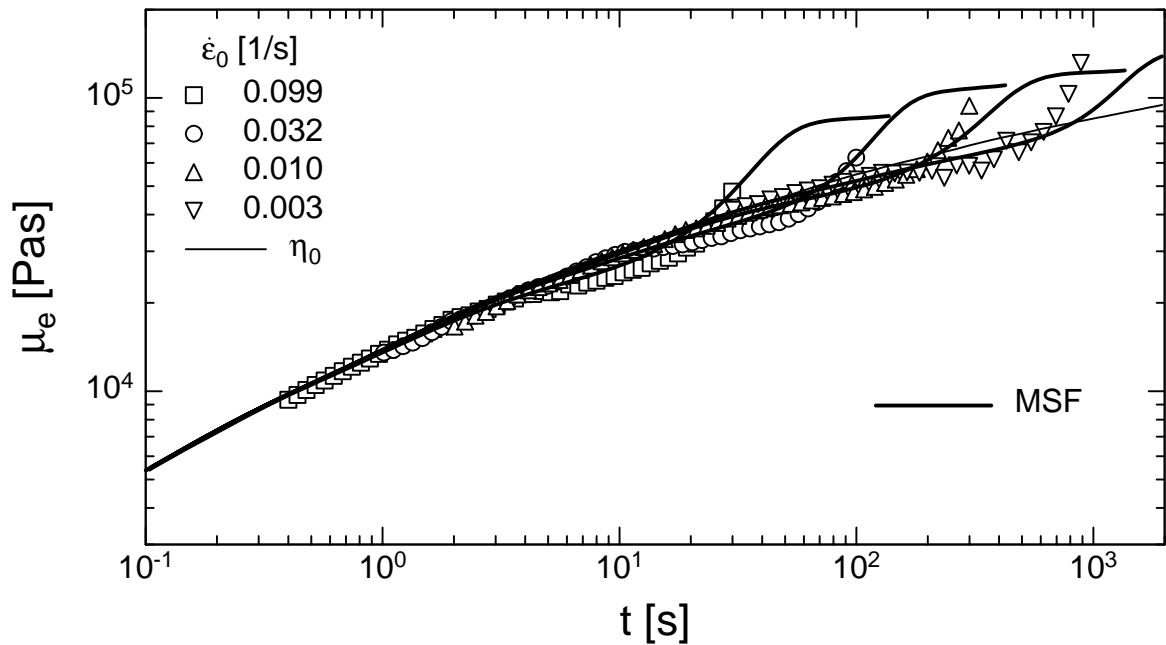


Figure 6.4: Equibiaxial viscosity μ_e of melt HDPE I at a temperature of $T = 150\text{ }^\circ\text{C}$, with $f_{max}^2 = 49$ (Eq. (6.54)).

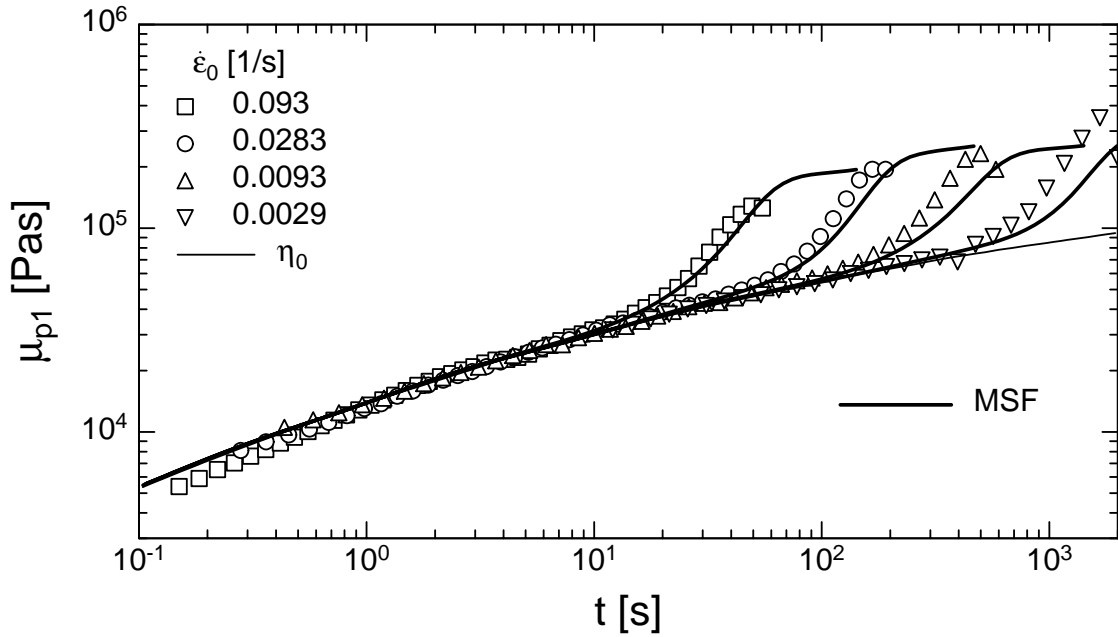


Figure 6.5: First planar viscosity μ_{p1} of melt HDPE I at a temperature of $T = 150 \text{ }^\circ\text{C}$, with $f_{max}^2 = 49$ (Eq. (6.54)).

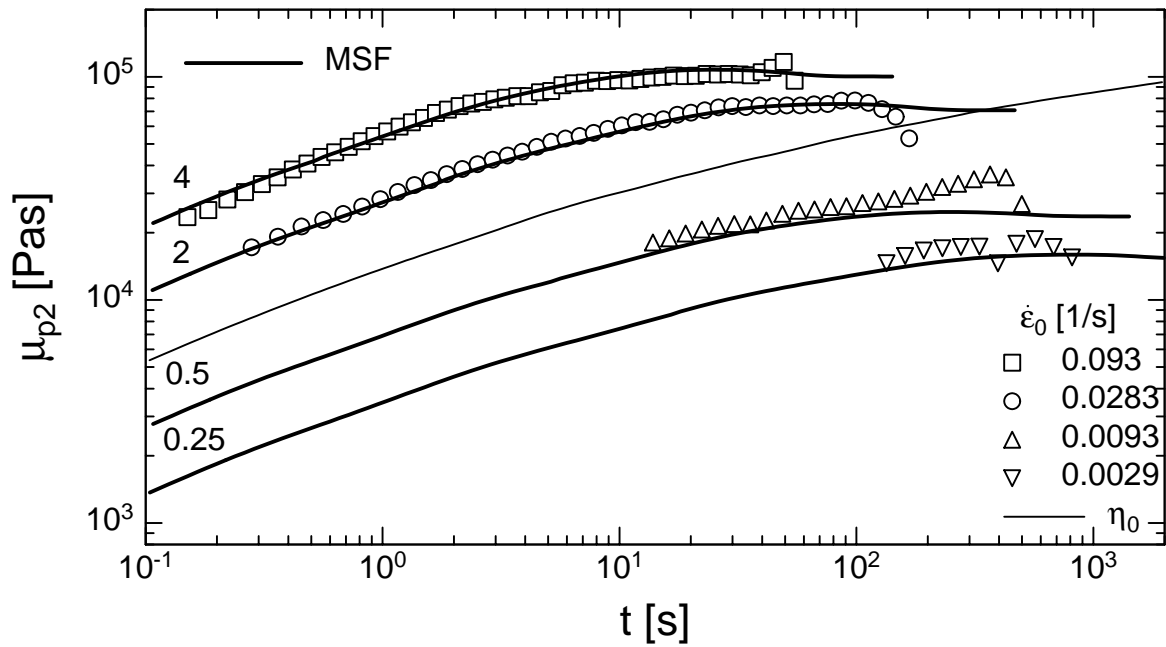


Figure 6.6: Second planar viscosity μ_{p2} of melt HDPE I at a temperature of $T = 150 \text{ }^\circ\text{C}$, with $f_{max}^2 = 49$ (Eq. (6.54)).

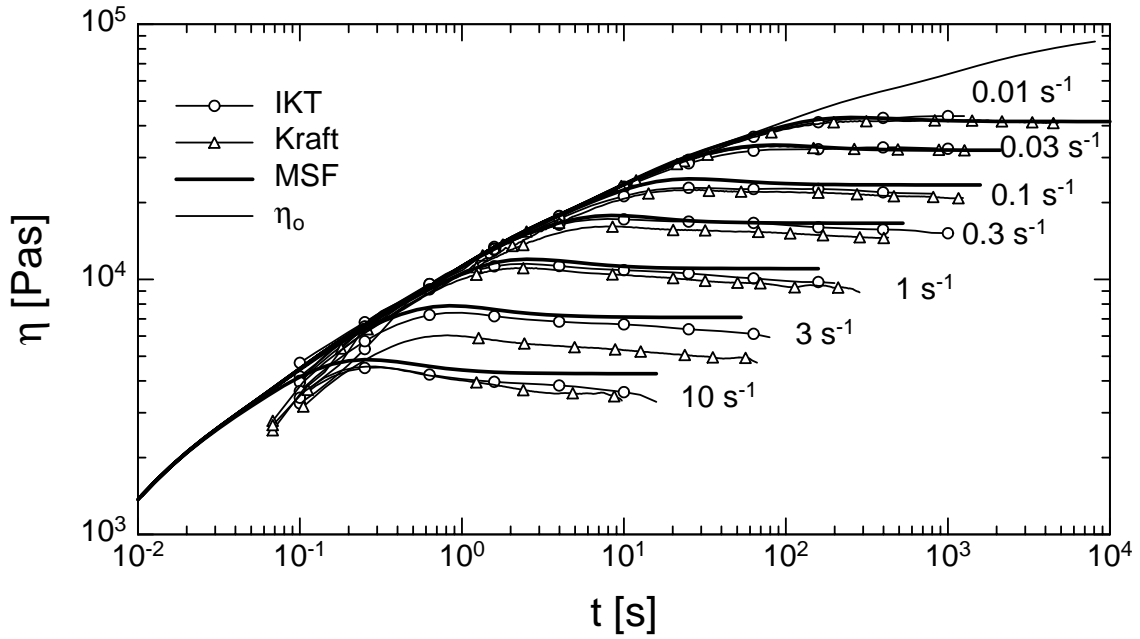


Figure 6.7: Shear viscosity η of melt HDPE I at a temperature of $T = 170\text{ }^{\circ}\text{C}$, with $a_1 = 0.02$ (corresponding to $f_{max}^2 = 49$) and $a_2 = 2.3$ (Eq. (6.56)).

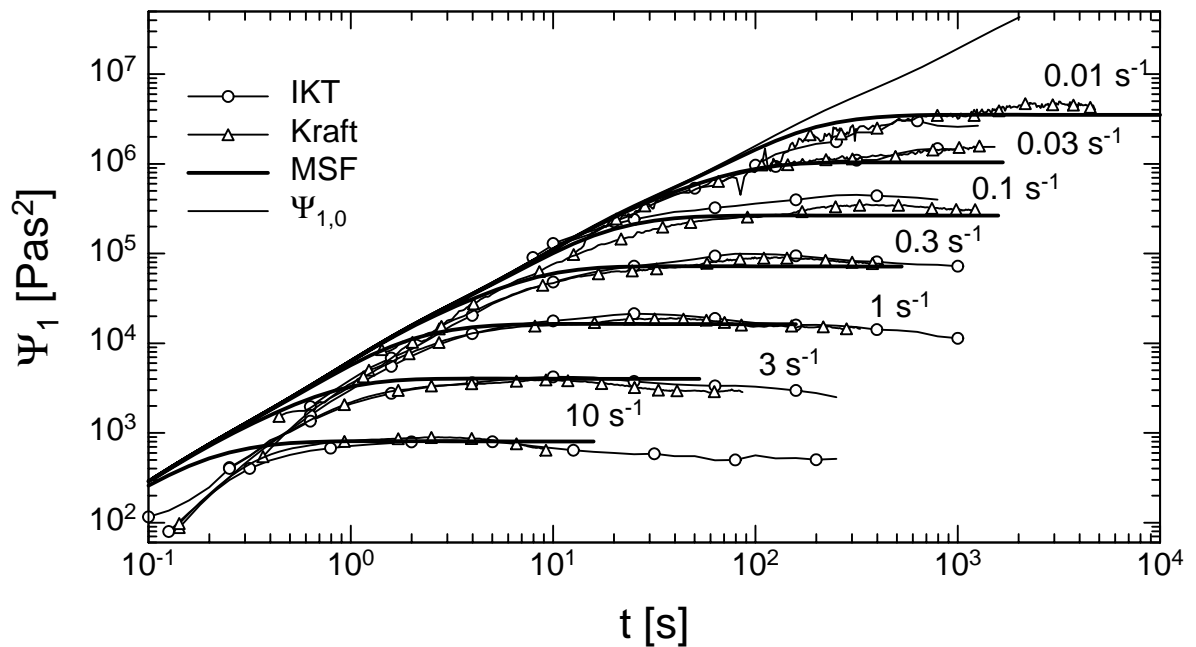


Figure 6.8: First normal stress coefficient Ψ_1 of melt HDPE I at a temperature of $T = 170\text{ }^{\circ}\text{C}$, with $a_1 = 0.02$ and $a_2 = 2.3$ (Eq. (6.56)).

The evolution equation of the molecular stress function for linear melts in shear flow is derived from Eq. (6.50) with Eqs. (6.46) and (6.47),

$$\frac{\partial f^2}{\partial t} = \dot{\gamma} f^2 \left[S_{12} - \frac{a_1}{2} (f^2 - 1) \sqrt{S_{11} + S_{22}} - \frac{a_2}{2} (f^2 - 1) \sqrt{|S_{11} - S_{22}|} \right] \quad (6.56)$$

While the value of the material parameter a_1 is determined by extensional flow and is given by Eq. (6.55) with $f_{max}^2 = 49$, shear viscosity $\eta(\dot{\gamma}, t)$ and first normal stress coefficient $\Psi_1(\dot{\gamma}, t)$ of melt HDPE I are modelled by adjusting the second material parameter a_2 , relevant for rotational flows, to a value of $a_2 = 2.3$ (fig. 6.7 and 6.8). Predictions of the overshoot and of the steady-state value of the shear viscosity are in excellent agreement with experimental data. The predictions of $\Psi_1(\dot{\gamma}, t)$ are in general agreement with the experimental data except at small deformations, where due to the limited stiffness of the instrument and radial flow, the experimental normal stress is delayed.

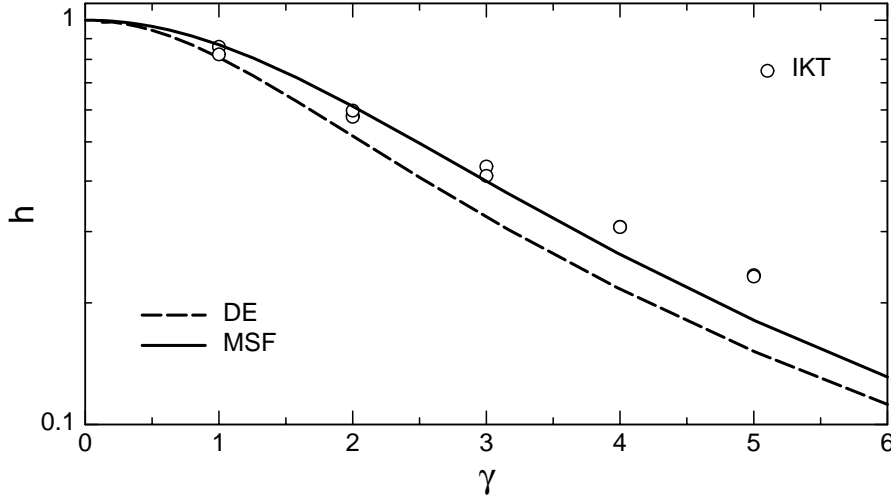


Figure 6.9: Damping function h of melt HDPE I in shear, with $a_1 = 0.02$ and $a_2 = 2.3$ (Eq. (6.57)).

To obtain a damping function for melt HDPE I, the shear relaxation modulus $G(t, \gamma)$ was measured for different step-shear strains up to $\gamma = 5$ with the cone-and-plate geometry of the rheometer RMS800 (chap. 3.2) at a temperature of 210°C . The damping function $h_{MSF}(\gamma)$ of the MSF model is expressed for simple shear flow by

$$h_{MSF}(\gamma) = \frac{f^2(\gamma)}{\gamma} S_{12}(\gamma) \quad (6.57)$$

In Eq. (6.57), $f^2(\gamma)$ is the solution by numerical integration of Eq. (6.56). The same values of the non-linear material parameters, $a_1 = 0.02$ (corresponding to $f_{max}^2 = 49$) and $a_2 = 2.3$, as determined by the start-up experiments in steady shear flow, were used to calculate $h_{MSF}(\gamma)$. The damping function $h_{MSF}(\gamma)$ is in good agreement with the experimentally observed damping function for melt HDPE I up to strains of $\gamma = 3$. At higher strains, the experimental data are higher than the predictions (fig. 6.9). The reason for this is not yet clear.

6.4 Comparison to extensional and shear data of long-chain-branched polymer melts

The evolution equation of the molecular stress function for long-chain-branched melts in extensional flows is derived from Eqs. (6.51) with Eq. (6.48) and (6.49),

$$\frac{\partial f^2}{\partial t} = \dot{\varepsilon}(2f^2 - 1) \left[S_{11} + mS_{22} - (1+m)S_{33} - a_1(f^2 - 1)\sqrt{S_{11} + m^2S_{22} - (1+m)^2S_{33}} \right] \quad (6.58)$$

Following the same arguments as for melt HDPE I, the same relation, Eq. (6.55), between the material parameter a_1 and f_{max}^2 is obtained. With a value of $f_{max}^2 = 100$ as used in the previous MSF model (chapt. 5.2), a consistent description of all extensional viscosities ($\mu_u, \mu_e, \mu_{p1}, \mu_{p2}$) of melt LDPE I (measurements by Hachmann [23]) is possible (fig. 6.10-6.13). Again, the predictions of Eq. (6.58) in irrotational flows are very similar to the predictions of Eq. (5.20). This is demonstrated for the uniaxial elongational viscosity at $\dot{\varepsilon} = 1$ 1/s in fig. 6.10. The onset of the elongational viscosity is nearly identical up to a Hencky strain of $\varepsilon_H = 3$, then a small deviation is observed up to a Hencky strain of $\varepsilon_H = 6$, where both predictions fall together again.

The evolution equation of the molecular stress function for long-chain-branched melts in shear flow is derived from Eq. (6.51) with Eqs. (6.46) and (6.47),

$$\frac{\partial f^2}{\partial t} = \dot{\gamma}(2f^2 - 1) \left[S_{12} - \frac{a_1}{2}(f^2 - 1)\sqrt{S_{11} + S_{22}} - \frac{1}{a_2}\dot{\gamma}(f^2 - 1)\sqrt{|S_{11} - S_{22}|} \right] \quad (6.59)$$

Again, the value of the material parameter a_1 is determined by extensional flows and is given by Eq. (6.55) with $f_{max}^2 = 100$. A value of $a_2 = 0.036$ provides an excellent description of the stress overshoot and steady-state values of both the shear viscosity $\eta(\dot{\gamma}, t)$ (fig. 6.14) and the first normal stress function $\Psi_1(\dot{\gamma}, t)$ (fig. 6.15), measured by Kraft [27] and by our rotational rheometer (denoted by IKT) in the non-linear range at a temperature of 150 °C. The new measurements are in good agreement with the results of Kraft, but with some deviations at higher shear-rates, in particular for the shear viscosity $\eta(\dot{\gamma}, t)$.

The shear relaxation modulus $G(t, \gamma)$ was measured for different step-shear strains up to $\gamma = 10$ with the cone-and-plate geometry of the rheometer RMS800 (chap. 3.2) at a temperature of 190 °C in order to obtain a damping function for melt LDPE I. Comparison of the experimental data to the predictions of Eq. (6.57) is shown in fig. 6.16. Here, $f^2(\gamma)$ in Eq. (6.57) is the solution by numerical integration of Eq. (6.59). The experimentally observed damping function for melt LDPE I is described very well by the non-linear material parameters $a_1 = 0.01$ (corresponding to $f_{max}^2 = 100$) and $a_2 = 0.036$, determined from the start-up flow experiments in shear, up to a step-shear strain of $\gamma = 10$ (fig. 6.16).

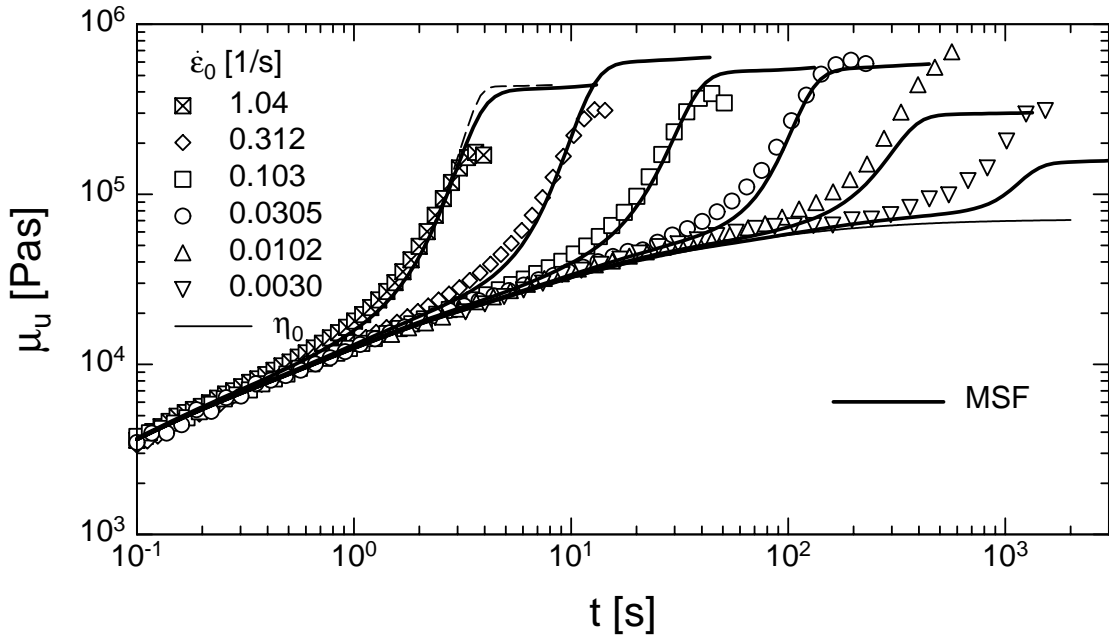


Figure 6.10: Elongational viscosity μ_u of melt LDPE I at a temperature of $T = 150\text{ }^\circ\text{C}$, with $f_{max}^2 = 100$ (Eq. (6.58)). (Dashed line is prediction of Eq. (5.20) with $f_{max}^2 = 100$.)

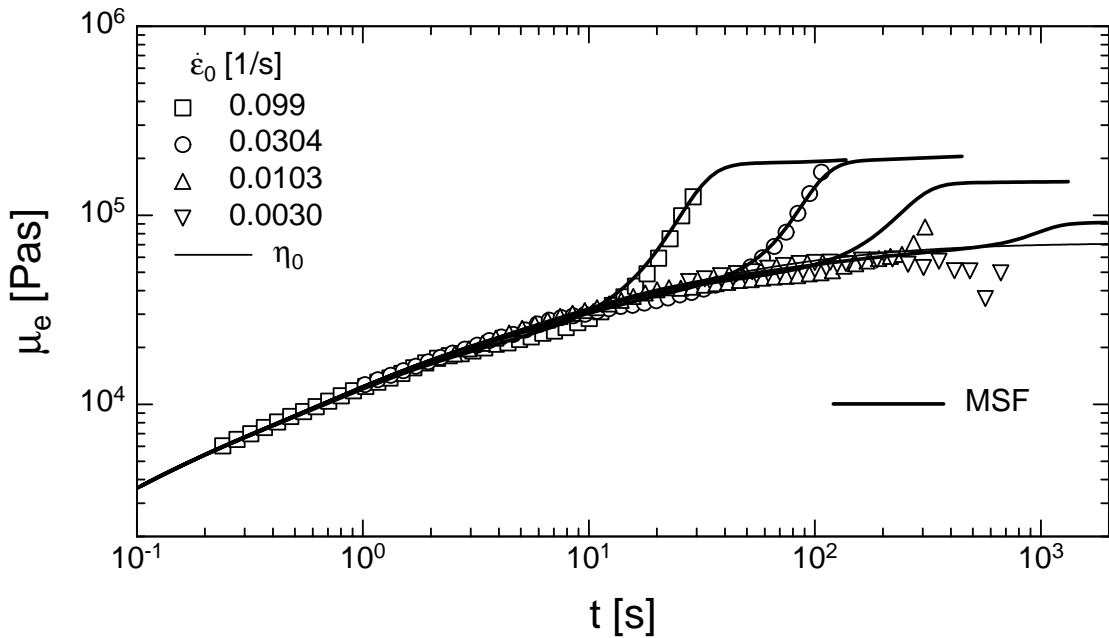


Figure 6.11: Equibiaxial viscosity μ_e of melt LDPE I at a temperature of $T = 150\text{ }^\circ\text{C}$, with $f_{max}^2 = 100$ (Eq. (6.58)).

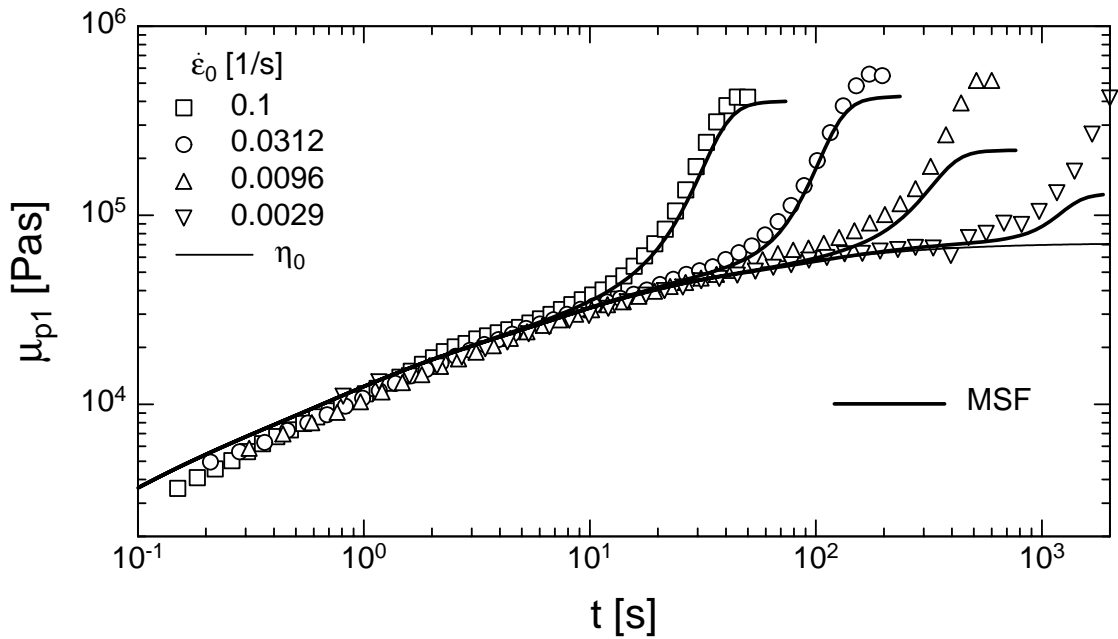


Figure 6.12: First planar viscosity μ_{p1} of melt LDPE I at a temperature of $T = 150\text{ }^\circ\text{C}$, with $f_{max}^2 = 100$ (Eq. (6.58)).

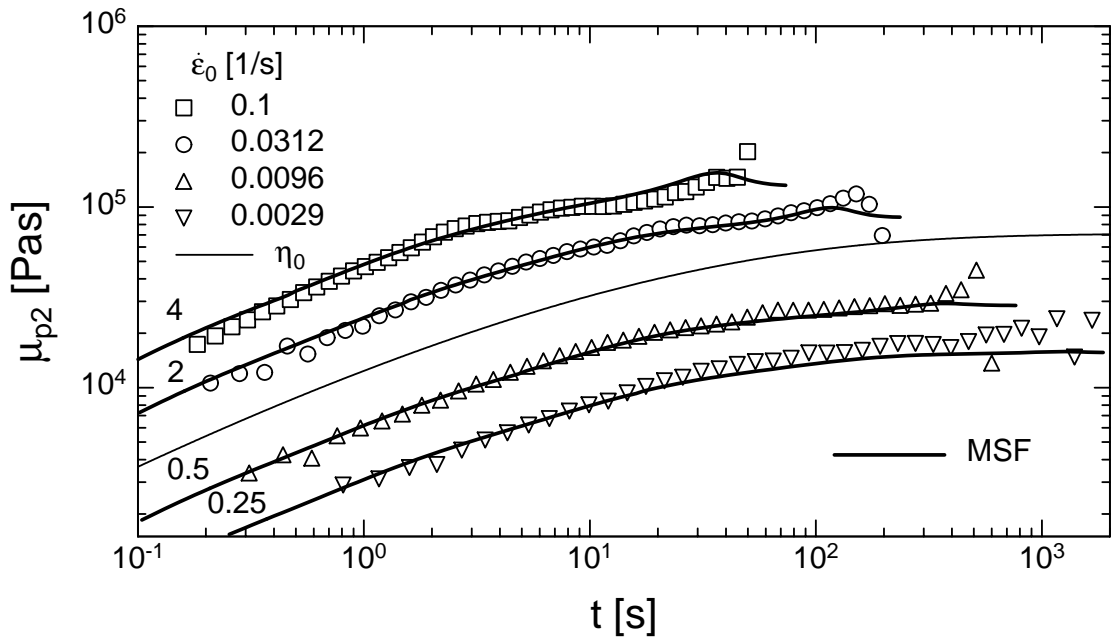


Figure 6.13: Second planar viscosity μ_{p2} of melt LDPE I at a temperature of $T = 150\text{ }^\circ\text{C}$, with $f_{max}^2 = 100$ (Eq. (6.58)).

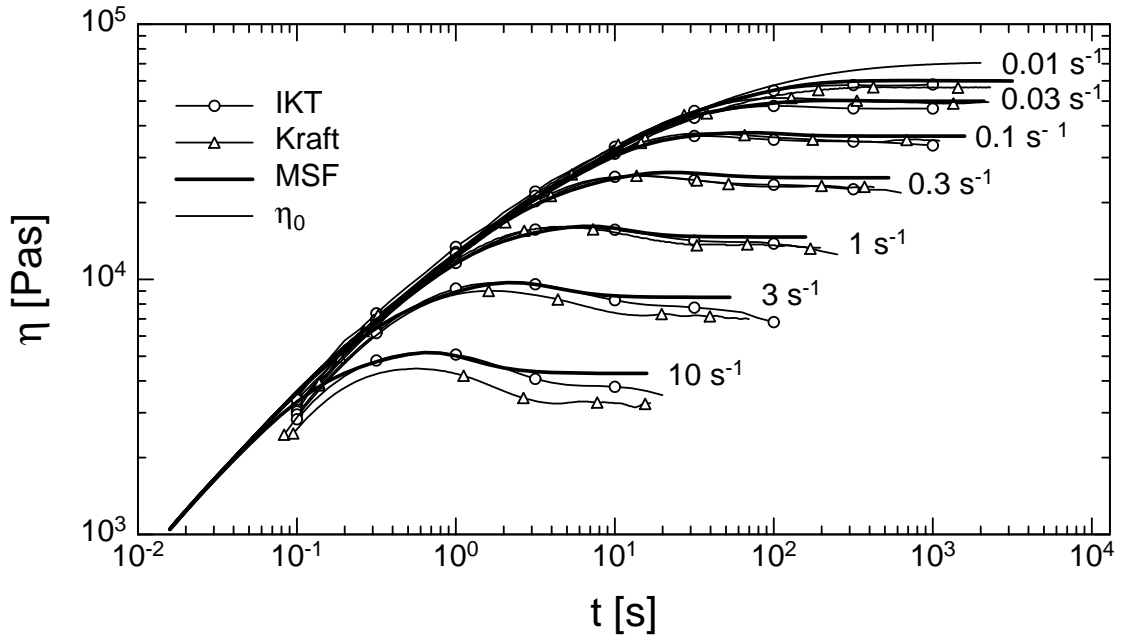


Figure 6.14: Shear viscosity η of melt LDPE I at a temperature of $T = 150\text{ }^\circ\text{C}$, with $a_1 = 0.01$ (corresponding to $f_{max}^2 = 100$) and $a_2 = 0.036$ (Eq. (6.59)).

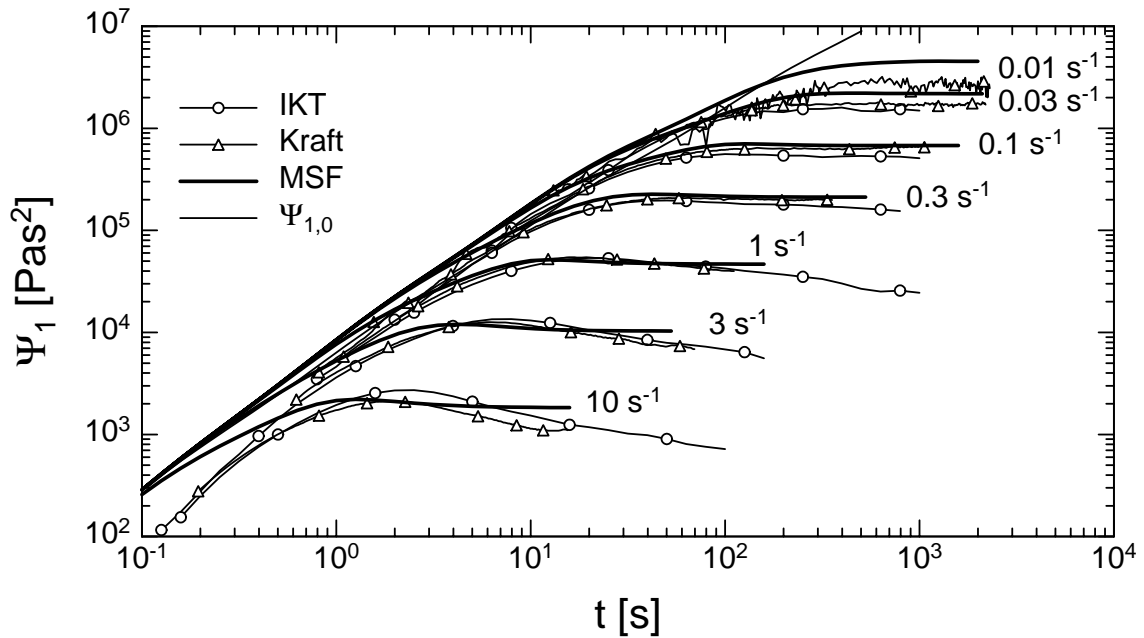


Figure 6.15: First normal stress coefficient Ψ_1 of melt LDPE I at a temperature of $T = 150\text{ }^\circ\text{C}$, with $a_1 = 0.01$ and $a_2 = 0.036$ (Eq. (6.59)).

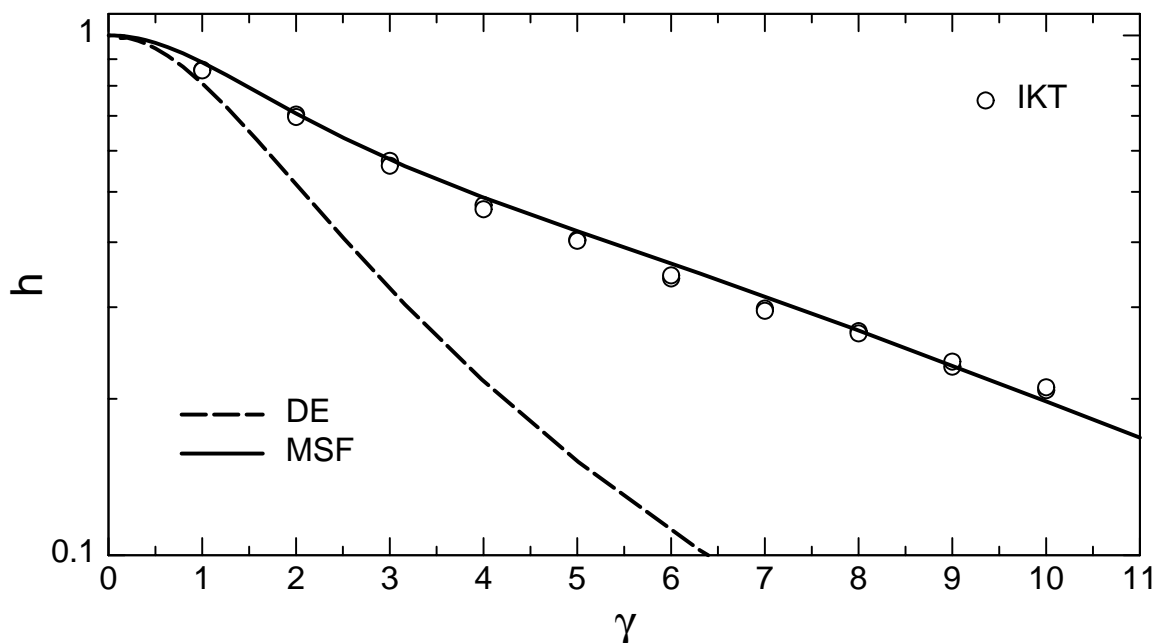


Figure 6.16: Damping function h of melt LDPE I in shear, with $a_1 = 0.01$ and $a_2 = 0.036$ (Eq. (6.57)).

6.5 Comparison of steady-state values in shear and elongational flows with predictions of the extended MSF model

Finally, the steady-state values of shear and elongational flow are examined in more detail for melts HDPE I and LDPE I by comparing them with the steady-state values of the predictions of the extended MSF model (figs. 6.17, 6.18), which were calculated for strain-rates between 10^{-4} and 300 $1/s$, and with the same values of a_1 and a_2 as determined above. As before, the elongational data are rescaled to shear flow. The steady-state values of the elongational data are denoted by the same symbols as used for the uniaxial viscosity in figures 6.3 and 6.10, whereas bold, larger symbols indicate an early rupture due to large stresses which arise at strain-rates $\dot{\epsilon} \geq 0.3$ $1/s$.

For both melts, the predictions of the extended MSF model are in qualitative agreement with experimental data. Deviations at high strain-rates might be due to the early rupture of the polymer melt, and deviations at lower strain-rates due to experimental uncertainties related to small elongational forces. The agreement of the steady-state values of the shear viscosity $\eta(\dot{\gamma}, t)$ between experimental data measured in our laboratory (denoted by IKT), and of the predictions of the extended MSF model is excellent for both melts.

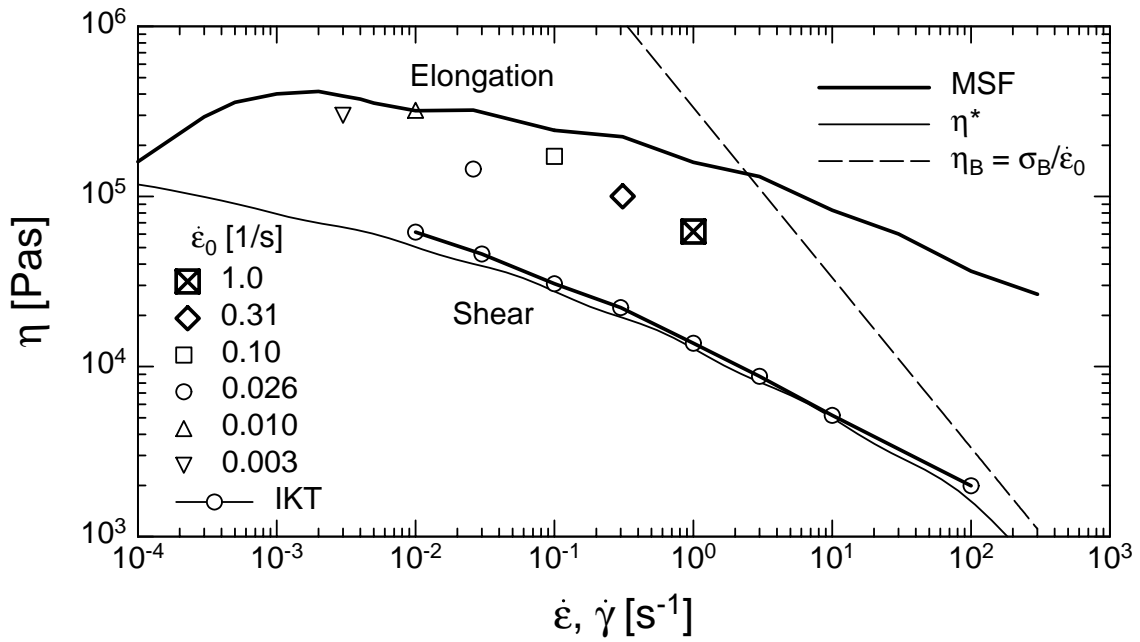


Figure 6.17: Comparison of shear flow and elongational flow with MSF theory for melt HDPE I

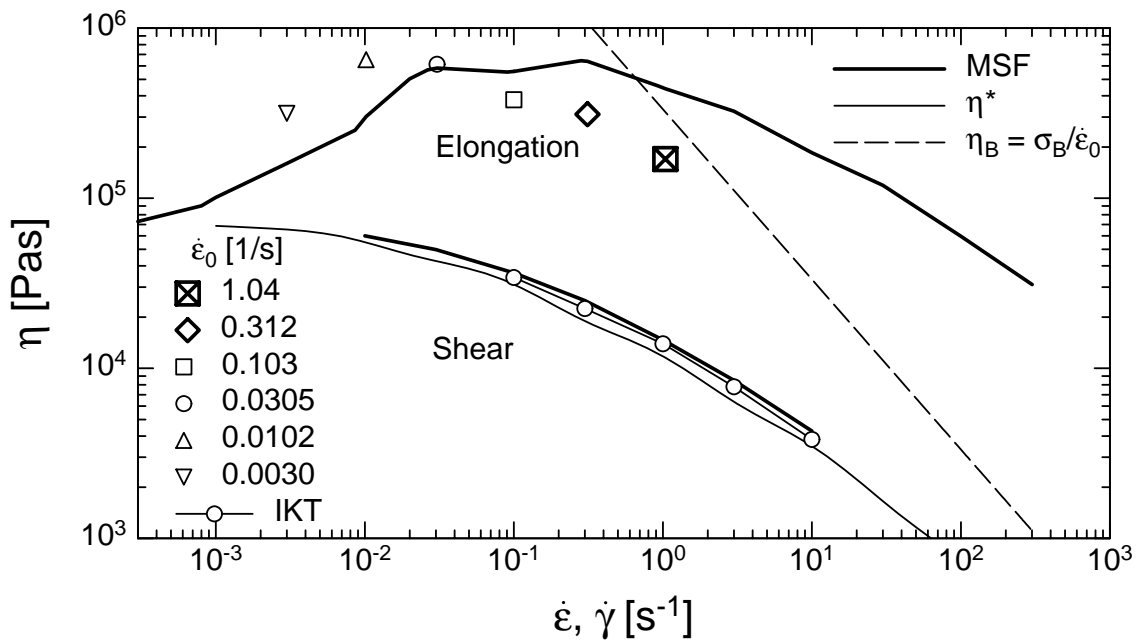


Figure 6.18: Comparison of shear flow and elongational flow with MSF theory for melt LDPE I

The steady-state values of the shear viscosity are also compared to the complex viscosity $\eta^*(\dot{\gamma})$,

$$|\eta^*(\dot{\gamma})| = \frac{\sqrt{G'^2 + G''^2}}{\omega} = \frac{\sqrt{G'^2 + G''^2}}{\dot{\gamma}} \quad (6.60)$$

determined by oscillatory measurements of G' and G'' (chapt. 2.2, chapt. 3.2), and by using the "Cox-Merz rule" with $\omega = \dot{\gamma}$ [12]. The steady-state values of the shear viscosity are very close to the complex viscosity which confirms once more the quality of both the measurements and the predictions. At small rates, the predictions of the steady-state values in shear and elongational flow come together at the zero-shear viscosity η_0 . At high deformation rates, both the experimental data and the predictions in shear and elongational flow show the same slope.

From experiments with the Rheotens, which was developed by Meissner [46] as a prototype flow for isothermal melt spinning, a critical rupture stress σ_B can be determined, at which filament breakage occurs. For polyethylenes a value of approximately $\sigma_B = 1$ MPa is reported [3], [2]. The corresponding "viscosity at break", $\eta_B(t)$, is calculated by dividing $\sigma_B = 1$ MPa by three times the strain rate $\dot{\epsilon}_0$, and is indicated in figures 6.17 and 6.18 by the dashed line. No steady state extension can be realised above this line due to brittle melt rupture.

7 Conclusions

The main purpose of this work was to develop a general rheological constitutive equation for polymer melts which allows consistent description of extensional and shear flows.

After summarising the basics of continuum mechanics of large deformations, and introducing the theory of linear viscoelasticity, non-linear network models were considered, namely the theory of entropy elasticity and the rubber-like liquid theory including the damping function approach. For tube models, non-linear strain measures can be derived from a molecular slip-link model, including the strain measure of the Doi-Edwards (DE) theory. Further developments of the DE theory considering chain stretch processes were discussed, in particular the molecular stress function (MSF) theory.

Experimental data of a linear (HDPE) and a long-chain-branched (LDPE) polyethylene melt measured in shear flow by Kraft (1996) [27], and in uniaxial, equibiaxial, and planar extensional flow by Hachmann (1996) [23] were analysed with the intention to check and improve tube models. Measurements in shear flow with rotational rheometry and in uniaxial elongational flow with a commercial elongational rheometer RME [49] were repeated and were found to be in good agreement with earlier measurements. Additionally, shear relaxation experiments were performed to extend the number of non-linear rheological experiments for the purpose of verification of improved constitutive equations. Further uniaxial elongational tests were done on many linear and long-chain-branched polymer melts. Simultaneously, experimental problems with the commercial elongational rheometer RME were revealed.

Doi and Edwards (1978) [18], [19] introduced the tube model with a universal non-linear strain measure for polymer melts. The basic assumption concerning non-linear viscoelasticity is that the tube diameter remains constant with deformation. Hence, the stress is governed only by orientation of the polymer chains. It was shown that the Doi-Edwards (DE) model predicts the shear-thinning behaviour of polymer melts at least qualitatively, but cannot predict any strain-hardening behaviour in extensional flows [81] neither for linear nor for long-chain-branched polymer melts. The molecular stress function (MSF) theory, developed by Wagner and Schaeffer (1992) [85], [86], takes into account stretch processes of the tube segments by assuming that the tube diameter decreases with increasing deformation. Derived from a strain energy function, the molecular stress function f depends on the average logarithmic stretch $\langle \ln(u') \rangle_0$. For linear melts, a linear dependence of f on $\exp(\langle \ln(u') \rangle_0)$ is found, which is called the linear molecular stress function (LMSF) model. With the LMSF model, the viscosity upturn is consistently described for the HDPE melt considered. However, long-chain-branched melts show a stronger viscosity upturn which has to be taken into account by a quadratic dependence on $\exp(\langle \ln(u') \rangle_0)$, and which is called the quadratic molecular stress function (QMSF) model. Again, the viscosity upturn of the LDPE melt is consistently described by the QMSF model. Viscosities of both linear and long-chain-

branched melts show a saturation effect and approach steady-state values at large deformations. This was modelled by the assumption that the reduction of the tube diameter is limited, i.e. a maximum stretch of the macromolecular chains exists. Therefore, a maximum value of the molecular stress function, f_{max} , was introduced. When f_{max} was fitted to the uniaxial viscosity, a consistent description of all extensional modes was possible. This is not only true for the linear and long-chain-branched melt investigated, but for various other linear, short-chain and long-chain-branched polymer melts investigated by means of the RME. Hence, the non-linear material parameter f_{max} reveals differences in the strain-hardening behaviour. However, with f_{max} fitted to uniaxial data, it was not possible to describe shear flow quantitatively. A smaller value of f_{max} was necessary.

To understand the difference between rotational and irrotational flows, the kinematics of tube deformation was further investigated, and constraint release (CR) as a dissipative process was introduced which led to a strain-dependent evolution equation for the molecular stress function. The new constraint release mechanism is based on the difference between affine convection of unit vectors describing tube segment orientation and tube cross-section orientation. Tube kinematics is fundamentally different for rotational and irrotational flows, and therefore distinguishes explicitly between simple shear and pure shear (planar extension). Thus, limited segmental stretch of macromolecules in shear flow is consistent with strong segmental stretch in planar extension and pronounced strain-hardening behaviour in extensional flows. To take into account these differences, two non-linear parameters a_1 and a_2 are necessary, both of which govern dissipation in simple shear flow, while dissipation in constant strain-rate extensional flows (being irrotational) depends on a_1 only, which is related to the maximum molecular stress f_{max} .

For start-up of simple shear and extensional flows, the predictions of this new simple set of constitutive equations consisting of a single integral equation for the stress tensor and a differential evolution equation for the molecular stress function with only two non-linear material parameters, are in excellent agreement with experimental data of linear and long-chain-branched polymer melts. Also, stress relaxation after a step-shear strain is described, i.e. the model is time/deformation separable.

Hence, a general rheological constitutive relation between stress and deformation history of a polymer melt was developed which allows to describe extensional flows and shear flow consistently with only two non-linear material parameters.

Further investigations will be necessary to prove the validity of this new rheological model in reversing double-step strain experiments which are of relevance in polymer processing. Also of interest are comparisons of predictions and experiments for mixed flows, as in polymer processing often extensional and shear flows are superimposed.

A Comparison of uniaxial viscosity data to the MSF theory

A.1 Linear polymer melts

Polymer Melt	POP		LLDPE	
Product	Affinity PL 1880		Dowlex NG5056E	
Producer	Dow		Dow	
M_W [g/Mol]	116400 [16]		105000	
M_n [g/Mol]	55100 [16]		35000	
M_W/M_n	2.1		3	
T_m [$^{\circ}C$]	102.5		118.7	
T [$^{\circ}C$]	130		130	
ρ_{RT} [g/cm^3]	0.918		0.919	
ρ [g/cm^3]	0.757		0.8	
E_a [kJ/mol]	41.5		31	
Rheometer	RME (IKT)		RME (IKT)	
Figure	A.1		A.2	
Theory with f_{max}^2	Eq. (5.9) 6		Eq. (5.9) 3	
Relaxation spectrum at T	g_i [Pa]	τ_i [s]	g_i [Pa]	τ_i [s]
	4.829E+05	1.000E-03	4.147E+05	2.548E-03
	2.798E+05	7.197E-03	1.842E+05	2.105E-02
	1.269E+05	5.179E-02	6.841E+04	1.271E-01
	2.970E+04	3.728E-01	1.336E+04	7.974E-01
	6.969E+03	2.683E+00	1.332E+03	5.312E+00
	1.792E+03	1.931E+01	8.827E+01	3.295E+01
	1.358E+02	1.389E+02	1.457E+00	1.000E+03

Table A.1: Characterisation of linear polymer melts.

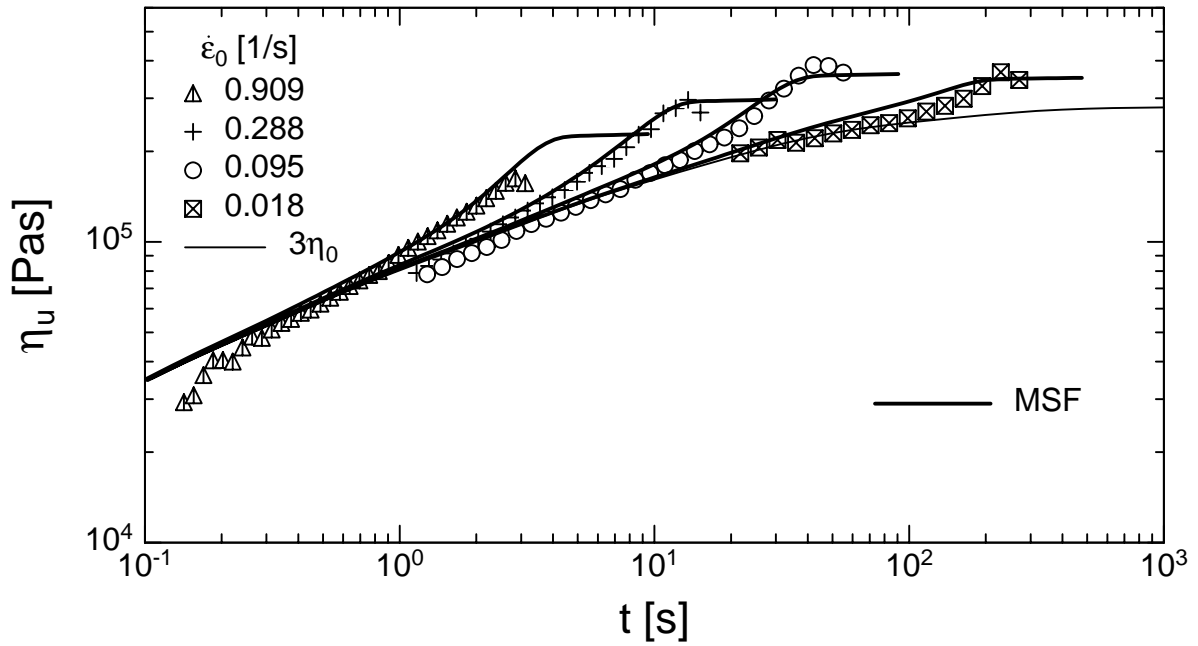


Figure A.1: Elongational viscosity η_u of melt POP at a temperature of $T = 130$ °C.

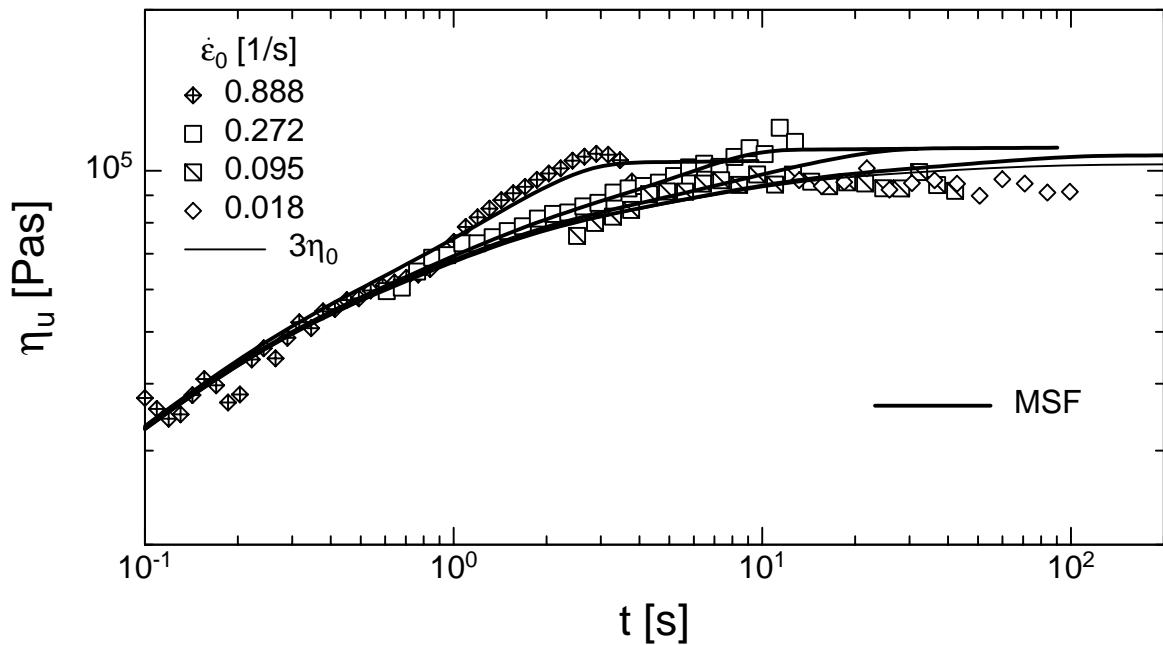


Figure A.2: Elongational viscosity η_u of melt LLDPE at a temperature of $T = 130$ °C.

Polymer Melt	HDPE II		HDPE III	
Product			Stamylan X1010	
Producer	Solvay		DSM	
M_W [g/Mol]	188300		195000	
M_n [g/Mol]	512200		5570	
M_W/M_n	15.5		35	
T_m [$^{\circ}C$]			131	
T [$^{\circ}C$]	190		190	
ρ_{RT} [g/cm^3]			0.957	
ρ [g/cm^3]			0.757	
E_a [kJ/mol]	41.5		27.6	
Rheometer	RME (Solvay) [31]		RME (IKT)	
Figure	A.3		A.4	
Theory	Eq. (5.9)		Eq. (5.9)	
with f_{max}^2	11		5	
Relaxation spectrum at T	g_i [Pa]	τ_i [s]	g_i [Pa]	τ_i [s]
	1.803E+05	4.495E-03	2.471E+05	8.501E-04
	7.561E+04	1.976E-02	1.262E+05	7.545E-03
	3.216E+04	8.684E-02	6.149E+04	5.228E-02
	1.307E+04	3.817E-01	2.329E+04	3.519E-01
	4.876E+03	1.678E+00	5.593E+03	2.416E+00
	1.557E+03	7.375E+00	8.656E+02	1.796E+01
	4.822E+02	3.241E+01	8.418E+01	1.667E+02
	7.868E+01	1.425E+02	9.741E+00	1.647E+03
	3.573E+01	6.262E+02		

Table A.2: Characterisation of linear polymer melts.

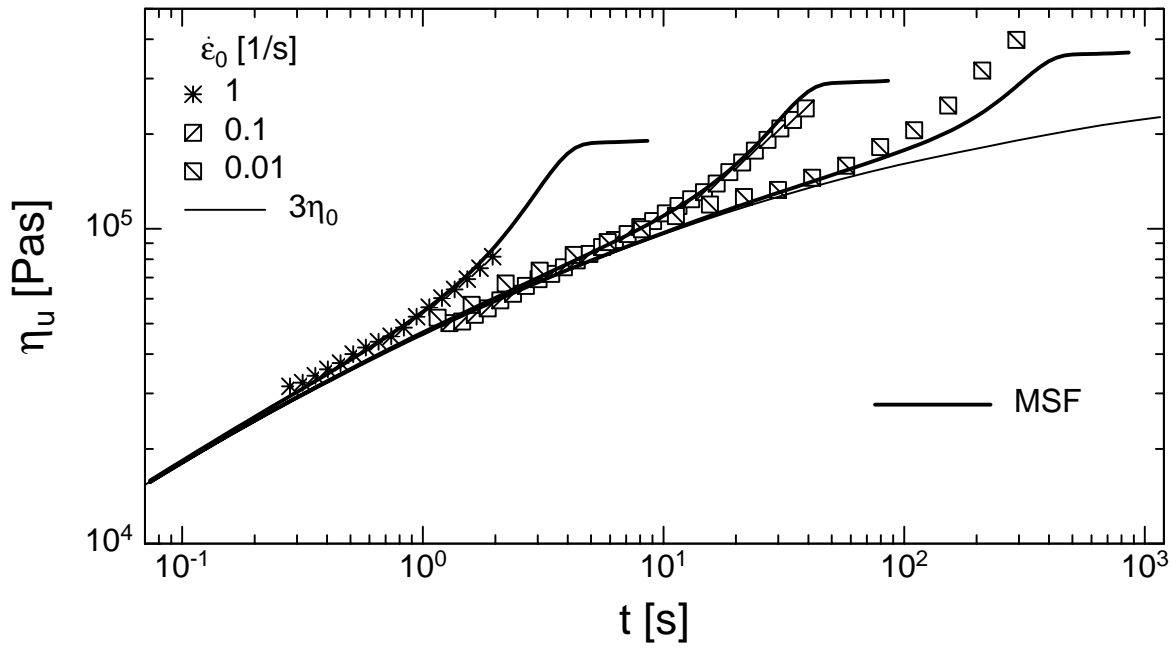


Figure A.3: Elongational viscosity η_u of melt HDPE II at a temperature of $T = 190\text{ }^\circ\text{C}$.

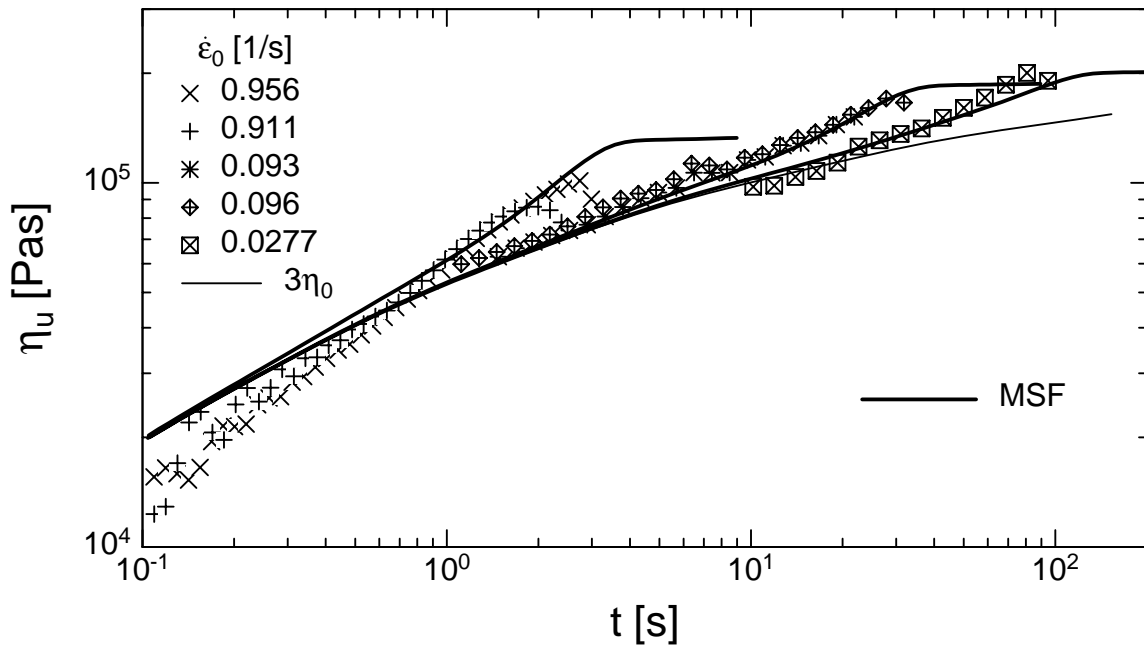


Figure A.4: Elongational viscosity η_u of melt HDPE III at a temperature of $T = 190\text{ }^\circ\text{C}$.

Polymer Melt	PP I		PP III	
Product	Novolen 1100H			
Producer	BASF			
M_W [g/Mol]			245000	
M_n [g/Mol]			52130	
M_W/M_n			4.7	
T_m [$^{\circ}C$]	163		170	
T [$^{\circ}C$]	190		180	
ρ_{RT} [g/cm^3]	0.909		0.908	
ρ [g/cm^3]	0.76			
E_a [kJ/mol]	45 [89]		43.1	
Rheometer	RME (IKT)		MTR (Erlangen) [29]	
Figure	A.5		A.6	
Theory	Eq. (5.9)		Eq. (5.9)	
with f_{max}^2	3		1.6	
Relaxation spectrum at T	g_i [Pa]	τ_i [s]	g_i [Pa]	τ_i [s]
	8.153E+04	8.417E-03	6.240E+04	4.570E-03
	3.252E+04	6.083E-02	2.853E+04	2.990E-02
	1.334E+04	3.502E-01	1.426E+04	1.955E-01
	3.476E+03	2.045E+00	4.284E+03	1.279E+00
	4.930E+02	1.292E+01	7.852E+02	8.361E+00
	4.407E+01	8.642E+01	8.404E+01	5.468E+01

Table A.3: Characterisation of linear polymer melts.

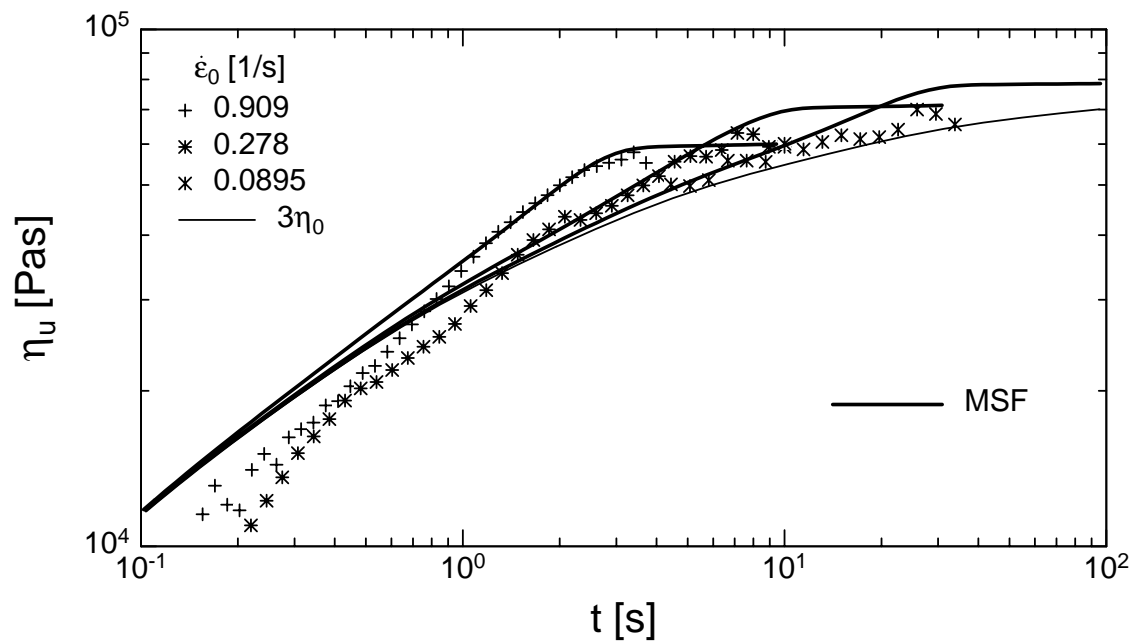


Figure A.5: Elongational viscosity η_u of melt PP I at a temperature of $T = 190 \text{ }^\circ\text{C}$.

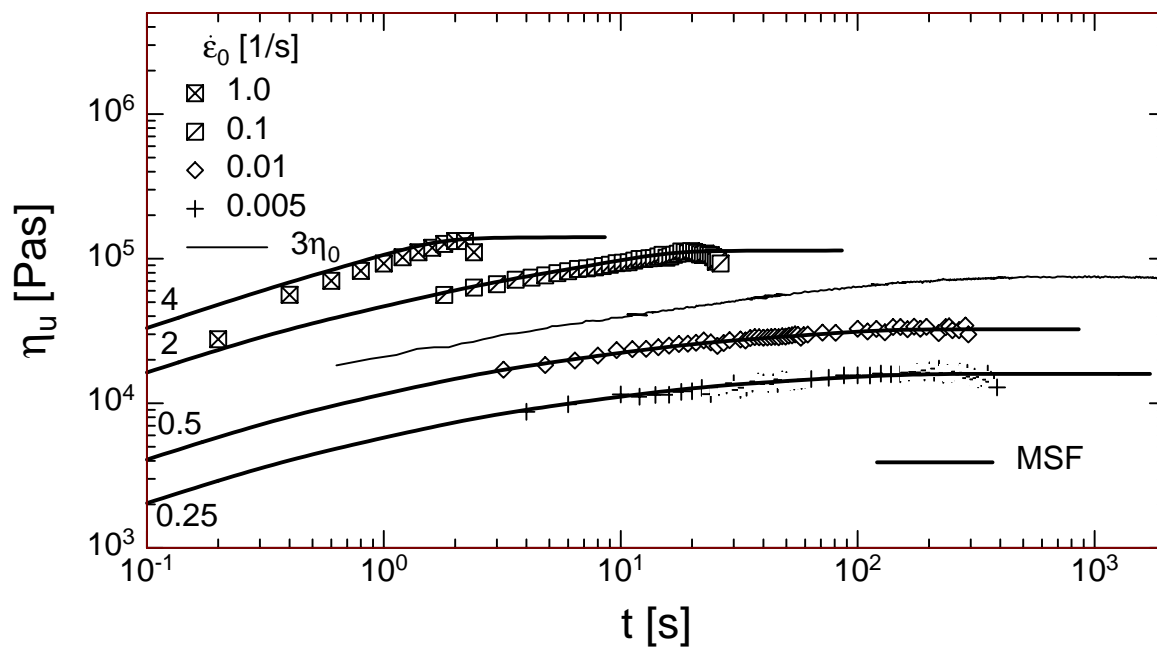


Figure A.6: Elongational viscosity η_u of melt PP III at a temperature of $T = 180 \text{ }^\circ\text{C}$, shifted for clarity by the factors indicated.

A.2 Long-chain-branched polymer melts

Polymer Melt	LDPE I	LDPE II																																		
Product	Lupolen 1810H	Lupolen 3020D																																		
Producer	BASF	BASF																																		
M_W [g/Mol]	188000	300000																																		
M_n [g/Mol]	16600	37500																																		
M_W/M_n	11.3	8																																		
T_m [$^{\circ}C$]	110	114																																		
T [$^{\circ}C$]	150	170																																		
ρ_{RT} [g/cm^3]	0.917	0.94																																		
ρ [g/cm^3]	0.778	0.762																																		
E_a [kJ/mol]	58.6	63.8																																		
Rheometer	RME (IKT)	RME (IKT), MTR (BASF)																																		
Figure	A.7	A.8																																		
Theory with f_{max}^2	Eq. (5.20) 50 (new spectrum)	Eq. (5.20) 40																																		
Relaxation spectrum at T	<table border="0"> <thead> <tr> <th>g_i [Pa]</th> <th>τ_i [s]</th> </tr> </thead> <tbody> <tr> <td>5.664E+01</td> <td>3.310E+02</td> </tr> <tr> <td>6.051E+02</td> <td>5.397E+01</td> </tr> <tr> <td>2.852E+03</td> <td>8.565E+00</td> </tr> <tr> <td>1.081E+04</td> <td>1.056E+00</td> </tr> <tr> <td>2.965E+04</td> <td>1.041E-01</td> </tr> <tr> <td>6.202E+04</td> <td>1.126E-02</td> </tr> <tr> <td>2.000E+05</td> <td>9.224E-04</td> </tr> </tbody> </table>	g_i [Pa]	τ_i [s]	5.664E+01	3.310E+02	6.051E+02	5.397E+01	2.852E+03	8.565E+00	1.081E+04	1.056E+00	2.965E+04	1.041E-01	6.202E+04	1.126E-02	2.000E+05	9.224E-04	<table border="0"> <thead> <tr> <th>g_i [Pa]</th> <th>τ_i [s]</th> </tr> </thead> <tbody> <tr> <td>1.542E+05</td> <td>1.472E-03</td> </tr> <tr> <td>5.886E+04</td> <td>9.580E-03</td> </tr> <tr> <td>3.686E+04</td> <td>4.997E-02</td> </tr> <tr> <td>2.220E+04</td> <td>2.855E-01</td> </tr> <tr> <td>1.008E+04</td> <td>1.626E+00</td> </tr> <tr> <td>3.904E+03</td> <td>9.052E+00</td> </tr> <tr> <td>1.081E+03</td> <td>5.141E+01</td> </tr> <tr> <td>1.117E+02</td> <td>3.278E+02</td> </tr> </tbody> </table>	g_i [Pa]	τ_i [s]	1.542E+05	1.472E-03	5.886E+04	9.580E-03	3.686E+04	4.997E-02	2.220E+04	2.855E-01	1.008E+04	1.626E+00	3.904E+03	9.052E+00	1.081E+03	5.141E+01	1.117E+02	3.278E+02
g_i [Pa]	τ_i [s]																																			
5.664E+01	3.310E+02																																			
6.051E+02	5.397E+01																																			
2.852E+03	8.565E+00																																			
1.081E+04	1.056E+00																																			
2.965E+04	1.041E-01																																			
6.202E+04	1.126E-02																																			
2.000E+05	9.224E-04																																			
g_i [Pa]	τ_i [s]																																			
1.542E+05	1.472E-03																																			
5.886E+04	9.580E-03																																			
3.686E+04	4.997E-02																																			
2.220E+04	2.855E-01																																			
1.008E+04	1.626E+00																																			
3.904E+03	9.052E+00																																			
1.081E+03	5.141E+01																																			
1.117E+02	3.278E+02																																			

Table A.4: Characterisation of long-chain branched polymer melts.

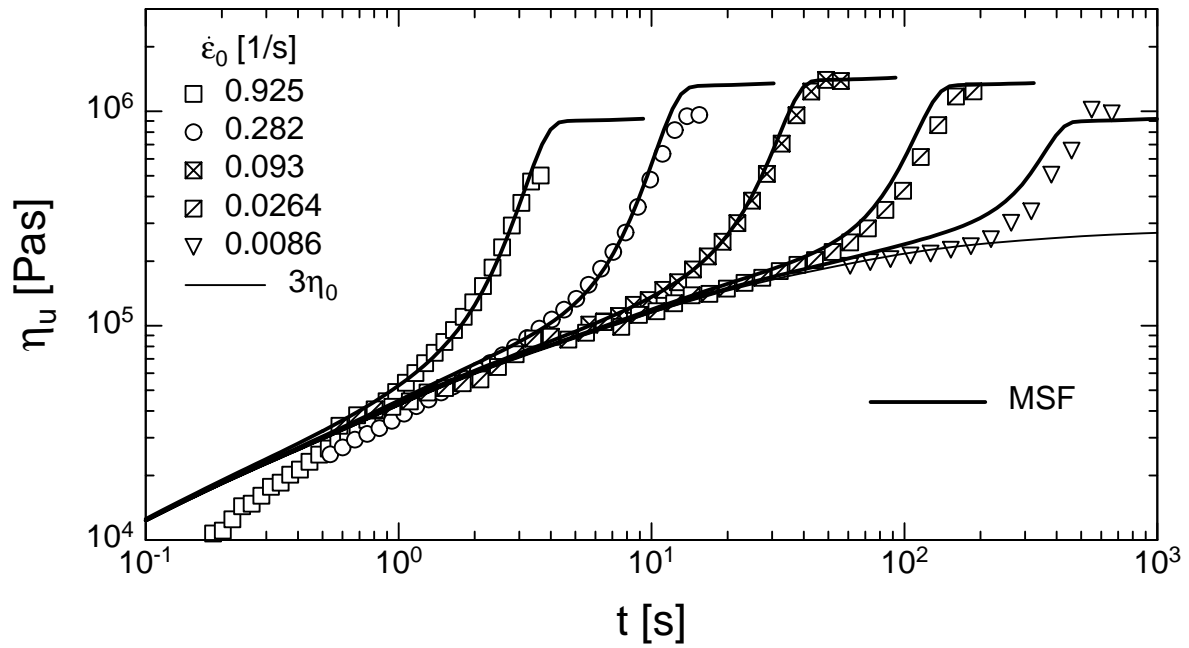


Figure A.7: Elongational viscosity η_u of melt LDPE I at a temperature of $T = 150 \text{ }^\circ\text{C}$ with new relaxation spectrum.

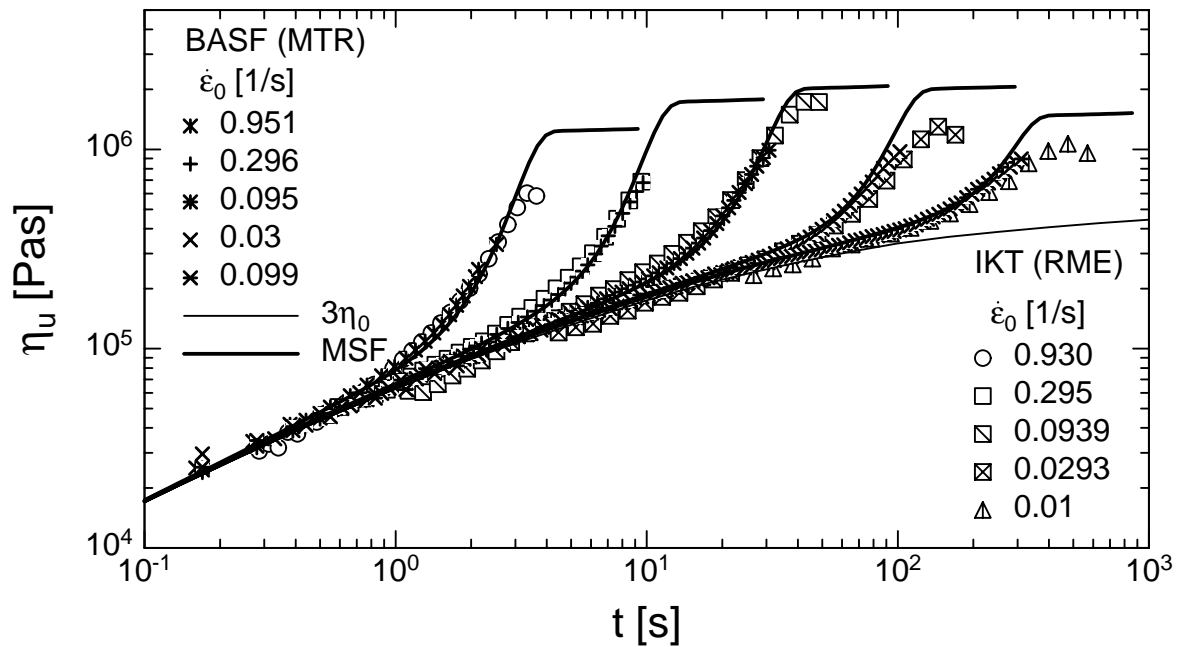


Figure A.8: Elongational viscosity η_u of melt LDPE II at a temperature of $T = 170 \text{ }^\circ\text{C}$.

Polymer Melt	LDPE III		LDPE IV	
Product	(tubular)		(tubular)	
Producer			BASF	
M_W [g/Mol]	119000		144000	
M_n [g/Mol]	24600		21500	
M_W/M_n	4.85		6.7	
T_m [$^{\circ}C$]				
T [$^{\circ}C$]	150		150	
ρ_{RT} [g/cm^3]	0.923		0.924	
ρ [g/cm^3]	0.78		0.78	
E_a [kJ/mol]	62.8		58.5	
Rheometer	RME (IKT)		RME (IKT)	
Figure	A.9		A.10	
Theory	Eq. (5.20)		Eq. (5.20)	
with f_{max}^2	40		60	
	g_i [Pa]	τ_i [s]	g_i [Pa]	τ_i [s]
Relaxation spectrum at T	1.464E+05	2.116E-03	1.303E+05	3.836E-03
	5.262E+04	1.509E-02	4.194E+04	3.495E-02
	2.914E+04	8.403E-02	2.146E+04	1.990E-01
	1.441E+04	4.597E-01	1.024E+04	1.078E+00
	6.004E+03	2.398E+00	4.144E+03	5.679E+00
	1.974E+03	1.200E+01	1.234E+03	2.958E+01
	3.624E+02	6.465E+01	2.035E+02	1.477E+02
	5.166E+00	1.349E+03		

Table A.5: Characterisation of long-chain branched polymer melts.

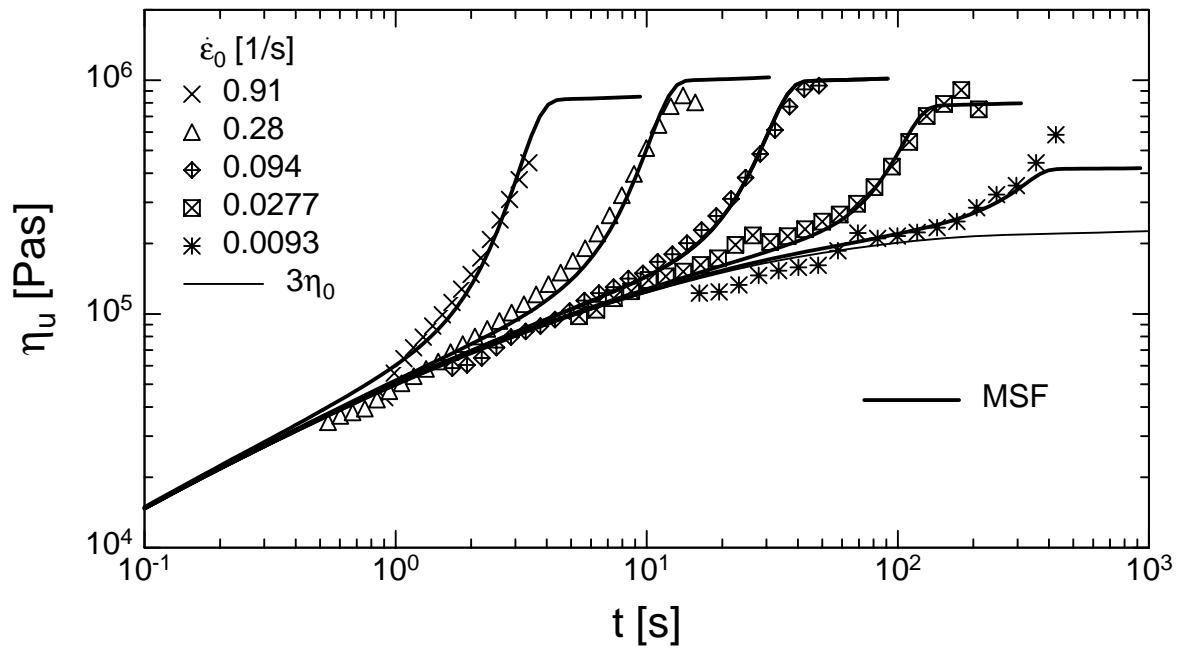


Figure A.9: Elongational viscosity η_u of melt LDPE III at a temperature of $T = 150\text{ }^\circ\text{C}$, shifted for clarity by the factors indicated.

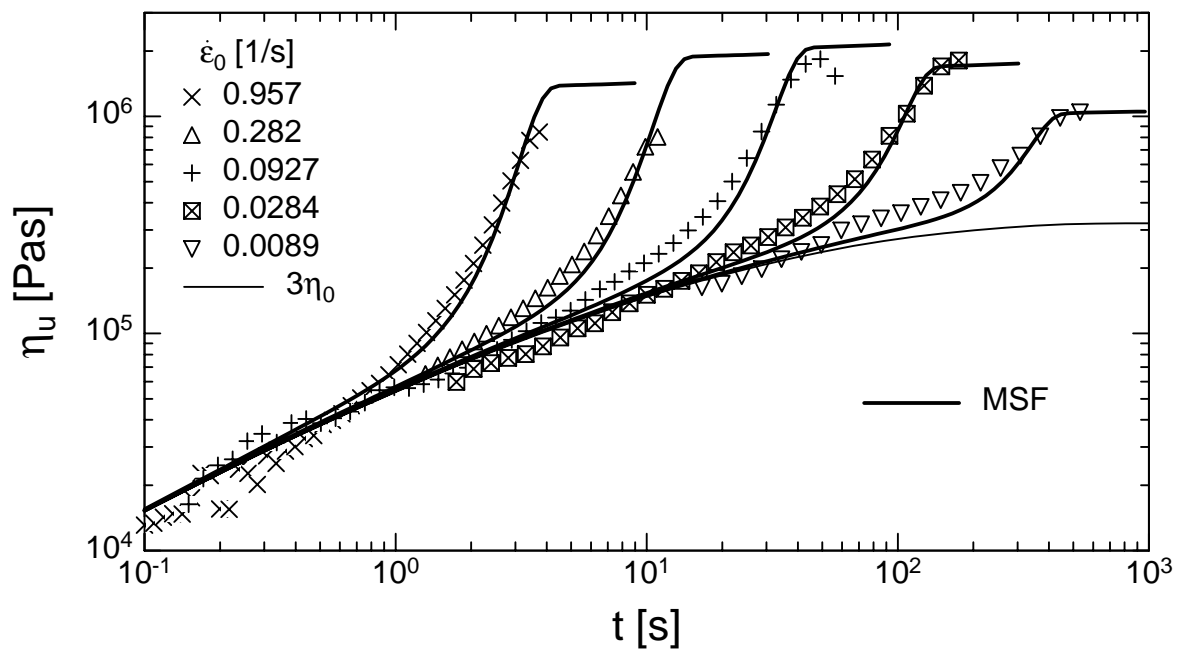


Figure A.10: Elongational viscosity η_u of melt LDPE IV at a temperature of $T = 150\text{ }^\circ\text{C}$.

Polymer Melt	LDPE V	LDPE VI
Product	(autoclave)	(autoclave)
Producer		
M_W [g/Mol]	130000	115000
M_n [g/Mol]	21900	16800
M_W/M_n	5.95	6.8
T_m [$^{\circ}C$]		
T [$^{\circ}C$]	150	150
ρ_{RT} [g/cm^3]	0.921	0.921
ρ [g/cm^3]	0.78	0.78
E_a [kJ/mol]	57.2	55.8
Rheometer	RME (IKT)	RME (IKT)
Figure	A.11	A.12
Theory	Eq. (5.20)	Eq. (5.20)
with f_{max}^2	80	80
Relaxation spectrum at T	g_i [Pa] τ_i [s] 1.525E+05 2.059E-03 5.653E+04 1.730E-02 3.012E+04 1.064E-01 1.371E+04 6.176E-01 4.646E+03 3.439E+00 9.675E+02 1.923E+01 5.848E+01 1.309E+02	g_i [Pa] τ_i [s] 1.226E+05 2.765E-03 4.411E+04 2.700E-02 1.915E+04 1.964E-01 5.655E+03 1.392E+00 8.410E+02 9.245E+00 3.050E+01 5.838E+01

Table A.6: Characterisation of long-chain branched polymer melts.

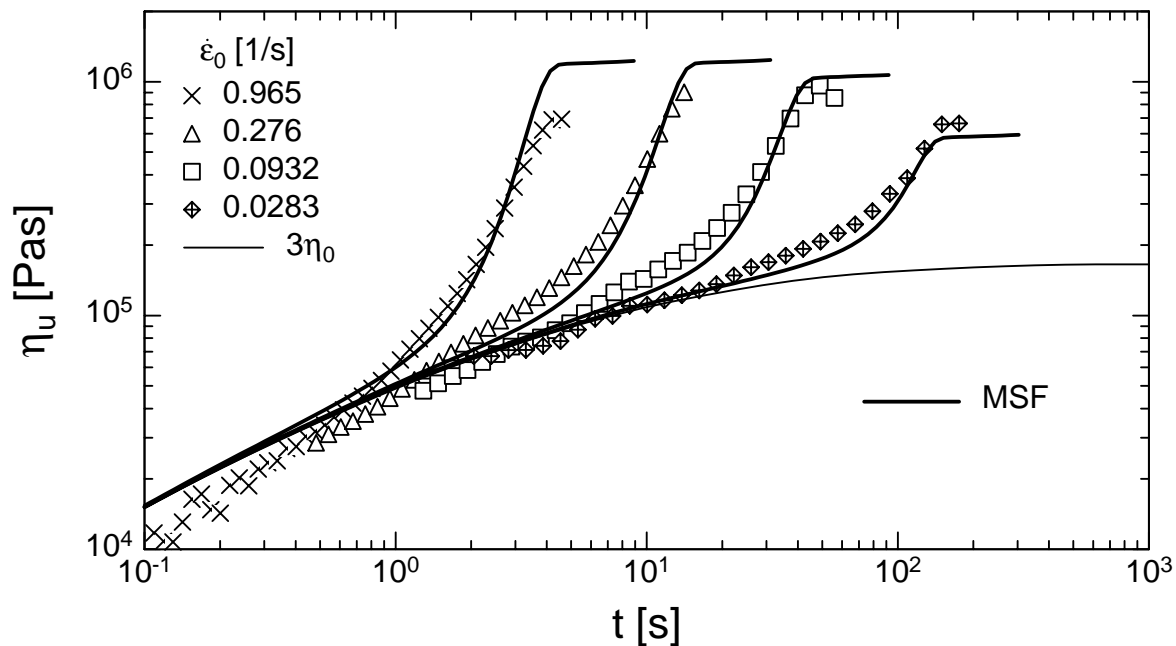


Figure A.11: Elongational viscosity η_u of melt LDPE V at a temperature of $T = 150 \text{ }^\circ\text{C}$.

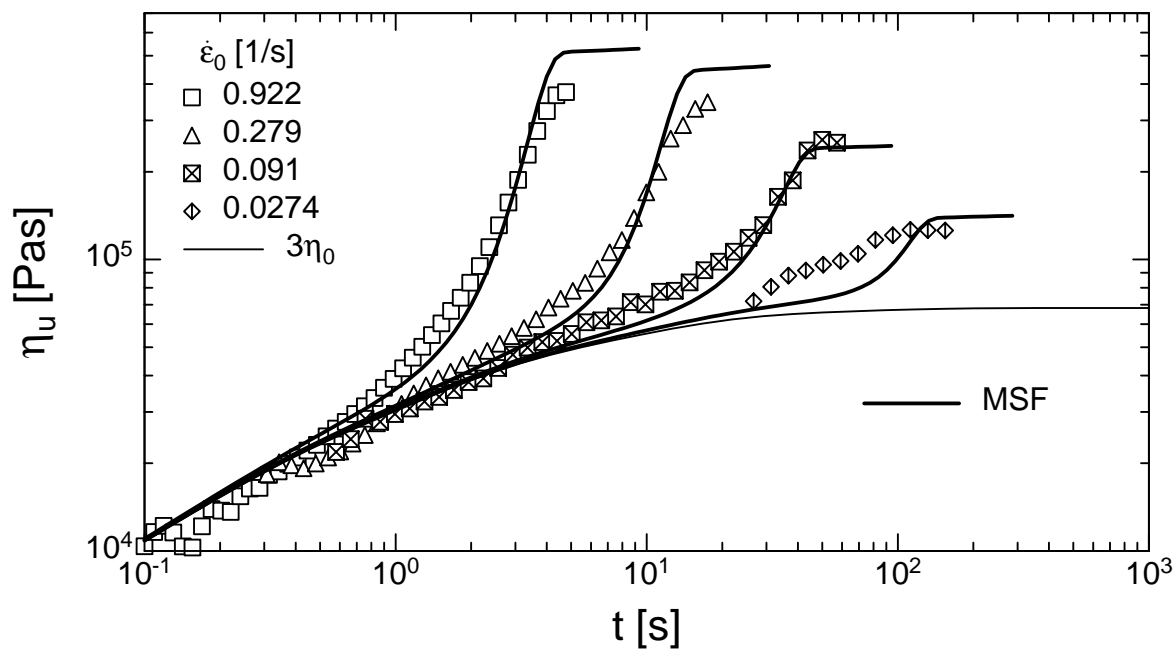


Figure A.12: Elongational viscosity η_u of melt LDPE VI at a temperature of $T = 150 \text{ }^\circ\text{C}$.

B Summary of vector and tensor operations

The result of the dot product of two vectors \underline{u} and \underline{v} is a scalar,

$$\underline{u} \cdot \underline{v} = u_i v_i = u_1 v_1 + u_2 v_2 + \dots + u_n v_n$$

The dyadic product of two vectors \underline{u} and \underline{v} leads to a second-order tensor,

$$\underline{u} \underline{v} = u_i u_j = \begin{pmatrix} u_1 v_1 & u_1 v_2 & \dots & u_1 v_m \\ u_2 v_1 & u_2 v_2 & \dots & u_2 v_m \\ \vdots & \vdots & \vdots & \vdots \\ u_n v_1 & u_n v_2 & \dots & u_n v_m \end{pmatrix}$$

The vector-tensor dot product can be taken in two ways with a vector as result,

$$\underline{\underline{\tau}} \cdot \underline{v} = \tau_{ij} v_j$$

$$\underline{v} \cdot \underline{\underline{\tau}} = v_i \tau_{ij}$$

The single dot product of two tensors $\underline{\underline{\tau}}$ and $\underline{\underline{\sigma}}$ leads to a tensor,

$$\underline{\underline{\tau}} \cdot \underline{\underline{\sigma}} = \tau_{ik} \sigma_{kj}$$

and the double dot product to a scalar

$$\underline{\underline{\tau}} : \underline{\underline{\sigma}} = \tau_{ij} \sigma_{ji} = tr[\underline{\underline{\tau}} \cdot \underline{\underline{\sigma}}]$$

References

- [1] E. Becker and W. Bürger. *Kontinuumsmechanik*. B. G. Teubner Stuttgart, 1975.
- [2] A. Bernnat. Private communication, November 2000.
- [3] A. Bernnat and M. H. Wagner. Rheotens experiments and elongational behaviour of polymer melts. In *Proceedings of the 5th European Rheology Conference*, 1998.
- [4] B. Bernstein, E. A. Kearsley, and L. J. Zapas. A study of stress relaxation with finite stress. *Trans. Soc. Rheol.*, 7:391–410, 1963.
- [5] R. B. Bird, R. C. Armstrong, and O. Hassager. *Dynamics of polymeric liquids, Vol. 2, Kinetic Theory*. John Wiley & Sons, 1977.
- [6] G. Böhme. *Strömungsmechanik nicht-newtonscher Fluide*. B. G. Teubner Stuttgart, 1981.
- [7] K. C. Castleman. *Digital Image Processing*. Prentice Hall, 1996.
- [8] F. N. Cogswell. Tensile deformations in molten polymers. *Rheol. Acta*, 8:187–194, 1969.
- [9] P. G. de Gennes. Reptation of a polymer chain in the presence of fixed obstacles. *J. Chem. Phys.*, 55:572, 1971.
- [10] P. G. de Gennes. Remarks on entanglement and rubber elasticity. *Le Journal de Physique-Lettre*, 35:133–134, 1974.
- [11] J. M. Dealy. *Rheometers for molten plastics*. Van Nostrand Reinhold New York, 1982.
- [12] J. M. Dealy and K. F. Wissbrun. *Melt rheology and its role in plastics processing: Theory and applications*. Van Nostrand Reinhold New York, 1989.
- [13] A. Demarmels and J. Meissner. Multiaxial elongation of polyisobutylene with various and changing strain rate ratios. *Rheol. Acta*, 33:253–259, 1985.
- [14] A. Demarmels and J. Meissner. Multiaxial elongations of polyisobutylene and the predictions of several network theories. *Colloid & Polymer Science*, 264:829–846, 1986.
- [15] S. M. Dinh and R. C. Armstrong. A rheological equation of state for semiconcentrated fiber suspensions. *J. Rheol.*, 28(3):207–227, 1984.
- [16] P. J. Doerpinghaus, S. E. B. Wadud, and D. G. Baird. Flow behaviour of sparsely branched metallocene-catalyzed polyethylenes. In *ANTEC*, 2000.

- [17] M. Doi and S. Edwards. *The theory of polymer dynamics*. Oxford Science publications, 1986.
- [18] M. Doi and S. F. Edwards. Dynamics of concentrated polymer systems. *Faraday Trans.I*, 74:1789–1801, 1978.
- [19] M. Doi and S. F. Edwards. Dynamics of concentrated polymer systems. *Faraday Trans.II*, 74:1802–1817, 1978.
- [20] P. Ehrecke. *Untersuchungen zur Irreversibilität von Netzwerkenschlaufungen beim Fließen von Polymerschmelzen*. PhD thesis, Universität Stuttgart D93, Shaker Verlag Aachen, 1997.
- [21] J. D. Ferry. *Viscoelastic properties of polymers*. John Wiley & Sons, 1961.
- [22] P. J. Flory. Statistical thermodynamics of random networks. *Proc R Soc London A*, 351:351–380, 1976.
- [23] P. Hachmann. *Multiaxiale Dehnung von Polymerschmelzen*. PhD thesis, ETH Zürich Nr. 11890, 1996.
- [24] G. Ianniruberto and G. Marrucci. On compatibility of the Cox-Merz rule with the model of Doi and Edwards. *J. Non-Newtonian Fluid Mech.*, 65:241–246, 1996.
- [25] N. J. Inkson and T. C. B. McLeish. Predicting low density polyethylene melt rheology in elongational and shear flows with "pom-pom" constitutive equations. *J. Rheol.*, 43(4):873–895, 1999.
- [26] S. A. Khan and R. G. Larson. Step planar extension of polymer melts using a lubricated channel. *Rheol. Acta*, 30:1–6, 1998.
- [27] M. Kraft. *Untersuchungen zur scherinduzierten Anisotropie von verschiedenen Polyethylen-Schmelzen*. PhD thesis, ETH Zürich Nr. 11417, 1996.
- [28] M. Kraft, J. Meissner, and J. Kaschta. Linear viscoelastic characterization of polymer melts with long relaxation times. *Macromolecules*, 32:751–757, 1999.
- [29] S. Kurzbeck. *Dehnrheologische Eigenschaften von Polyolefinschmelzen und Korrelationen mit ihrem Verarbeitungsverhalten beim Folienblasen und Thermoformen*. PhD thesis, Universität Erlangen-Nürnberg, 1999.
- [30] S. Kurzbeck, F. Oster, H. Münstedt, T. Q. Nguyen, and R. Gensler. Rheological properties of two polypropylenes with different molecular structure. *J. Rheol.*, 43:359–374, 1999.
- [31] F. Langouche and B. Debbaut. Rheological characterisation of a high-density polyethylene with a multi-mode differential viscoelastic model and numerical simulation of transient elongational recovery experiments. *Rheol. Acta*, 38:48–64, 1999.

- [32] R. G. Larson. *Constitutive equations for polymer melts and solutions*. Butterworths, 1988.
- [33] H. M. Laun. Description of the non-linear shear behaviour of a low density polyethylene melt by means of an experimentally determined strain dependent memory function. *Rheol. Acta*, 17:1–15, 1978.
- [34] H. M. Laun and H. Münstedt. Comparison of the elongational behaviour of a polyethylene melt at constant stress and constant strain rate. *Rheol. Acta*, 15:517–524, 1976.
- [35] J. J. Linster and J. Meissner. Melt elongation and structure of linear polyethylene (HDPE). *Polymer Bulletin*, 16:187–194, 1986.
- [36] A. S. Lodge. Constitutive equations from molecular network theories for polymer solutions. *Rheol. Acta*, 7:379–392, 1968.
- [37] G. Marrucci. Molecular modeling of flows of concentrated polymers. *Transport phenomena in polymeric systems*, pages 1–36, 1989.
- [38] G. Marrucci. Dynamics of entanglements: A nonlinear model consistent with the Cox-Merz rule. *J. Non-Newtonian Fluid Mech.*, 62:279–289, 1996.
- [39] G. Marrucci and B. de Cindio. The stress relaxation of molten PMMA at large deformations and its theoretical interpretation. *Rheol. Acta*, 19:68–75, 1980.
- [40] G. Marrucci and N. Grizzuti. The free energy function of the Doi-Edwards theory: Analysis of the instabilities in stress relaxation. *J. Rheol.*, 27(5):433–450, 1983.
- [41] T. C. B. McLeish and R. G. Larson. Molecular constitutive equations for a class of branched polymers: The pom-pom polymer. *J. Rheol.*, 42(1):81–110, 1998.
- [42] D. W. Mead, R. G. Larson, and M. Doi. A molecular theory for fast flows of entangled polymers. *Macromolecules*, 31:7895–7914, 1998.
- [43] D. W. Mead and L. G. Leal. The reptation model with segmental stretch I. Basic equations and general properties. *Rheol. Acta*, 34:339–359, 1995.
- [44] D. W. Mead, D. Yavich, and L. G. Leal. The reptation model with segmental stretch II. Steady flow properties. *Rheol. Acta*, 34:360–383, 1995.
- [45] J. Meissner. Rheometer zur Untersuchung der deformationsmechanischen Eigenschaften von Kunststoff-Schmelzen unter definierter Zugbeanspruchung. *Rheol. Acta*, 8:78–88, 1969.
- [46] J. Meissner. Dehnungsverhalten von Polyäthylenschmelzen. *Rheol. Acta*, 10:230–242, 1971.

- [47] J. Meissner. Development of a uniaxial extensional rheometer for the uniaxial extension of polymer melts. *Transactions of the society of rheology*, 16:3:405–420, 1972.
- [48] J. Meissner. Modifications of the Weissenberg rheogoniometer for measurement of transient rheological properties of molten polyethylene under shear. Comparison with tensile data. *Journal of Applied Polymer Science*, 16:2877–2899, 1972.
- [49] J. Meissner and J. Hostettler. A new elongational rheometer for polymer melts and other highly viscoelastic liquids. *Rheol. Acta*, 33:1–21, 1994.
- [50] J. Meissner, T. Raible, and S. E. Stephenson. Rotary clamp in uniaxial and biaxial rheometry of polymer melts. *J. Rheol.*, 25:1–25, 1981.
- [51] J. Meissner, S. E. Stephenson, A. Demarmels, and P. Portmann. Multiaxial elongational flows of polymer melts- Classification and experimental realization. *J. Non-Newtonian Fluid Mech.*, 11:221–237, 1982.
- [52] H. Münstedt. Viscoelasticity of polystyrene melts in tensile creep experiments. *Rheol. Acta*, 15:1077–1088, 1975.
- [53] H. Münstedt. New universal extensional rheometer for polymer melts. Measurements on a polystyrene sample. *J. Rheol.*, 23(4):421–436, 1979.
- [54] H. Münstedt, S. Kurzbeck, and L. Egersdörfer. Influence of molecular structure on rheological properties of polyethylenes, Part II. Elongational behavior. *Rheol. Acta*, 37:21–29, 1998.
- [55] H. C. Öttinger. Nonequilibrium thermodynamics- a tool for applied rheologists. *Applied Rheology*, 1:17–26, 1999.
- [56] H. C. Öttinger. Thermodynamically admissible reptation models with anisotropic tube cross sections and convective constraint release. *J. Non-Newtonian Fluid Mech.*, 89:165–185, 2000.
- [57] A. C. Papanastasiou, L. E. Scriven, and C. W. Macosko. An integral constitutive equation for mixed flows: Viscoelastic characterization. *J. Rheol.*, 27(4):387–410, 1983.
- [58] D. S. Pearson, E. Herbolzheimer, N. Grizzuti, and G. Marrucci. Transient behaviour of entangled polymers at high shear rates. *Journal of Polymer Science: Part B: Polymer Physics*, 29:1589–1597, 1991.
- [59] D. S. Pearson and A. D. Kiss. Flow-induced birefringence of concentrated polyisoprene solutions. *J. Rheol.*, 33(3):517–535, 1989.
- [60] C. J. S. Petrie. *Elongational flows*. Pitman, 1979.

- [61] Rheometric Scientific, Inc. *Instrument manual: Polymer melt elongational rheometer RME*, 1995.
- [62] D. Rohr. *Manual for the True Strain Rate Software for the RME*. Swiss Federal Institute of Technology ETH, Zürich, 1996.
- [63] P. Rubio. *Rheologie elongationnelle: Equation constitutive en viscoelasticite non-lineaire*. PhD thesis, Universite de Pau et des Pays de l'Adour, 1999.
- [64] P. Rubio, H. Bastian, and M. H. Wagner. The molecular stress function model for polymer melts with dissipative constraint release. *To appear in J. Rheol.*, 2001.
- [65] P. Rubio and M. H. Wagner. LDPE melt rheology and the pom-pom model. *J. Non-Newtonian Fluid Mech.*, 92:245–259, 2000.
- [66] J. Schaeffer. *Entwicklung einer rheologischen Zustandsgleichung für biaxiale Dehnungen und Scherung von Polymerschmelzen*. PhD thesis, Universität Stuttgart, 1994.
- [67] J. S. Schulze, T. P. Lodge, C. W. Macosko, J. Hepperle, H. Münstedt, T. Virkler, M. Lyon, E. Waßner, H. Bastian, D. J. Groves, D. Ferri, Y. H. Kim, W. Zoetelief, and T. Schweizer. A comparison of extensional viscosity measurements from various RME rheometers. *To appear in Rheol. Acta*, 2001.
- [68] T. Schweizer. Calculation of effective length in the RME, Private communication, April 1999.
- [69] T. Schweizer. Tips for the RME, Private communication, April 1999.
- [70] T. Schweizer. The uniaxial elongational rheometer RME - six years of experience. *Rheol. Acta*, 39:428–443, 2000.
- [71] R. Soskey, P. and H. Winter. Large step shear strain experiments with parallel-disk rotational rheometers. *J. Rheol.*, 28(5):625–645, 1984.
- [72] A. v. Tobolsky and M. Hoffmann. *Mechanische Eigenschaften und Struktur von Polymeren*. Berliner Union Stuttgart, 1967.
- [73] L. R. G. Treloar. *The physics of rubber elasticity*. Clarendon Press Oxford, 1975.
- [74] W. M. H. Verbeeten, G. W. M. Peters, and F. P. T. Baaijens. Differential constitutive equations for polymer melts. In *Proceedings of the XIIIth International Congress on Rheology Cambridge*, 2000.
- [75] G. V. Vinogradov, V. D. Fikhman, and B. V. Radushkevich. Uniaxial extension of polystyrene at true constant stress. *Rheol. Acta*, 11:286–291, 1972.

- [76] M. H. Wagner. Zur Netzwerktheorie von Polymer-Schmelzen. *Rheol. Acta*, 18:33–50, 1979.
- [77] M. H. Wagner. *Vorlesungsskript: Rheologie der Polymerschmelzen*. Universität Erlangen-Nürnberg, Technische Fakultät, Institut für Werkstoffwissenschaften, 1991.
- [78] M. H. Wagner, H. Bastian, P. Ehrecke, P. Hachmann, and J. Meissner. A constitutive analysis of uniaxial, equibiaxial and planar extension of linear and branched polyethylene melts. In *Proceedings of the 5th European Rheology Conference*, 1998.
- [79] M. H. Wagner, H. Bastian, P. Ehrecke, M. Kraft, P. Hachmann, and J. Meissner. Nonlinear viscoelastic characterization of a linear polyethylene (HDPE) melt in rotational and irrotational flows. *J. Non-Newtonian Fluid Mech.*, 79:283–296, 1998.
- [80] M. H. Wagner, H. Bastian, P. Hachmann, J. Meissner, S. Kurzbeck, H. Münstedt, and F. Langouche. The strain-hardening behaviour of linear and longchain-branched polyolefin melts in extensional flows. *Rheol. Acta*, 39:97–109, 2000.
- [81] M. H. Wagner and A. Demarmels. A constitutive analysis of extensional flows of polyisobutylene. *J. Rheol.*, 34:943–958, 1990.
- [82] M. H. Wagner, P. Ehrecke, P. Hachmann, and J. Meissner. A constitutive analysis of uniaxial, equibiaxial and planar extensions of a commercial linear high-density polyethylene melt. *J. Rheol.*, 42(3):621–638, 1998.
- [83] M. H. Wagner and J. Meissner. A useful constitutive analysis of rheological behaviour of polymer melts. *Makromol. Chem.*, 181:1533–1550, 1980.
- [84] M. H. Wagner and J. Schaeffer. Constitutive equations from Gaussian slip-link network theories in polymer melt rheology. *Rheol. Acta*, 31:22–31, 1992.
- [85] M. H. Wagner and J. Schaeffer. Nonlinear strain measures for general biaxial extension of polymer melts. *J. Rheol.*, 36:1–26, 1992.
- [86] M. H. Wagner and J. Schaeffer. Rubbers and polymer melts: Universal aspects of nonlinear stress-strain relations. *J. Rheol.*, 37:643–661, 1993.
- [87] M. H. Wagner and J. Schaeffer. Assessment of nonlinear strain measures for extensional and shearing flows of polymer melts. *Rheol. Acta*, 33:506–516, 1994.
- [88] E. Waßner. Determination of true extensional viscosities with a Meissner-type rheometer. In *Proceedings of PPS15*, 1999.
- [89] E. Waßner. Private communication, November 2000.

Lebenslauf

Heike Bastian

19. Juni 1973	geboren in Calw
1979-1983	Grundschule in Sindelfingen
1983-1992	Gymnasium in den Pfarrwiesen, Sindelfingen Abitur Mai 1992
1992-1997	Studium des Maschinenwesens an der Universität Stuttgart Abschluß als Diplom-Ingenieurin November 1997
1998-2001	Wissenschaftliche Mitarbeiterin am Institut für Kunststofftechnologie der Universität Stuttgart
seit 01.05.2001	Mitarbeiterin der Firma Robert Bosch GmbH, Stuttgart